

Health-conscious fast charging  
of Li-ion batteries via an electro-  
chemical battery aging model.

Hassan Sewailem

Master of Science Thesis



# **Health-conscious fast charging of Li-ion batteries via an electro-chemical battery aging model.**

MASTER OF SCIENCE THESIS

For the degree of Master of Science in Systems and Control at Delft  
University of Technology

Hassan Sewailem

March 20, 2023

Faculty of Mechanical, Maritime and Materials Engineering (3mE) · Delft University of  
Technology

**TNO**

 **TU Delft** Delft  
University of  
Technology

Copyright © Delft Center for Systems and Control (DCSC)  
All rights reserved.

**DCSC**

DELFT UNIVERSITY OF TECHNOLOGY  
DEPARTMENT OF  
DELFT CENTER FOR SYSTEMS AND CONTROL (DCSC)

The undersigned hereby certify that they have read and recommend to the Faculty of  
Mechanical, Maritime and Materials Engineering (3mE) for acceptance a thesis  
entitled

HEALTH-CONSCIOUS FAST CHARGING OF LI-ION BATTERIES VIA AN  
ELECTRO-CHEMICAL BATTERY AGING MODEL.

by

HASSAN SEWAILEM

in partial fulfillment of the requirements for the degree of  
MASTER OF SCIENCE SYSTEMS AND CONTROL

Dated: March 20, 2023

Supervisor(s):

\_\_\_\_\_  
Dr.ir.Ton van den Boom

\_\_\_\_\_  
Dr. Robinson Medina Sanchez

Reader(s):

\_\_\_\_\_



---

# Abstract

The transition towards a more sustainable future has been more prevalent and necessary in recent years due to the increase of greenhouse gas emissions. With the increasing size of modern cities, major concern is risen in the transport sector, becoming one of the main contributors to greenhouse gas emissions. More specifically, road transport is the main contributor within this sector, causing as much as 70 % of the total emissions [3]. As a consequence, the adoption of Electric Vehicles (EVs) has become more prevalent in various countries as a replacement of Internal Combustion Energy Vehicles (ICEVs), being the main cause of pollution within road transport.

On the other hand, EVs are yet to be the perfect replacement due to 2 main bottlenecks, significantly slower charging times compared to refilling Internal Combustion Energy vehicle (ICEV), as well as Li-ion battery lifespan and deterioration over time, which is not an issue in ICEVs, thus a charging profile needs to be determined to mitigate these factors as much as possible. This brings the research proposal "Finding a model-based real-time control charging strategy that mitigates charging times as well as degradation" .

To explore this research topic before developing a model-based control charging strategy, a battery model as well as a degradation model are needed to be implemented, to capture physical states of the battery such as State Of Charge (SOC) and of degradation mechanisms such as Solid Electrolyte Interphase (SEI) and lithium plating. First of all, 3 electro-chemical Li-ion battery dynamical models have been implemented and/or simulated, the Pseudo 2-Dimensional (P2D) model, the Electrolyte Enhanced Single Particle Model (SPMe) and the Extended Single Particle Model (ESPM). The P2D model is considered a full order model, highly accurate for a wide range of charge/discharge currents, which is taken as the base for comparison. The SPMe is a simplified, less accurate model of the P2D, but faster in terms of computational time. Both models are computationally heavy, inapplicable for real time control applications, thus being infeasible for realtime control. The ESPM, a simplification of SPMe, has been developed to tackle the computational time issue, while still maintaining high accuracy performance. The P2D and SPMe are already available and simulation data was obtained using the Python library PyBamm, whereas ESPM was unavailable, thus implemented and simulated on MATLAB. Implementations of comparison between models on MATLAB showed that ESPM can be used for a current range of at least 2C, showing

above 90 % similarity in all model variables compared. In order to include degradation effects in the control strategy, a detailed electro-chemical degradation model, incorporating the 2 main aging effects, SEI growth and lithium plating has been implemented and simulated on MATLAB where degradation parameters were adjusted to fit the capacity fade specifications for the LGM50 battery. Such degradation effects were incorporated such that they could be minimized separately in the charging strategy.

Lastly, based on the models developed, an Nonlinear Model Predictive Control (NMPC) control strategy has been developed with the aim to achieve a tradeoff between charging time, SEI growth and lithium plating as well as change of charge current with time while staying between the feasible model and cell constraints. A Health Conscious Fast charging strategy achieved a charging time of 34 minutes, while having a battery lifespan of approximately 800 charge/discharge cycles. This charging time matches typical DC Fast charging times, while saving approximately 100 cycles from the LGM50 battery lifespan.

---

# Table of Contents

<b>Acknowledgements</b>	<b>xiii</b>
<b>1 Introduction</b>	<b>1</b>
1-1 Background Of Electric Vehicles . . . . .	1
1-2 Advantages and Disadvantages of EVs . . . . .	1
1-3 Batteries used in EVs . . . . .	2
1-4 Li-ion Battery Modelling Methods and Degradation Mechanisms . . . . .	3
1-5 Charging Strategies . . . . .	4
1-6 Thesis Goal and Structure . . . . .	5
<b>2 Literature Review</b>	<b>7</b>
2-1 Li-ion Battery Dynamical Models . . . . .	7
2-1-1 P2D Model [21] . . . . .	8
2-1-2 Electrolyte Enhanced Single Particle Model (SPMe) [28] . . . . .	13
2-1-3 The Extended Single Particle Model (ESPM) . . . . .	19
2-1-4 Conclusion . . . . .	24
2-2 Li-ion Battery Degradation Models . . . . .	24
2-2-1 Description . . . . .	24
2-2-2 Accuracy of degradation model . . . . .	25
2-2-3 Other Methods in Literature . . . . .	27
2-3 Charging Strategies . . . . .	27
2-3-1 Introduction . . . . .	27
2-3-2 Method 1 [44] . . . . .	27
2-3-3 Result of method 1 . . . . .	28
2-3-4 Method 2 [77] . . . . .	31
2-3-5 Results of method 2 . . . . .	32
2-3-6 Other methods in literature . . . . .	33
2-4 Literature Discussion . . . . .	35

<b>3</b>	<b>Mathematical Modelling and Implementation</b>	<b>37</b>
3-1	Introduction . . . . .	37
3-2	Battery Model Dynamics . . . . .	37
3-2-1	ESPM . . . . .	37
3-3	Degradation Model Dynamics . . . . .	40
3-3-1	SEI Growth . . . . .	40
3-3-2	Lithium Plating . . . . .	41
3-3-3	Diffusion Equations . . . . .	41
3-4	Model Implementation and Simulation . . . . .	42
3-4-1	P2D Model and SPMe . . . . .	42
3-4-2	ESPM . . . . .	43
3-4-3	Degradation Model . . . . .	47
3-5	Results . . . . .	50
3-5-1	Performance Indicators . . . . .	50
3-5-2	Battery Diffusion Model . . . . .	50
3-5-3	Degradation Model . . . . .	55
3-6	Discussion . . . . .	58
3-6-1	Battery Diffusion Model . . . . .	58
3-6-2	Degradation Model . . . . .	59
3-7	Conclusion . . . . .	60
<b>4</b>	<b>Charging Strategy Implementation</b>	<b>61</b>
4-1	Introduction . . . . .	61
4-2	Model Formulation . . . . .	61
4-2-1	NMPC Description . . . . .	61
4-2-2	NMPC Charging Strategy Formulation . . . . .	62
4-3	Methodology . . . . .	64
4-3-1	MATLAB Nonlinear Optimizer " <b>fmincon</b> " . . . . .	64
4-3-2	Choosing the weights $Q$ and $R$ . . . . .	66
4-3-3	NMPC Parameters . . . . .	68
4-4	Results . . . . .	68
4-4-1	Constraint Satisfaction . . . . .	69
4-4-2	Charging Speeds . . . . .	69
4-4-3	Degradation Results . . . . .	71
4-4-4	Computational Time . . . . .	75
4-5	Discussion . . . . .	76
4-6	Conclusion . . . . .	77
<b>5</b>	<b>Conclusions and Recommendations</b>	<b>79</b>
5-1	Conclusions . . . . .	79
5-2	Recommendations . . . . .	80

---

<b>A</b>	<b>The Back of the Thesis</b>	<b>83</b>
A-1	Battery and Degradation model (LGM50 5 Ah battery) . . . . .	85
A-1-1	Symbol Definition and Parameter Sets . . . . .	85
<b>B</b>	<b>NMPC</b>	<b>87</b>
B-1	Parameters per Strategy . . . . .	87
B-1-1	State $\mathbf{x}$ and Input $\mathbf{u}$ Bounds . . . . .	87
B-1-2	Weighting Matrices $Q$ and $R$ . . . . .	88
	<b>Glossary</b>	<b>99</b>
	List of Acronyms . . . . .	99
	List of Symbols . . . . .	100
	<b>Index</b>	<b>101</b>



---

# List of Figures

1-1	Strengths and weaknesses of lead-acid, Li-ion, Nickel Metal Hydride (NiMH) and Nickel Cadmium (NiCd) batteries. [84] . . . . .	3
2-1	List of the main Lithium ion battery models found in literature. [34] . . . . .	8
2-2	Pseudo 2-Dimensional model diagram. [35] . . . . .	9
2-3	Comparison between experimental, P2D (Doyle-Fuller Newman (DFN)) and Full Homogenized Macroscale (FHM) for the terminal voltage (V) against time (s) for the different constant charging experiments [8]. . . . .	12
2-4	Schematic of the P2D and Single Particle (SP)/SPMe models of a lithium ion battery. [40] . . . . .	13
2-5	Comparison of the pore wall fluxes at the cc-neg interface and the pos-cc interface simulated by SP, SPM (ESP) and P2D models under 1C ((a) and (b) respectively) 3C ((c) and (d) respectively) / 4C ((e) and (f) respectively) rate discharges. [50].	17
2-6	Plots of the terminal voltage profiles simulated by SP,SPMe (ESP) and P2D models and the corresponding deviations under 1C ((a) and (b) respectively), 3C ((c) and (d) respectively) and 4C ((e) and (f) respectively) rate discharges. [50]. . . . .	18
2-7	The computation times of SP, SPM (ESP) and P2D models. [50]. . . . .	19
2-8	Plot of cell voltage (V) against time (s) and a current profile (C-rate) against time (s) for the ESPM model (blue) as well as experimental data (red). [44] . . . . .	22
2-9	Plot of cell voltage (V) against time (s) and a current profile (C-rate) against time (s) for the ESPM model (blue) as well as experimental data (red) [44] . . . . .	22
2-10	Plot of the terminal voltage (V) against time (s) for charging (left plot) and discharging (right plot) cases for both the ESPM and experimental data at charge/discharge rates ranging from 1C to 6C. All curves overlap. [78] . . . . .	23
2-11	Computational times of a reduced order ESPM model (ROEM) and P2D model under different experiment conditions. [38] . . . . .	24
2-12	A summary of the degradation mechanismss for the Li-ion battery [10] . . . . .	25
2-13	Comparison of model results with experiment data in terms of discharge curves at (a) C/3 (b) 1C (c) 2C and (d) 3C measured in the reference performance tests of the cell after different number of cycles. [76] . . . . .	26

2-14	Experiment results for Constant-Current Constant-Voltage (CCCV) strategy at different charging rates, fast charging strategy and health-conscious fast charging for method 1. [44]	30
2-15	Capacity fade comparison between CCCV at different charge rates, fast charging and health conscious fast charging strategies for method 1. [44]	31
2-16	Simulation and experiment results for fast charging strategy for method 2. [77]	33
3-1	Charging Experiment 1.	42
3-2	Charging experiment 2.	42
3-3	Charging Experiment 3.	43
3-4	Charging Experiment 4.	43
3-5	Cathode and Anode Surface Electrolyte Concentrations $c_{e,surf,+}$ and $c_{e,surf,-}$ under constant charging experiment conditions	44
3-6	Plot of P2D model data of the equilibrium electrolyte concentration per current on the cathode current collector surfaces and its corresponding fitting function	45
3-7	Plot of P2D model data of the equilibrium electrolyte concentration per current on the anode current collector surfaces and its corresponding fitting function.	45
3-8		46
3-9	Cycling Experiment Conditions for LGM50 Battery. Taken from LGM50 Battery Specification Sheet.	49
3-10	Degradation Capacity Fade Criteria for the LGM50 battery. Taken from the LGM50 Battery Specification Sheet	49
3-11	Experiment 1 (Fig.3-1) Results	51
3-12	Experiment 2 (Fig.3-2) Results	52
3-13	Experiment 3 (Fig.3-3) Results	53
3-14	Experiment 4 (Fig.3-4) Results	54
3-15		57
3-16		57
3-17	Plot of capacity fade against number of cycles for the LGM50 battery for 0.33C, 1C and 2C constant charging experiments. Discharging experiment is according to Fig.3-9.	58
4-1	Model Predictive Control (MPC)/NMPC algorithm description [37].	62
4-2	Plot of the $j_{sei}$ against time (min) under a 2C constant charging experiment. The peak $abs(j_{j_{sei,max}}) = 0.00024 \frac{A}{m^2}$ .	67
4-3	Plot of the $j_{sei}$ against time (min) under a 2C constant charging experiment. The peak $abs(j_{j_{ipl,max}}) = 1.09e - 08 \frac{A}{m^2}$ .	67
4-4	Plot of SOC and the corresponding charging profile against time for the various charging strategies.	70
4-5	Plots of Anode and Cathode Electrolyte Concentrations $c_{e,surf,+}$ and $c_{e,surf,-}$ under various charging strategies.	71
4-6	Original and zoomed in plots of SEI molar flux $j_{sei} (\frac{A}{m^2})$ against time (min) for the various NMPC charging strategies.	73

---

4-7	Original and zoomed in plots of Lithium Plating molar flux $j_{\text{pl}}$ ( $\frac{\text{A}}{\text{m}^2\cdot\text{s}}$ ) against time (min) for the various NMPC charging strategies. . . . .	74
4-8	Plot of the capacity (%) against the cycle number for for the various charging strategies. 2 cycles correspond to one charge and one discharge. The method at which this plot is obtained is closely similar to the methodology in Section 3-3-3	75



---

# List of Tables

3-2	Table of Variance Accounted For (VAF) between SPMe and P2D model as well as between ESPM and P2D model for the results in Fig.3-11 to Fig.3-14. The experiment numbers 1 to 4 follow experiments in Fig.3-1 to Fig.3-4 respectively.	55
3-1	Table of Root Mean Square Error (RMSE) between SPMe and P2D model as well as between ESPM and P2D model for the results in Fig.3-11 to Fig.3-14. The experiment numbers 1 to 4 follow experiments in Fig.3-1 to Fig.3-4 respectively.	55
4-1	Table of the maximum possible magnitude and squared magnitude of the 3 variables to be minimized $\bar{c}_s - c_{s,max,-}, j_{sei}, j_{ipl}$ .	68
4-2	Summary of Charging Speed and Degradation Results per Strategy.	75
4-3	Computational time (s) of the different charging strategies.	75
A-1	List of Symbols for the P2D,SPMe, ESPM and the electrochemical degradation Model.	85
A-3	List of whole cell constants LGM50.	86
A-2	List of the LGM50 cell electrode parameters used for the P2D,SPMe,ESPM and the electro-chemical degradation Model. <sup>c</sup> : Calculated, <sup>adj</sup> : Adjusted, N/A : Not available.	86



---

# Acknowledgements

I would like to thank my supervisors Ton van den Boom at TU Delft and Robinson Medina Sanchez at TNO, for their assistance while writing this thesis.

Delft, University of Technology  
March 20, 2023

Hassan Sewailem



---

# Chapter 1

---

## Introduction

### 1-1 Background Of Electric Vehicles

The transition towards a more sustainable future has been more prevalent and necessary in recent years due to the increase of greenhouse gas emissions. The transport sector specifically in modern cities plays a major role in such emissions due to the continuously increasing size of modern cities which then results in pollution and other serious environmental problems [30]. Within this sector, road transport is the main contributor in the greenhouse gas emissions. In fact, road transport represents 70 % of all the greenhouse gas emissions in the transport sector [3], thus the main research and focus is on reduction of greenhouse gas emissions within road transport. As a result, many countries have adopted the use of New Energy Vehicles (NEVs), also known as Electric Vehicles (EVs) as a form of reducing the dependence on fossil fuels used by conventional vehicles. Current EVs comprise mainly of plug-in hybrid EVs, and plug-in fully EVs. The world's largest market, China, committed to the development and use of EVs to reduce the import of oil [70]. As a consequence, global sales of EVs have dramatically increased in recent years having sales of 6750000 units in the year 2021, covering a market share of 8.3 % almost double of the year 2020 [1]. The growth is likely to not stop here, as the plans of Electric Vehicle (EV) companies, led by TESLA, is to increase production volumes as well as sales. An example can be that TESLA intend on selling 20 million EVs annually by 2030 according to their 2021 annual report.

### 1-2 Advantages and Disadvantages of EVs

There are many advantages for the adoption of EVs compared to the conventional vehicles. The first obvious reason of EV is that they produce zero tailpipe emissions, meaning that they do not produce any pollutants being CO<sub>2</sub>, nor nitrogen while driving. On top of that, the battery manufacturing process even though it adversely affects the environment in terms of greenhouse gas emissions, it is still considered more respectful to the environment than conventional vehicles [63]. Moreover, EVs are more simple to make and less noisy as the engine

for EVs requires less parts, and no components are needed for noise/vibration reduction. This also means that the possibility for breakdown of EVs is less than the conventional vehicles, due to fewer components. The EV is also known to be more cost effective as the EV motor being more efficient, with higher power density as well as higher power factor (ratio of power drawn by the charger to the power actually utilized in charging) as opposed to the internal combustion engines [56]. For example, the Well To Wheel (WTW) efficiency calculation in [5] shows that if renewable energy is used to feed EVs, the WTW efficiency would be significantly higher compared to the conventional Internal Combustion Energy vehicle (ICEV) with a range efficiency between 40% to 70% as compared to the highest efficiency ICEV being 25% to 37% for the diesel ICEV.

Despite the many advantages that EVs have over conventional Internal Combustion Energy Vehicles (ICEVs), EVs are still far from a perfect replacement to the ICEV for several reasons. First of all, in the industry, the charging times have still not reached the required standards as they are still considered disturbingly higher than refuelling a tank in a conventional ICEV. Typically, fully charging a battery pack takes from 4-8 hours [63]. Even with recent developments in fast charging, one of the fastest chargers in the industry has a charging speed of 16.3 km/min for the Tesla Model S Long Range Plus [75], which is still unsatisfactory compared to ICEVs. If a fast charging speed exceeds 32 km/min, it is assumed to satisfy over 80 % of trips [14]. One other key disadvantage is battery degradation and capacity fade, which is directly related to the charging strategy used as well as other environmental conditions. Other battery related disadvantages include being costly, large and heavier than carrying gasoline [63], however, they are insignificant to the 2 main disadvantages mentioned being fast degradation and long charging times. As a result, the main focus of the literature review is discussing different types of dynamical models for Li-ion batteries in EVs with the incorporation of degradation mechanisms as well as reviewing different charging strategies that have been seen previously in literature. This is in order to choose the best model for implementation for the thesis. The criteria at which the models will be chosen will be discussed in detail in the literature review.

### 1-3 Batteries used in EVs

In the current market, there are 4 leading battery types. They are the Lead-acid, Li-ion, Nickel Metal Hydride (NiMH) and Nickel Cadmium (NiCd) batteries as they represent the highest market shares [84]. A list of advantages and disadvantages of the 4 main battery types can be found in Fig.1-1 below. The main focus of the literature and the thesis will be on Li-ion batteries due to their outstanding specific energy and power, relatively long calendar and cycle lives, high round trip efficiency and the recent extensive research and development globally on Li-ion batteries as found in Fig.1-1. In order to simulate and monitor the behaviour of Li-ion batteries to implement charging strategies, analytical models of the Li-ion battery are needed. This is done to obtain relations between the different battery variables as well as analytically determining control charging strategies for minimizing charging time as well as degradation.

Battery type	Strengths	Weaknesses
Lead-acid	<ul style="list-style-type: none"> <li>+ Relatively low initial cost</li> <li>+ Mature technology</li> <li>+ Large number of manufacturers worldwide</li> <li>+ Reliance on abundant cheap materials</li> <li>+ Satisfactory round-trip efficiency</li> <li>+ No memory effect</li> <li>+ Low self-discharge rate</li> <li>+ Proven efficiency of recycling schemes</li> </ul>	<ul style="list-style-type: none"> <li>- Modest specific energy and power</li> <li>- Short cycle life</li> <li>- High O&amp;M requirements</li> <li>- Performance sensitive to temperature</li> <li>- Limited reliability</li> <li>- Long charging time</li> <li>- Safety concerns; gas release</li> <li>- Reliance on hazardous lead<sup>3</sup></li> </ul>
Li-ion	<ul style="list-style-type: none"> <li>+ Outstanding specific energy and power</li> <li>+ Long calendar and cycle lives</li> <li>+ High roundtrip efficiency</li> <li>+ Low O&amp;M requirements</li> <li>+ Satisfactory operating temperature ranges</li> <li>+ High reliability</li> <li>+ Technological diversity; several chemistries</li> <li>+ Intensive global R&amp;D efforts</li> <li>+ Chemistries with eco-friendly materials available</li> <li>+ Reasonable self-discharge rate</li> <li>+ Relatively fast recharge</li> </ul>	<ul style="list-style-type: none"> <li>- High initial cost</li> <li>- Advanced BMS required</li> <li>- Safety concerns; thermal runaway incidents</li> <li>- Material bottleneck concerns; lithium and cobalt</li> <li>- Currently weak recovery and recycling schemes</li> </ul>
NiMH	<ul style="list-style-type: none"> <li>+ Moderate initial cost</li> <li>+ Satisfactory specific energy and power</li> <li>+ Satisfactory round-trip efficiency</li> <li>+ Low O&amp;M requirements</li> <li>+ High reliability</li> <li>+ Reliance on eco-friendly materials</li> <li>+ Good safety record</li> <li>+ Satisfactory operating temperature ranges</li> <li>+ Relatively fast recharge</li> </ul>	<ul style="list-style-type: none"> <li>- High self-discharge rate</li> <li>- Slight memory effect</li> <li>- Relatively short cycle life</li> <li>- Currently weak recovery and recycling schemes</li> </ul>
NiCd	<ul style="list-style-type: none"> <li>+ Relatively low initial cost</li> <li>+ Outstanding calendar and cycle lives</li> <li>+ Mature technology</li> <li>+ High reliability</li> <li>+ Low O&amp;M requirements</li> <li>+ Reasonable self-discharge rate</li> <li>+ Good safety record</li> <li>+ Extensive operating temperature ranges</li> <li>+ Relatively fast recharge</li> </ul>	<ul style="list-style-type: none"> <li>- Modest specific energy and power</li> <li>- Memory effect</li> <li>- Relatively low round-trip efficiency</li> <li>- Reliance on hazardous cadmium<sup>3</sup></li> </ul>

Figure 1-1: Strengths and weaknesses of lead-acid, Li-ion, NiMH and NiCd batteries. [84]

## 1-4 Li-ion Battery Modelling Methods and Degradation Mechanisms

The purpose of Li-ion battery modelling is simulation of the battery dynamics to resemble real Li-ion battery behaviour, obtain relations between the different internal physical states of the battery and finally determining a charging control strategy with a specific objective. For example, a common relation that is obtained for analysis is the Open Circuit Voltage (OCV) against State Of Charge (SOC) for a certain charge current profile.

As a physical description of the Li-ion battery, the components of it include the anode, cathode, the separator, the electrolyte and the 2 current collectors. While the battery is discharging, the lithium ions are flowed in the electrolyte from the anode to the cathode, passing through the semi-permeable separator and creating a flow of electrons [2]. The exact opposite occurs when charging, meaning the lithium ions move from the cathode to the anode. To obtain an accurate model of the battery, one can incorporate degradation mechanisms within the battery model. There are 2 main causes of capacity fade which are Solid Electrolyte Interphase (SEI) growth and lithium plating or deposition.

An SEI layer, which is a passivation layer [72] forms on the anode [75] in the first few cycles of charging, causing irreversible capacity loss [75]. This layer formed protects from any side reactions occurring with the electrolyte [19]. High temperatures are thought to be a possible reason of formation of the SEI layer [79] [59], however, it is still uncertain what causes degradation at high temperatures in conventional charging and discharging techniques [75].

The other degradation mechanism is lithium deposition, which is also known as lithium plating [44]. This is caused when the lithium ions are flowed at a higher rate than the battery can intercalate [44], thus at high charge currents this occurs. Consequently, the lithium ions are transformed into metallic lithium causing capacity fade as well as hindering battery performance [23]. This shows the complexity of modelling li-ion batteries and degradation mechanisms.

In literature, 3 main methods are used to model Li-ion battery dynamics as well as degradation. They are characteristic maps, equivalent circuit models and physics based electro-chemical models.

Starting with characteristic maps, they are models that use real life charge/discharge experiments or Full Order Models (FOMs) to obtain input-output relations between variables. One example of a Full Order Model (FOM) being used by Lin and colleagues [44], a static map has been obtained from a previously implemented FOM [45] which shows the SEI thickness growth rate as well as lithium plating at different charge rates and different States Of Charge (SOCs). Moreover, a first order transfer function to model Li-ion concentration at a given charge rate with the support of the Extended Single Particle Model (ESPM) to simulate the Li-ion battery diffusion dynamics was obtained [44]. As for testing, it can be on either customized cells (eg. 3 electrode test cells) or special experimental setups such as dilation analysis [75]. For example, lithium plating can be tracked and measured using dilation analysis [11]. This method was implemented which was later used to obtain characteristic maps for health conscious fast charging [67]. Moreover, in a case study by Waldmann and colleagues [74], a customized 3-electrode cell was used to model the battery dynamics and apply optimized charging algorithms by measuring anode voltages at different charge rates. Secondly, equivalent circuit battery modelling mainly uses Resistor-Capacitor (RC) circuits to model battery behaviour. In a recent study by Li and colleagues [42], a physics-based low order RC electrical model was used, along with a thermal network model to model the dynamics along with battery aging, then a Multistage Constant Current Constant Voltage (MCCCV) charging strategy was applied. In addition, in another study by Zou and colleagues [82], a second order RC model coupled with thermal model was used, then an optimization charging strategy with the objective to minimize charging time as well as regulating battery temperature was implemented.

Lastly, physics based electro-chemical models are most commonly researched and used in literature due to their wide flexibility and simplicity in incorporating lithium deposition as well as SEI growth. They include partial differential equations of the diffusion dynamics of the lithium ions in each electrode. The main models used in literature are the FOM, also known as the Pseudo 2-Dimensional (P2D) model [45], simplified P2D [34], Electrolyte Enhanced Single Particle Model (SPMe) [39] and ESPM [51].

The focus of the thesis will be only on electro-chemical models, as they are the most widely used in literature due to their high accuracy and flexibility to manipulate internal battery states.

## 1-5 Charging Strategies

The main purpose of this study is to find a new charging strategy or improve on previous charging strategies that minimize charging time as well aging of the battery. Conventional charging strategies include Constant-Current Constant-Voltage (CCCV) charging [80], pulse

current charging and pulse voltage charging [64] [31]. Although being efficient charging methods for lithium ion batteries, these traditional methods are not performing at a sufficient level in today's market in terms of charging speed and battery lifespan [44]. With recent efforts in this field, more advanced charging strategies have been developed. Examples can be optimization based techniques such as Adaptive Multistage CCCV (AMCCCV) [42], Nonlinear Model Predictive Control (NMPC) [37] etc. Optimization based charging strategies are the most common in the industry at the moment. There are other methods using neural networks [22], fuzzy logic [32] and the traditional MCCCVC [33] [6].

The focus of the literature review and as a result the thesis will be on optimization based charging strategies as they support the electro-chemical models for the battery, leading to the most accurate results. Also, parameters and constraints can be easily modified to reach the global/local optimum desired.

## 1-6 Thesis Goal and Structure

Based on previous studies, an electro-chemical battery dynamic model coupled with a degradation model will be chosen for implementation on MATLAB throughout the thesis. After simulation and validation of the model, a charging strategy is then determined tackling the research proposal "Finding a model-based real-time control charging strategy that mitigates charging times as well as degradation". The thesis report will be structured as follows: the first chapter, **Introduction**, explains the need for the transition to EVs, the current limitations that incorporating EVs impose, with the main ones being battery degradation and charging times. Moreover, the introduction discusses how to approach the research question being "How to minimize battery degradation and charging times using a model-based charging control strategy?". Research subquestions include, "Which electro-chemical battery dynamical model should be used?", "Which degradation model should be used?" and "What type of control strategy to be used?".

The answers to the research questions and subquestions can be found in the second chapter, **Literature Review**, discussing the previous research already done in tackling the same topic, where the first section, "Li-ion Battery Models", highlights the main electro-chemical battery models available in literature, with a performance analysis and discussion in terms of range of charge/discharge currents the model is accurate and computational complexity. The second section in this chapter, "Degradation Models", explains one of the main electro-chemical degradation models currently used in research, with a performance analysis with respect to experimental results. The third section, "Charging Strategies", discusses the main charging strategies available in literature, with a comparison of results in terms of charging time and battery degradation. The last section "Thesis Proposal", concludes the literature review with explaining the reasoning behind the choices made in terms of what would be implemented moving forward with the thesis, as well as the target to be achieved from this implementation.

The third chapter, **Model Implementation**, describes the battery model and degradation model dynamics that are chosen for implementation shown in sections "Battery Model Dynamics" and "Degradation Model Dynamics" respectively. The section "Methodology" describes the details of practical implementation of the battery and degradation models, "Results" presenting the models results for verification of the models chosen, showing accuracy and computational complexity, and finally a "Discussion" section discussing the results obtained.

The next chapter is **Charging Strategy Implementation**, having the same structure as the previous chapter, with the sections "Model Formulation", "Methodology", "Results" and "Discussion".

The final chapter is **Conclusions and Recommendations** which gives a summary of the work done in the Thesis and compares it with what is state of the art in section "Conclusions", then explaining what further extensions could be made on this work in the section "Recommendations".

---

## Chapter 2

---

# Literature Review

### 2-1 Li-ion Battery Dynamical Models

In literature, extensive research is being done on finding an accurate model for the Li-ion battery that does not fail in severe charge/discharge current cases, while also not being computationally expensive. A list of the different types of models found in literature can be seen in Fig.2-1. In this section, some of the main electro-chemical models in literature will be explained, as well as a performance analysis will be performed in terms of computational burden, and accuracy compared to the real Li-ion battery. The goal from such analysis is finding a model to be used that is accurate enough for a wide range of charging currents, while having low enough computational complexity to be applicable for real time control applications. For all models, the symbol definitions and parameter values can be found in Tables A-1, A-2 and A-3 in Appendix A-1.

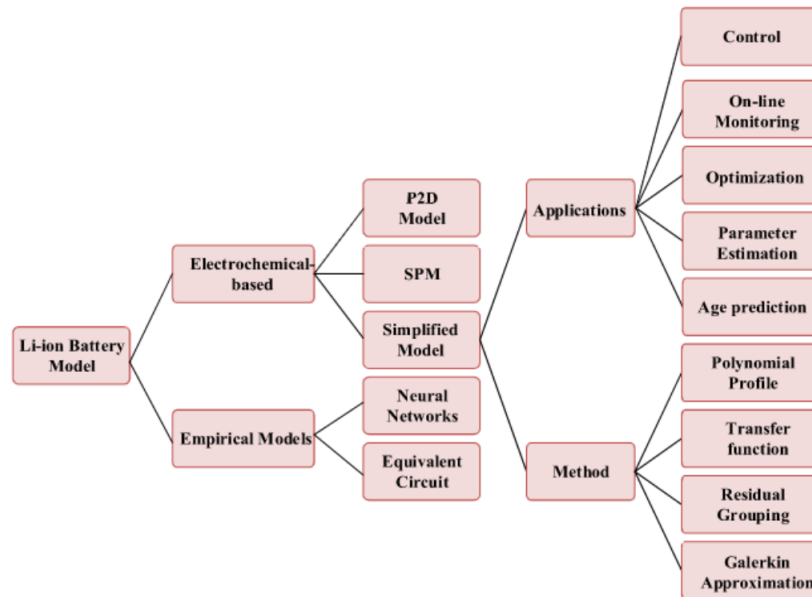


**Figure 2-1:** List of the main Lithium ion battery models found in literature. [34]

### 2-1-1 Pseudo 2-Dimensional (P2D) Model [21]

The P2D is one of the most popular models used in literature for its high accuracy and detail [35]. It has been widely reviewed in literature and validated for a variety of lithium based cells and a wide range of charge current densities [73]. It is a galvano-static, iso-thermal electro-chemical model, meaning that the dynamical equations do not change with changing currents and temperature is assumed to be constant throughout charging/discharging [73]. The conductivity of the current collectors is large enough to assume that there are no significant changes at the current collector in the  $y$  and  $z$  spaces, thus the P2D model assumes the electro-chemical dynamics to be one dimensional [35], specifically the  $x$  direction. In order to take into account the movement of lithium both in the solid and liquid (electrolyte) phases over 1 dimension, small spherical solid particles are fused with the electrolyte. The changes in concentration of lithium within these particles are computed over the radial domain, where  $r$  is the radial position within one of the particles. As a result, in the model dynamics, 2 dimensions are considered, being the  $x$  direction and the pseudo  $r$  direction, which gives it the name pseudo 2-dimensional model. The P2D model can be shown in Fig.2-2.

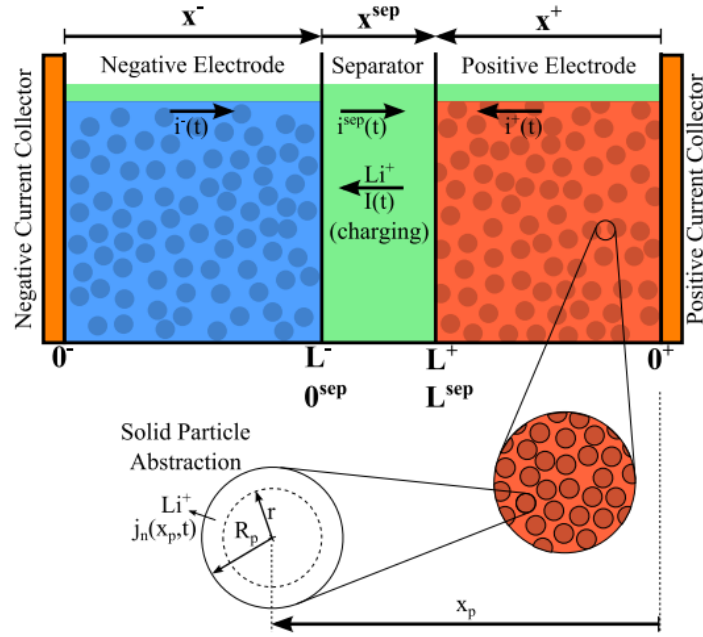


Figure 2-2: Pseudo 2-Dimensional model diagram. [35]

### Solid Phase Diffusion Dynamics

The diffusion dynamics in the solid matrix phase are governed by the local rate of insertion and Fick's second law [54],

$$\frac{\partial c_{s,j}}{\partial t} = D_{s,j} \left( \frac{\partial^2 c_{s,j}}{\partial r^2} + \frac{2}{r} \frac{\partial c_{s,j}}{\partial r} \right). \quad (2-1)$$

As a physical description of the equation above, the evolution of the solid phase concentration  $c_{s,j}$  in electrode  $j = +/-$  (positive/negative) with time  $t$  has both a first and second order dependency with respect to the radial position inside the solid particle  $r$ . The rate at which  $c_{s,j}$  changes with time depends mainly on the solid phase diffusivity constant  $D_{s,j}$ . The boundary conditions are as follows,

$$\begin{aligned} j_j &= -D_{s,j} \frac{\partial c_{s,j}}{\partial r} \text{ at } r = R_p, \\ \frac{\partial c_{s,j}}{\partial r} &= 0 \text{ at } r = 0, \\ \text{and } c_{s,j}(t = 0, r) &= c_{s,0}. \end{aligned} \quad (2-2)$$

The molar flux per electrode  $j_j$  is considered the input to the P2D model and  $R_p$  is the particle radius.

### Electrolyte Phase Diffusion Dynamics

The rate of change in concentration with respect to time in the electrolyte follow the dynamics below,

$$\varepsilon \frac{\partial c_{e,j}}{\partial t} = \frac{\partial}{\partial x} \left( D_{e,j}^{\text{eff}} \frac{\partial c_{e,j}}{\partial x} \right) + a_j (1 - t_+^0). \quad (2-3)$$

where  $\varepsilon = 1$  and  $j_j = 0$  in the separator phase ( $0^{\text{sep}} < x^{\text{sep}} < L^{\text{sep}}$ ) [21] according to Fig.2-2. It can also be seen that there is a second order dependency with respect to the horizontal spacial position  $x$  for the evolution of  $c_{e,j}$  with time and the direct dependency on the input  $j_j$ . The solid and liquid phases are coupled with the input  $j_j$  using the Butler-Volmer kinetics below [20],

$$j_j = \frac{i_{0,j}}{F} \left( \exp \left( \frac{\alpha_{\text{int}} F}{RT} (\eta_{\text{int},j}) \right) - \exp \left( -\frac{\alpha_{\text{int}} F}{RT} (\eta_{\text{int},j}) \right) \right), \quad (2-4)$$

where  $\eta_j = \Phi_{s,j} - \Phi_{e,j} - U_{\text{int},j}$  and  $U_{\text{int},j} = U(c_{s,\text{surf},j})$  which varies per cell electrode chemistry.  $i_{0,j}$  is the Li-ion exchange current density, defined by the following equation [29],

$$i_{0,j} = F k_j (c_{s,\text{max},j} - c_{s,\text{surf},j})^{0.5} (c_{s,\text{surf},j})^{0.5} \left( \frac{c_{e,j}}{c_{e,0,j}} \right)^{0.5} \quad (2-5)$$

where  $k_j$  is the temperature dependent reaction rate constant at electrode  $j$  and  $c_{s,\text{surf},j}$  is the solid phase concentration on the surface of electrode. At the positive current collector, the boundary conditions are as follows,

$$\frac{\partial c_{e,j}}{\partial x}(x = L) = 0 \quad (2-6)$$

At the internal boundary, the flux and concentration are assumed to be continuing and follow the same solid and liquid phase dynamics. At the negative current collector,  $\Phi_{e,-}(x = 0)$  is set to 0, and the Butler-Volmer kinetic expression is used,

$$\frac{\partial c_{e,-}}{\partial x}(x = 0) = -\frac{I(1 - t_+^0)}{F D_{e,j}^{\text{eff}}}. \quad (2-7)$$

Finally, the initial condition for the electrolyte concentration in electrode  $j$  given by,

$$c_{e,j}(t = 0, x) = c_{e,0,j}. \quad (2-8)$$

The state of charge, which is referred to as *SOC* is derived from the solid phase concentration evolution for all electro-chemical models, where it is given as [37],

$$SOC = \frac{\bar{c}_{s,-}}{c_{s,\text{max},-}} \quad (2-9)$$

where  $\bar{c}_{s,-}$  is the volume averaged solid phase concentration at the negative electrode (anode) and  $c_{s,\text{max},-}$  is given as the maximum solid phase concentration in the anode.

## Voltages and Potentials

The cell voltage is given as

$$V_{\text{cell}} = \phi_{s,+}(x = L) - \phi_{s,-}(x = 0) - R_{\text{cell}} \cdot I, \quad (2-10)$$

where  $\Phi_{s,j}$  is the solid phase potential in electrode  $j$  and  $R_{\text{cell}}$  is the internal cell resistance, which was taken to be zero. The rate of change in  $\Phi_{s,j}$  [21],

$$I - i_{s,j} = -\sigma \frac{\partial \Phi_{s,j}}{\partial x}. \quad (2-11)$$

The change in the electrolyte current density is given by,

$$aFj_j = \frac{\partial i_{e,j}}{\partial x}, \quad (2-12)$$

The evolution of the potential in the liquid phase with respect to  $x$  is as follows,

$$\frac{\partial \Phi_{e,j}}{\partial x} = -\frac{I}{\kappa_{\text{eff}}} + \frac{RT}{F} (1 - t_+^0) \left( 1 + \frac{\partial \ln f_A}{\partial \ln c_{e,j}} \right) \frac{\partial \ln c_{e,j}}{\partial x}, \quad (2-13)$$

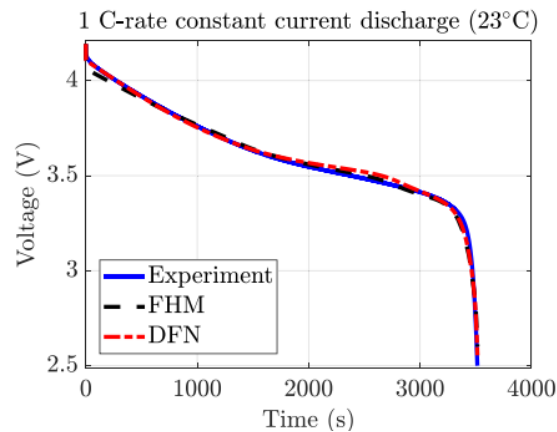
Thus, in the electrodes, there are six equations and six unknowns ( $c_{e,j}$ ,  $\Phi_{e,j}$ ,  $c_{s,j}$ ,  $i_{e,j}$ ,  $j_j$ , and  $\Phi_{s,j}$ ). [37]

### Accuracy of the P2D model

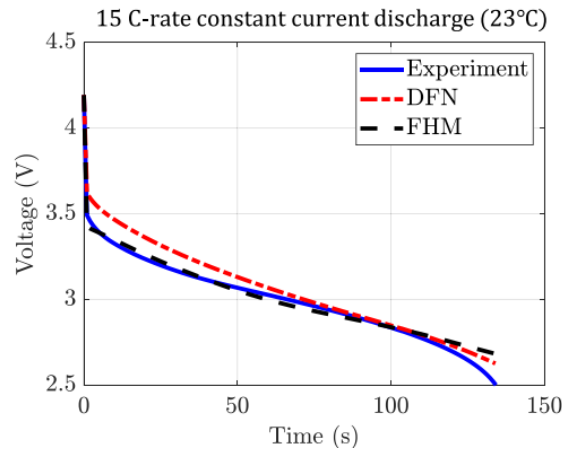
The P2D model is widely used in battery modelling due to its high accuracy at a wide range of charge/discharge current densities. This can be validated from the study by Arunachalam and colleagues [8], where several comparisons were performed between the P2D (named Doyle-Fuller Newman (DFN) in their study) and experimental data of the real battery used. A Full Homogenized Macroscale (FHM) was also included for comparison in this study, however, the focus in this section is on the accuracy of the P2D (DFN) model with respect to experimental data.

Looking at the terminal voltage data for 1C constant discharging experiment (at 23° C) in Fig.2-3 (a), it can be seen that the P2D model voltage data follows the experimental data in a one to one fashion. Even when increasing the C-rate to 15C as shown in Fig.2-3 (b), it can be seen that while the accuracy of the P2D (DFN) model slightly drops with respect to the experimental data, the dynamical behaviour is still followed with high accuracy.

As a result, from the study made by Arunachalam and colleagues [8], it can be concluded that the P2D model is applicable up to a current C-rate of 15C. Since such a range is higher than any range that batteries can withstand, thus the P2D model is used as a base for comparison in thesis for less accurate models, rather than experimental data, due to unavailability of an experimental setup.



**(a)** Terminal Voltage (V) vs time  $t$  (s) plot for the experiment, FHM and P2D (DFN) model data at 1C constant discharging experiment. [8]



**(b)** Terminal Voltage (V) vs time  $t$  (s) plot for the experiment, FHM and P2D (DFN) model data at 15C constant discharging experiment. [8]

**Figure 2-3:** Comparison between experimental, P2D (DFN) and FHM for the terminal voltage (V) against time (s) for the different constant charging experiments [8].

### Computational aspects of the P2D model

Although the P2D model is a useful tool due to its high accuracy for a wide range of currents, it has some drawbacks. First of all, it is computationally expensive as it involves solving a set of tightly coupled, high order Partial Differential Equation (PDE). One example of a high order PDE in the P2D model can be found in Eq.2-1, where the second order dependency with radius as well as the dependency with time with such boundary conditions makes the PDE extremely difficult to solve. In fact, no analytical solution is yet to be available for the P2D model [24] [12]. The numerical methods that solve such a PDE for all solid particles are slow, making feasibility for realtime control applications difficult for such a complex model.

Rahimian and colleagues [36] simulated the P2D model for multiple discharge rates, and it showed an average runtime of 11.2 s for simulating 4000s, making it infeasible for some applications such as real time control [29]. In addition, applying a Kalman filter would be difficult for such a highly complex model.

Since an analytical solution is unavailable for the model, several numerical methods to solve the P2D model have been developed in literature. The main methods include Finite-Difference method, Finite-Element method, Finite-Volume method and orthogonal projection method [34]. Finite-Difference and Finite-Volume methods are the most widely used as they can be solved efficiently by commercial software. Commercial software is generally used to simulate complex geometries and batteries, for example COMSOL and AutoLion [15] [36].

Recent efforts have been made to tackle the issue of the high computational time of the P2D model by either simplifying this model using model order reduction techniques or finding faster numerical methods than the ones mentioned above [29]. The main focus of this literature will be on reduced order models rather than going in depth on numerical solutions. One of the most common models would be the Electrolyte Enhanced Single Particle Model (SPMe). An analytical solution exists under some conditions and has computational time is similar to that of equivalent circuit models [29], thus solutions can be found almost instantly in some cases. It will be explained in detail in the next section.

### 2-1-2 Electrolyte Enhanced Single Particle Model (SPMe) [28]

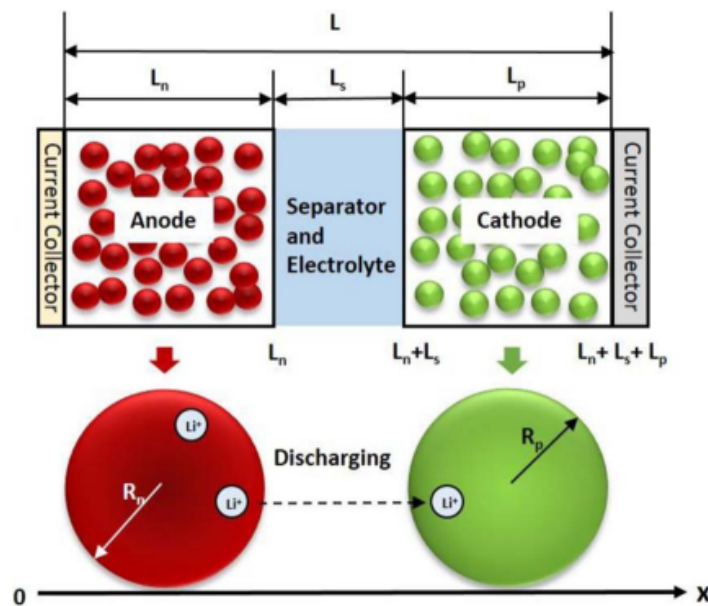


**Figure 2-4:** Schematic of the P2D and Single Particle (SP)/SPMe models of a lithium ion battery. [40]

As an attempt to make a lower order model than the P2D model, the SP model was developed [28]. In the SP model, both electrodes are considered to be spherical particles with equal size due to the fact that it is assumed that current is uniformly distributed across all particles in the electrode. This heavily simplifies the dynamics of the model as the reactions such as

diffusion, transportation, diffusion induced stress are taken to have a uniform impact on each particle [39]. The schematics showing the differences between the P2D and the SP model can be found in Fig.2-4. On the other hand, the assumption made on the fact that the electrolyte concentration is assumed to be a constant value limits the applicability of the model at high charge/dicsharge current rates [28].

As a result the SPMe was developed, which has the same solid phase dynamics as the SP, with the inclusion of a dynamical model for the electrolyte dynamics, similar to that of the P2D model.

### Solid Phase Dynamics

In recent research, an improved version of the SP model called the SPMe which incorporates electrolyte dynamics has been developed. The solid phase diffusion dynamics are governed by Fick's second law [54], given by,

$$\frac{\partial c_{s,j}}{\partial t} = \frac{D_{s,j}}{r^2} \frac{\partial}{\partial r} \left( r^2 \frac{\partial c_{s,j}}{\partial r} \right), \quad (2-14)$$

where  $c_{s,j}$  is the concentration of lithium ions in the solid phase,  $t$  is time,  $r$  is the radial position in the sphere,  $D_{s,j}$  is the temperature dependent solid phase diffusion coefficient and the subscript  $j = +/ -$  represents the positive/negative electrode. The initial and boundary conditions for the equation above are given by,

$$c_{s,j}(t = 0) = c_{s,0,j}, \quad (2-15)$$

$$\left( D_{s,j} \frac{\partial c_{s,j}}{\partial r} \right)_{r=0} = 0, \quad (2-16)$$

$$\left( D_{s,j} \frac{\partial c_{s,j}}{\partial r} \right)_{r=R_j} = -j_j, \quad (2-17)$$

where  $j_j$  being the molar flux at the surface of the sphere at the solid-electrolyte interface. In order to couple the solid phase with the solution phase, the Butler-Volmer equation is used as in the P2D model [20] in Eq.2-4. The state of charge per electrode,  $SOC_j$ , is given as the ratio of the solid phase concentration  $c_{s,j}$  in electrode  $j$ , with the maximum solid phase concentration  $c_{s,j,max}$  in electrode  $j$ , given as,

$$SOC_j = \frac{c_{s,j}}{c_{s,j,max}}. \quad (2-18)$$

The initial and surface state of charge is given as,

$$\begin{aligned} SOC_{0,j} &= \frac{c_{s,0,j}}{c_{s,j,max}}, \\ SOC_{j, surf} &= \frac{c_{s,j}|_{r=R_p}}{c_{s,j,max}}. \end{aligned} \quad (2-19)$$

### Electrolyte Phase Diffusion Dynamics

The liquid/electrolyte phase diffusion dynamics and boundary conditions are as follows,

$$\begin{aligned} \frac{\partial (\varepsilon_e c_{e,j})}{\partial t} &= \frac{\partial}{\partial x} \left( D_{e,j}^{\text{eff}} \frac{\partial c_{e,j}}{\partial x} \right) + \frac{1 - t_+^0}{F} j_j, \\ \frac{\partial c_{e,j}}{\partial x} \Big|_{x=0} &= \frac{\partial c_{e,j}}{\partial x} \Big|_{x=L} = 0, \end{aligned} \quad (2-20)$$

where  $c_{e,j}$  is the lithium ion concentration in electrolyte,  $\varepsilon_e$  is the electrolyte phase volume fraction,  $D_{e,j}^{\text{eff}}$  is the effective electrolyte phase  $Li^+$  diffusion coefficient.  $t_+^0$  is the transference number  $j_j$  is defined as the molar flux in the electrolyte at electrode  $j$ , given by Eq.2-4. In literature, the intercalation molar flux  $j_j$  for the SPMe and approximate versions of it is often approximated from Eq.2-4 to the following,

$$j_{\pm} = \frac{\mp I}{F \cdot a_{\pm} \cdot L_{\pm}}, \quad (2-21)$$

when electrode surface variables are only considered.

### Voltages and Potentials

The voltages and potentials for the SPMe are taken to be the same as the P2D model from Eq.2-10 to Eq.2-13.

### Accuracy of the SPMe

Since the P2D model was determined to be highly accurate for a wide range of charge densities, the accuracy of the SPMe can be determined by comparing it with the P2D model. This has been done in a previous study by Luo and colleagues [50], where as seen in Fig.2-5, the molar fluxes for the P2D model, SP model and the SPMe under 1C, 3C and 4C Constant-Current Constant-Voltage (CCCV) charging and discharging strategies [50]. Under 1C charging/discharging, it can be noticed from Fig.2-5 (a) and Fig.2-5 (b) that the SPMe (red line) molar flux follows the same trajectory as the P2D model (blue line) with high accuracy, where charging at 1C in Fig.2-5 shows almost a one to one similarity, whereas for 1C discharging there are minor deviations, but the shape is still followed. As for the SP model, due to the fact that the the electrolyte concentration is modelled as a constant, the molar flux under all charging/discharging rates will be a constant, which is seen in all plots in Fig.2-5. For 3C CCCV charging and discharging in Fig.2-5 (c) and Fig.2-5 (d) respectively, when comparing the SPMe with the P2D molar fluxes, both trajectories follow each other, however, with lower accuracy compared to 1C. Again for 3C charging/discharging, the SP molar flux is constant at all times. Lastly, for 4C charging and discharging in Fig.2-5 (e) and Fig.2-5 (f) respectively, it can be seen that the SPMe molar flux shows a similar shape to the P2D model, however, there is a large deviation in magnitude between the two models across the charging/discharging period.

Another measure for determining the accuracy of the SPMe is comparing the terminal voltage at multiple C-rates across the charging/discharging period to models which are known to be

highly accurate, such as the P2D model. This has been done previously as seen in Fig.2-6, where the terminal voltage was plotted against time for the P2D, SP and the SPMe models at 1C, 3C and 4C discharging rates [50]. The deviation in the terminal voltage between the SPMe and P2D as well between the SP model and P2D model for the 1C, 3C and 4C rates were also plotted in Fig.2-6. Starting with the terminal voltage at 1C discharge in Fig.2-6 (a), it can be seen that for both the SP and SPMe models, the shape of the voltage profile is followed where all lines overlap across the discharging period. However, the deviation plot in Fig.2-6 (b) shows that the SP model deviates more with respect to the P2D model, with a maximum deviation of around 0.027 V, compared to a maximum of around 0.003 V in the SPMe. At 3C discharge, it is more evident in the terminal voltage plot against time in Fig.2-6 (c) that the SP model fails to follow the P2D model, whereas the SPMe model follows the P2D model in almost a one to one fashion. The terminal voltage deviation plot in Fig.2-6 (d) further proves this, with the SP model having a maximum deviation of around 0.08 V with respect to the P2D model, whereas the SPMe has a maximum deviation magnitude of 0.02 V. Lastly, at 4C discharge, the terminal voltage plot in Fig.2-6 (e) shows that SP model completely fails to follow the same trajectory as the P2D model across the whole discharging period, whereas the terminal voltage for the SPMe model follows that of the P2D model, with some deviations between the times 4 min and 6 min. The terminal voltage deviations in Fig.2-6 (f) show that the SP model at this C-rate becomes highly inaccurate, having a maximum deviation magnitude of 0.45 V with respect to the P2D, whereas the SPMe still shows good performance with a maximum deviation of 0.08 V. As a result, it was concluded in [50] that the SP model can be only be used for up to 1C charge/discharge and the SPMe model can be used for up to 4C charge/discharge rates.

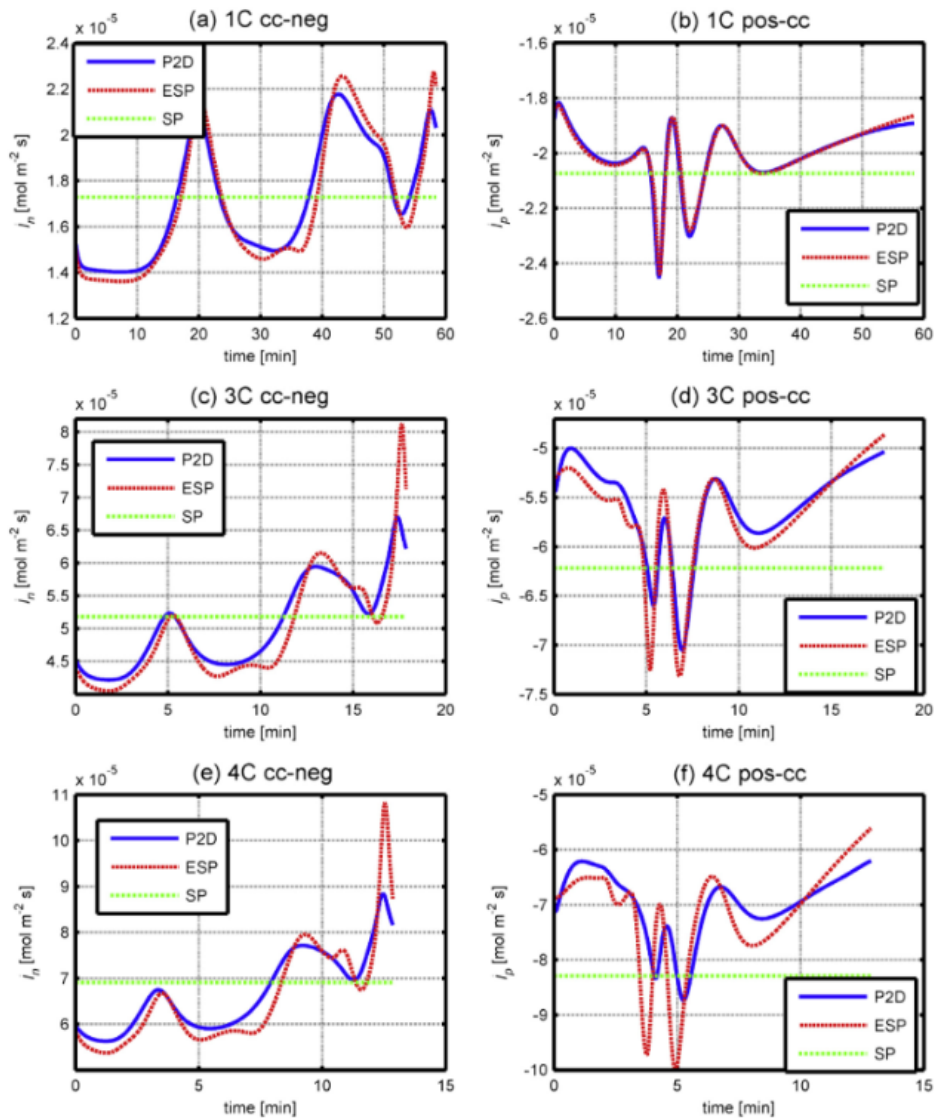


**Figure 2-5:** Comparison of the pore wall fluxes at the cc-neg interface and the pos-cc interface simulated by SP, SPM (ESP) and P2D models under 1C ((a) and (b) respectively) 3C ((c) and (d) respectively) / 4C ((e) and (f) respectively) rate discharges. [50].

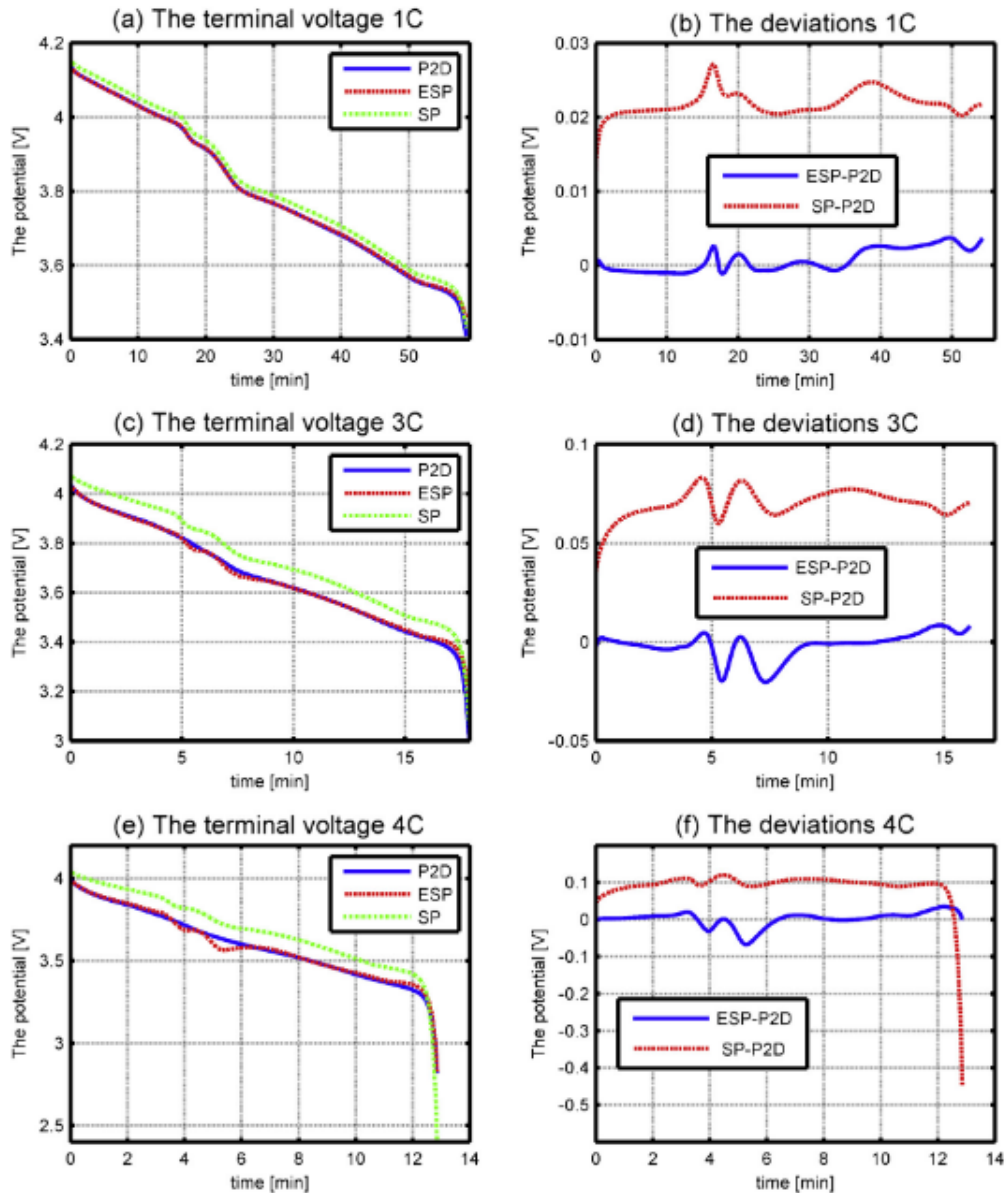


**Figure 2-6:** Plots of the terminal voltage profiles simulated by SP,SPMe (ESP) and P2D models and the corresponding deviations under 1C ((a) and (b) respectively), 3C ((c) and (d) respectively) and 4C ((e) and (f) respectively) rate discharges. [50].

### Computational aspects of SPMe

The main advantage that lies in the SPMe compared to more accurate models is its low complexity. The low complexity allows for an analytical solution to exist, and has one of the fastest simulation speeds amongst other models. In previous research by Luo and colleagues [50], multiple simulations for the SP, SPMe and P2D at different discharge/charge rates were performed, as seen in Fig.2-7. Looking at the experiment that took the longest simulation time, being the 4C Federal Urban Driving Schedule (FUDS), it can be seen that the simulation

time obtained for the SPMe (ESP) model was 527.43 ms, 1006 times faster than the P2D with a simulation time of 530.7 s and 14.9 times slower than the SP model, with a simulation time of 35.247 ms. Although the SPMe model is significantly faster than P2D model, in some cases the simulation times are high enough such that real time control would not be applicable. As a result, efforts to further reduce the complexity of the SPMe model have been made which simplifies the dynamics from polynomial order Partial Differential Equations (PDEs) to be first order Ordinary Differential Equations (ODEs) while keeping the accuracy similar to the SPMe. In the next section, the Extended Single Particle Model (ESPM) will be discussed.

Operating conditions	SP	ESP	P2D	Ratio (ESP/P2D)	Ratio (ESP/SP)
1C discharge	0.758 ms	10.55 ms	11.15 s	1/1057	13.9
2C discharge	1.421 ms	15.56 ms	16.85 s	1/1083	11.0
3C discharge	4.534 ms	56.31 ms	59.18 s	1/1051	12.4
4C discharge	6.777 ms	91.09 ms	94.34 s	1/1036	13.4
0.5C CCCV charge	2.901 ms	33.61 ms	31.75 s	1/945	11.6
4C DST	1.601 ms	22.08 ms	19.91 s	1/902	13.8
4C FUDS	35.247 ms	527.43 ms	530.77 s	1/1006	14.9

**Figure 2-7:** The computation times of SP, SPMe (ESP) and P2D models. [50].

### 2-1-3 The Extended Single Particle Model (ESPM)

The SPMe is widely used in literature for its fast computation times which allow the application of various real time control techniques, such as Model Predictive Control (MPC). However, from the previous section it was concluded that in some cases, the simulation time can be high enough such that real time control cannot be used. As a result, recent efforts have been made in literature to overcome such a limitation by extending to the SPMe and making assumptions on what shape of the **solid phase** concentration profiles might look like. The method that is discussed is called polynomial profile approximation [34]. Polynomial profile approximation assumes that the solid phase concentration has an n-th order shape, then using a volume averaging technique, a the concentration and rate of change of concentration are averaged across the volume of the sphere. Using this method, the solid phase SPMe dynamics are reduced from a PDE that has a second order dependency on the sphere radius and first order dependency on time, to a linear state space model. The performance of multiple orders of polynomial profile approximations will be discussed. As for the electrolyte phase dynamics in SPMe, they are either kept unchanged in the ESPM, or they are approximated using various approximation techniques which reduces the electrolyte dynamics to first order ODEs [44], [83] and [78].

#### Solid Phase Diffusion Dynamics

One variant of the polynomial profile approximation for the solid phase diffusion dynamics is the 2-term polynomial approximation, where the solid phase concentration at electrode  $j$ ,  $c_{s,j}$ , is assumed to have a parabolic concentration profile as follows,

$$c_{s,j}(r, t) = a(t) + b(t) \left( \frac{r^2}{R_p^2} \right), \quad (2-22)$$

$$\frac{da(t)}{dt} + \frac{r^2}{R_p^2} \frac{db(t)}{dt} - \frac{6D_{s,j}b(t)}{R_p^2}, \quad (2-23)$$

where  $a(t)$  and  $b(t)$  are constants to be determined for each electrode  $j$ . The boundary condition at  $r = 0$  is automatically satisfied. The boundary condition at  $r = R_p$  becomes

$$2\frac{D_{s,j}}{R_p}b(t) = -j_j \quad (2-24)$$

Since the most important solid phase terms in battery modelling are the volume averaged solid concentration at electrode  $j$ ,  $\bar{c}_{s,j}$ , and the surface concentration at electrode  $j$ ,  $c_{s,\text{surf},j}$  to monitor electro-chemical behaviour,  $c_{s,j}$  is averaged across the volume of the sphere as follows,

$$\bar{c}_{s,j}(t) = \int_{r=0}^{R_p} 3\frac{r^2}{R_p^2}c_{s,j}(r,t)d\left(\frac{r}{R_p}\right). \quad (2-25)$$

Placing Eq.2-22 in Eq.2-25, the following is obtained,

$$\bar{c}_{s,j}(t) = a(t) + \frac{3}{5}b(t) \quad (2-26)$$

Evaluating  $c_{s,j}(r,t)$  in Eq.2-22 at the surface of the sphere, the surface concentration  $c_{s,\text{surf},j}$  is obtained,

$$c_{s,\text{surf},j}(t) = a(t) + b(t) \quad (2-27)$$

Solving for  $a(t)$  and  $b(t)$  in Eq.2-26 and Eq.2-27,

$$\begin{aligned} a(t) &= -\frac{3}{2}c_{s,\text{surf},j}(t) + \frac{5}{2}\bar{c}_{s,j}(t) \\ b(t) &= -\frac{5}{2}\bar{c}_{s,j}(t) + \frac{5}{2}c_{s,\text{surf},j}(t) \end{aligned} \quad (2-28)$$

Now,  $c_{s,j}$  can be written in terms of the volume-averaged- concentration  $\bar{c}_{s,j}$  and the surface concentration  $c_{s,\text{surf},j}$  as follows,

$$c_{s,j}(r,t) = -\frac{3}{2}c_{s,\text{surf},j}(t) + \frac{5}{2}\bar{c}_{s,j}(t) + \left(-\frac{5}{2}\bar{c}_{s,j}(t) + \frac{5}{2}c_{s,\text{surf},j}(t)\right)\frac{r^2}{R_p^2}. \quad (2-29)$$

To obtain 2 equations that show the evolution of both  $\bar{c}_{s,j}$  and  $c_{s,\text{surf},j}$ , the solid phase concentration evolution equation from the SPMe in Eq.2-14 is volume averaged as follows,

$$\int_{r=0}^{R_p} 3\frac{r^2}{R_p^2} \left[ \frac{\partial c_{s,j}}{\partial t} - D_{s,j} \frac{1}{r^2} \frac{\partial}{\partial r} \left( r^2 \frac{\partial c_{s,j}}{\partial r} \right) \right] d\left(\frac{r}{R_p}\right) = 0. \quad (2-30)$$

Plugging in Eq.2-29 in Eq.2-32,

$$\frac{d}{dt}\bar{c}_{s,j}(t) + 3\frac{j_j}{R_p} = 0. \quad (2-31)$$

To obtain  $c_{s,\text{surf},j}$ , Eq.2-22 is evaluated using Eq.2-28, we get

$$\frac{D_{s,j}}{R_p} [c_{s,\text{surf},j}(t) - \bar{c}_{s,j}(t)] = -\frac{j_j}{5} \quad (2-32)$$

## Electrolyte Phase Diffusion Dynamics

As for the electrolyte phase dynamics, they are either kept unchanged as in Eq.2-20 to Eq.2-21, or they are approximated using multiple techniques found in literature. One example of an approximation is by using concentration data from the full order P2D model, giving rise to a first order transfer function [44] given by,

$$G(s) = \frac{c_{e,\text{surf},j}(s)}{c_{e,\text{surf},\text{eq},j}(s)} = \frac{1}{\Delta T_j s + 1}, \quad (2-33)$$

where  $c_{e,\text{surf},j}(s)$  is the instantaneous electrolyte concentration (in Laplace domain) near current collector of electrode  $j$ .  $c_{e,\text{surf},\text{eq},j}(s)$  is the equilibrium electrolyte concentration at a given charge rate near current collector of electrode  $j$ .  $\Delta T_j$  is the time constant for the diffusion dynamics.

## Accuracy of different types of ESPM

In this section, the accuracy of the polynomial profile approximation for the SPMe is analyzed and compared with experiments.

First of all, a previous study by Lin and colleagues [44], implemented a 2-term polynomial approximation for the solid phase diffusion dynamics, whereas for the electrolyte phase dynamics, the electrolyte dynamics found in the original SPMe [40] were simplified into a first order Ordinary Differential Equation (ODE) using a first order transfer function arising from the electrolyte concentration as well as equilibrium electrolyte concentration at the anode current collector surface.

It can be seen from Fig.2-8, that the cell voltage was plotted against time for a charge current range between 0C and 6C. At 6C, in the first 50s of the charging, it can be noticed that the shape of the cell voltage is followed comparing simulation to experiment, but there is a deviation in magnitude indicating that the model would not be accurate for charging at 6C for a prolonged time. After 50s, the current is instantly dropped to 3C, and it can be seen that the model shows high accuracy compared to the experiment for the rest of the charging period.

The model was then tested for a charging profile, as seen in Fig.2-9. At 5C charging in the first 50s, the cell voltage shape follows is similar for both the simulation and the experiment with minor deviations in magnitude. For the rest of the charging period when the charge current is reduced, the simulation emulates the experiment with high accuracy. To conclude, the model has very high accuracy for current rates up to 3C, moderate accuracy up to 5C and low accuracy beyond 5C.

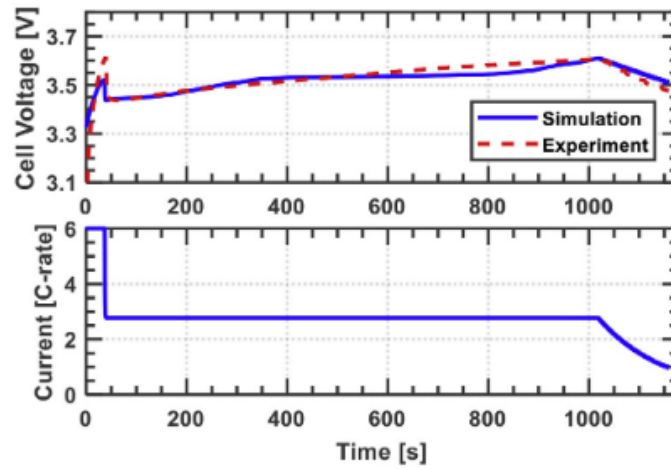


**Figure 2-8:** Plot of cell voltage (V) against time (s) and a current profile (C-rate) against time (s) for the ESPM model (blue) as well as experimental data (red). [44]

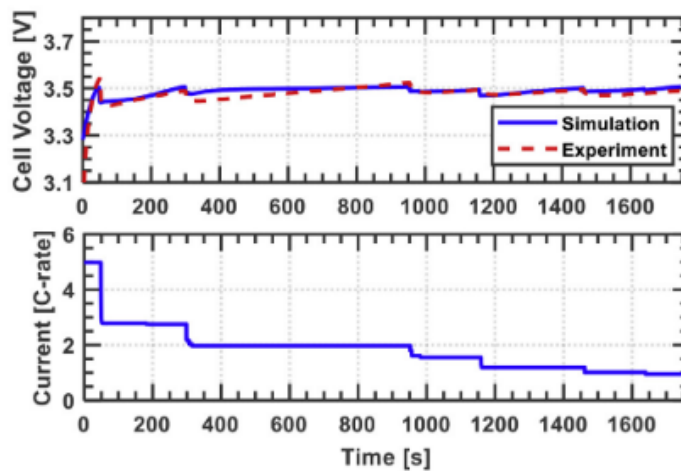


**Figure 2-9:** Plot of cell voltage (V) against time (s) and a current profile (C-rate) against time (s) for the ESPM model (blue) as well as experimental data (red) [44]

Another study by Yin and colleagues [78] used a 3-term polynomial approximation for the solid phase diffusion dynamics, whereas for the electrolyte diffusion dynamics, it was approximated to a first order 5-state state space model [78] [65]. It can be seen in Fig.2-10, that the reduced order model terminal voltage was plotted against experiment for charging (left plot) and discharging (right plot) current rates ranging from 1C to 6C, where there is almost a one to one resemblance in the shape and magnitude of the simulation compared to the experimental data. As a conclusion, the 3 parameter model shows higher accuracy than the 2 parameter model for a wider current range, and the 3 parameter model shows very high accuracy for a C-rate range of until at least 6C.

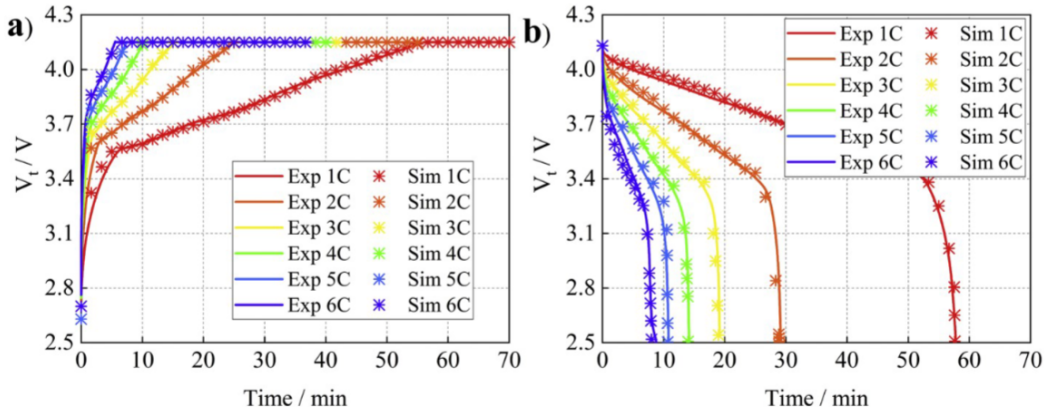


**Figure 2-10:** Plot of the terminal voltage (V) against time (s) for charging (left plot) and discharging (right plot) cases for both the ESPM and experimental data at charge/discharge rates ranging from 1C to 6C. All curves overlap. [78]

### Computational aspects of ESPM

Previous research has analyzed the computational price of the ESPM has been analyzed. In a previous study by Li and colleagues [38], a 3-term polynomial approximation for the solid phase diffusion dynamics has been implemented for an SPMe model. For the electrolyte dynamics, a polynomial profile approximation was implemented for the electrolyte concentration [38]. It was then analysed and compared with the P2D model on the basis of computational complexity as seen in Fig.2-11. The low computational complexity in the reduced-order SPMe model (ROEM) is evident, having a maximum computational time 22.3 ms for a duration time of 14547 s under 2C FUDS experiment conditions. This is 3596 times faster than the P2D model, with a computational time of 80.18 s for the 2C FUDS experiment conditions. Comparing this ratio with maximum ratio in computational time between the P2D and SPMe (ESP) being 1083 as seen in Fig.2-7 under 2C discharge experiment conditions, it can be concluded that reduced order SPMe model is computationally lighter than the unapproximated SPMe. For all cases presented in Fig.2-11, it can be seen that such a model is suitable for real time control, with an average computational time of 18.25 ms, for duration of at least 242.45 minutes, being the maximum duration time found in Fig.2-11. As a result, since the 3-term polynomial approximation of the solid phase diffusion dynamics in the SPMe was found to be accurate enough to be used for a wide range of charging/discharging currents up to at least 6C, as well as being computationally light enough for real time control even for duration times as high as 242.45 minutes, it will be the model of choice moving forward with the thesis.

Conditions	Duration-time	ROEM	P2D	Ratio (P2D/ROEM)
0.5C Disch.	7092 s	18.5 ms	39.15 s	2116
1 C Disch.	3407 s	17.5 ms	19.93 s	1139
1.5C Disch.	2101 s	16.4 ms	13.51 s	824
2 C Disch.	1417 s	15.7 ms	9.73 s	620
2 C FUDS	14547 s	22.3 ms	80.18 s	3596
2C UDDS	7769 s	19.1 ms	44.01 s	2304

**Figure 2-11:** Computational times of a reduced order ESPM model (ROEM) and P2D model under different experiment conditions. [38]

### 2-1-4 Conclusion

In this chapter, the P2D, SPMe and ESPM models have been presented in detail and compared with each other in terms of accuracy across a range of charge/discharge current densities, as well as the computational complexity of each model.

For the P2D model, it was shown that while it has the highest accuracy, it cannot be used due to the high computational complexity, making it infeasible for real time control applications. The SPMe and ESPM significantly lower computational time than the P2D model, and real time control is applicable. Among SPMe and ESPM, the ESPM showed the highest accuracy. As a result, the best trade-off achieved between accuracy and computational complexity is the ESPM, which will be the model of choice moving forward in the thesis.

## 2-2 Li-ion Battery Degradation Models

### 2-2-1 Description

A key component in battery modelling to depict the dynamics as accurately as possible is incorporating capacity fade in the model. Before introducing the model, the key aspects of degradation need to be discussed. These are loss of lithium inventory, loss of active material in the anode and loss of active material in the cathode [10].

First of all, the loss of lithium material includes the loss of lithium ions due to parasitic reactions such as Solid Electrolyte Interphase (SEI) growth, lithium plating, decomposition reactions etc. These types of reactions are irreversible and their main causes are time, high temperatures, high current loads and high ratio between open circuit voltage and the State Of Charge (SOC). Loss of active material in the anode is material that is no longer available for insertion of lithium due to particle cracking, loss of electrical contact or blocking of sites in the anode that used to be active in the resistive surface layers [10]. Loss of active material in the cathode is active mass that is no longer available in the cathode due to unusual changes in the structure particle cracking or electrical contact loss. A summary of the different types of degradation mechanisms can be found in Fig.2-12.

With all the degradation mechanisms mentioned previously, the most dominant aging mechanism in the early charge/discharge cycles is said to be the growth of SEI [76]. It is a layer formed on the anode in the early stages of the charging process. For the SEI growth dynamics, it is mainly affected by activity on the film surface, such as surface kinetics and diffusion rate of Ethyl Carbonate (EC) at the film surface [62]. As a result, the dynamics

of the SEI formation is governed by the tafel kinetics at the anode [57]. On the other hand, in recent studies [13], [81], it was shown that the nonlinear aging behaviour after prolonged cycling is not dominated by SEI growth, but rather lithium plating. It is one of the main aging processes in the later stages of cycling as to lithium plating may not only promote further degradation, but it may also have a negative impact on the safety of LiBs [7]. During fast charging, lithium-ions can be deposited on the surface of the graphite anode rather than being intercalated into the interstitial space between the graphite anode's atomic layers [17]. In general, the deposited lithium can be reversible or irreversible. The irreversible portion can react with the electrolyte to form a secondary SEI layer, or it can form a high-impedance "dead" lithium film that is electrically isolated from the graphite anode and remains irreversible, increasing internal resistance. As a result, it can be concluded that the linear aging in the early cycles of the li-ion battery life is dominated by the SEI growth dynamics, whereas the nonlinear aging behaviour near the end of the life of the battery is dominated by lithium plating. The main focus of this literature would be discussing and analyzing physics based models that capture SEI growth and lithium plating dynamics.

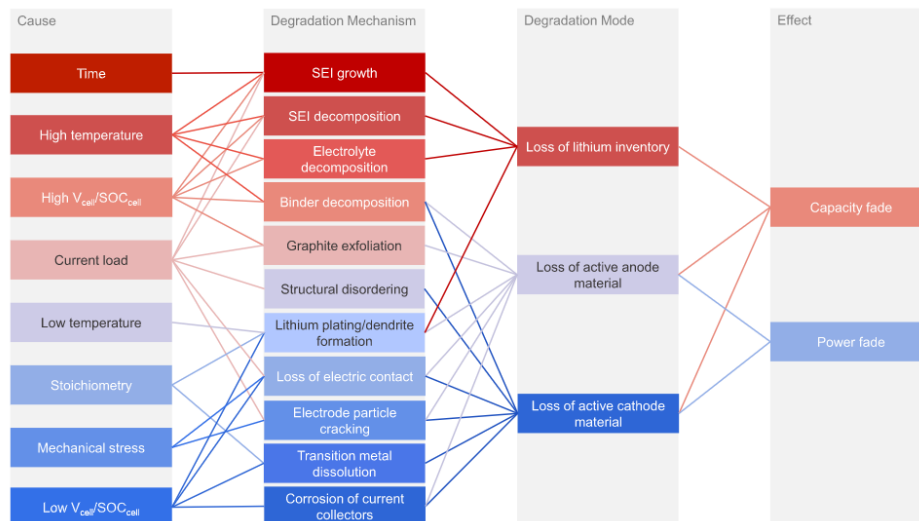


**Figure 2-12:** A summary of the degradation mechanisms for the Li-ion battery [10]

This is now changed to  $j_{tot}$  since it will include the flux arising from the SEI growth as well as the lithium plating mechanisms. In this case, a simplified P2D thermal model that is considered as the degradation model is incorporated on such battery model [76]. However, any of the electro-chemical battery models discussed in section 2 can be applied on the degradation model too. Since this has been implemented from scratch during the thesis, it is included in the model implementation chapter from Eq.3-12 to Eq.3-20

### 2-2-2 Accuracy of degradation model

In the same research [76], the accuracy of the degradation model incorporated in an electrochemical-thermal model in their previous work [26] [68] has been tested. The comparison was made

with experimental data, where the experiment was performed on a Li-ion pouch cell fabricated by EC power for plug-in Electric Vehicle (EV) applications.

The variables that were compared against experimental data can be found in Fig.2-13 where the cell voltage is plotted against the discharge capacity (Ah) at the different stages of the age of the battery, for (a) a C/3 discharge rate, (b) 1C discharge rate, (c) 2C discharge rate and (d) 3C discharge rate. Starting with Fig.2-13 (a), (b), (c), it can be seen that the battery model with degradation accurately depicts the cell voltage with respect to the discharge capacity at C/3, 1C and 2C, where the experimental data is followed with similar accuracy at the different stages of the battery life cycle. On the other hand, at a discharge rate of 3C as in Fig.2-13 (d), the battery model with degradation accurately represents the cell voltage with respect to the discharge capacity until a cycle number of around 2900. The model fails at a high discharge rate of 3C, when the battery starts showing highly nonlinear behaviour at the end of the battery life at a cycle number of 3300. The voltage undershoot behaviour that occurred at cycle 3300 Fig.2-13 (d) was said to be associated to cells discharging at low temperatures [76], and poor electrolyte performance at freezing temperatures.

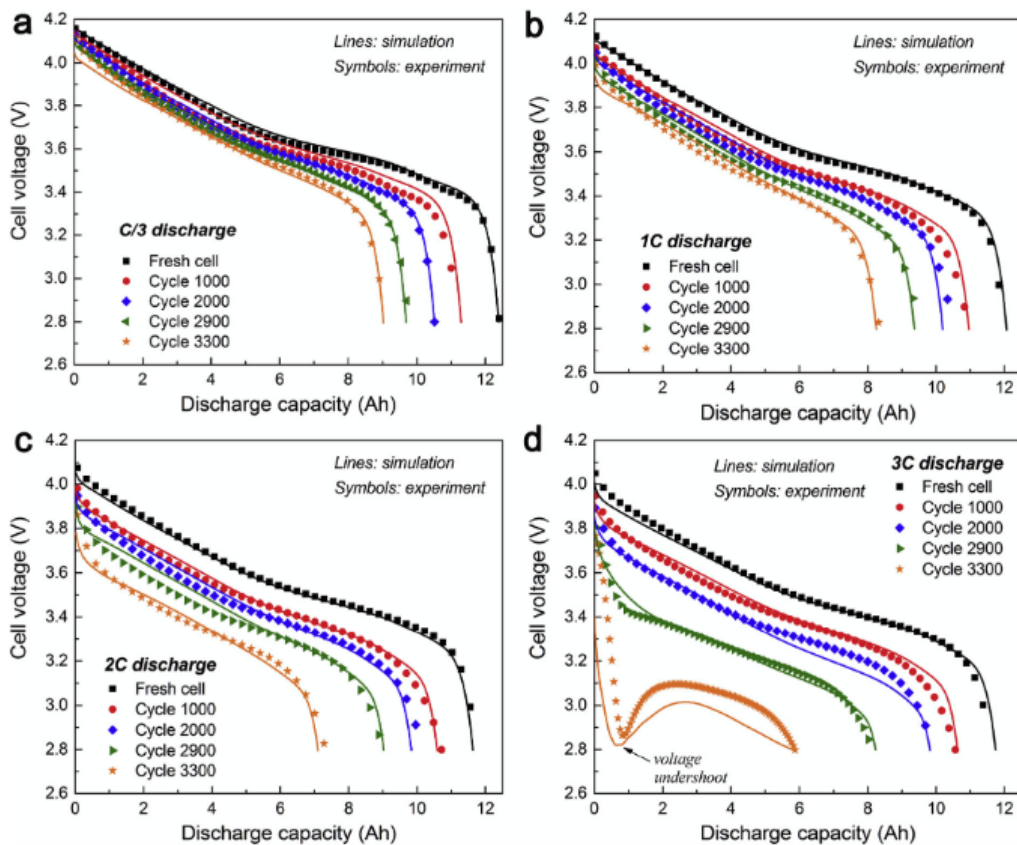


**Figure 2-13:** Comparison of model results with experiment data in terms of discharge curves at (a) C/3 (b) 1C (c) 2C and (d) 3C measured in the reference performance tests of the cell after different number of cycles. [76]

### 2-2-3 Other Methods in Literature

Examples of physics based degradation models include [58], where a solvent diffusion model to capture the SEI growth behaviour in Li-ion cells incorporating the carbon anodes was introduced. The model predicted that the SEI thickness increases proportionally with the square root of time. Moreover, a phase field model was developed to simulate the micro-structure morphology evolution that happens during SEI growth [27]. To incorporate thermal effects, the SEI growth dynamics were modelled using a one dimensional thermal-electrochemical model [48]. In addition, a statistical physics based model based on the Fokker-Plank equation [55] is used to model SEI growth [71]. Studies attempted to depict more accurately the SEI thickness evolution by including stress generation effects on the SEI growth [60]. There are other studies on the different modelling methods for degradation, specifically SEI growth

## 2-3 Charging Strategies

### 2-3-1 Introduction

Based on the electro-chemical battery model as well as the degradation model chosen, the charging strategy to be chosen should align with such models. Based on the choice, the charging strategy needs to follow certain criteria. First of all, the control mechanism needs to be implementable in real time in order apply such control strategy in real world applications. This means that the battery model chosen must be computationally light or can be simplified to have low simulation times as well as relatively high accuracy. As a result, a strategy based on the SPMe or the ESPM would be the model of choice. The second criteria would be that the control strategy should have the objectives of minimizing the aging/degradation of the battery as well as minimizing the charging time. Lastly, the strategy chosen should have been validated experimentally and have proven results. Based on these criteria, the following representative charging strategies are chosen from previous research.

### 2-3-2 Method 1 [44]

The first discussed charging strategy used uses a variant of the ESPM where it uses a 2 term polynomial approximation of the solid phase diffusion dynamics [44]. The electrolyte dynamics were simplified by obtaining a static map from the full order P2D model of their previous work [46] which predicts the Li-ion concentration at the surface of the anode collector with respect to the charge rate. From there, a first order transfer function was obtained that predicts the instantaneous electrolyte concentration when given an input equilibrium concentration. As for the degradation mechanisms, an electro-chemical model based on [76] was used to obtain a 3D static maps that show SEI and lithium plating growth as a function of the charge rates and SOC in the battery model. The static maps represented the degradation (SEI or Lithium plating growth) mechanism rate at a given charge rate as well as anode SOC. Finally, the charging strategy previously proposed in is an open-loop optimization based strategy which aims to minimize the following cost function [44],

$$\min_{I(t), I_f} \int_{t_0}^{t_f} (\alpha \cdot 1 \cdot dt + \beta \cdot f_{SEI}(t) \cdot dt + \gamma \cdot f_{\text{plating}}(t) \cdot dt), \quad (2-34)$$

where  $(t_f - t_0)$  is the charge time,  $f_{SEI}(t)$  is the SEI growth rate,  $f_{plating}(t)$  is the lithium plating rate,  $\alpha, \beta, \gamma$  are the weighting factors to penalize charging time, SEI growth rate and Lithium plating accordingly. The optimization variables are the input current  $I(t)$  and final time  $t_f$ , with the state variables,  $x_{i,avg}$  (electrode SOC) and  $c_{e,j}$  (electrolyte concentration). The cost function was further simplified by converting from the time domain to the SOC domain. To do so, the anode SOC is divided into small  $\Delta SOC$  intervals, where in each interval the following variables are computed,

$$\begin{aligned} t_{char} &= \frac{\Delta SOC \cdot S_- \cdot F \cdot R_p \cdot c_{s,-,max}}{3 \cdot I(SOC)}, \\ \delta_{SEI} &= f_{SEI}(SOC, I) \cdot t_{char}, \\ \delta_{plating} &= f_{plating}(SOC, I) \cdot t_{char}, \end{aligned} \quad (2-35)$$

where  $t_{char}$  is the charge time for the segment  $\Delta SOC$ ,  $f_{SEI}$  is the SEI growth rate,  $f_{plating}$  is the lithium plating rate. This leads to the following cost function,

$$\min_{I(SOC)} \int_{SOC_{lo}}^{SOC_{hi}} (\alpha \cdot t_{char} + \beta \cdot \delta_{SEI} + \gamma \cdot \delta_{plating}), \quad (2-36)$$

where anode electrode  $SOC_{lo} = 0.017$  (fully discharged) and  $SOC_{hi} = 0.61$  (fully charged). It can be seen now that the thickness of the SEI layer  $\delta_{SEI}$ , thickness of the lithium plating layer  $\delta_{lpl}$  and charging time  $t_{char}$  are minimized in the new control problem, and the optimization variables reduce to be only the input charging current  $I(SOC)$  and now the electrolyte concentration  $c_e$  is the only state variable which increases the complexity of the control problem. After the time to SOC conversion, the state variable SOC is eliminated, and optimization variable  $t_f$  is also eliminated. The optimization variable is now the input current  $I(SOC)$  only. The only state variable is the electrolyte concentration  $c_e$  near the anode current collector. The above time to SOC conversion technique simplifies the optimal control problem significantly.

The optimal control problem has the following constraints on the maximum discharge current, the normalize solid surface concentration in each electrode  $x_{-,surf} = \frac{c_{s,surf,-}}{c_{s,max,-}}$  and  $x_{-,surf} = \frac{c_{s,surf,+}}{c_{s,max,+}}$ , also known as the surface SOC, and the terminal cell voltage  $V_{cell}$ ,

$$\begin{aligned} 0 &< I(SOC) \leq I_{max}, \\ c_{e,j} &> 0, \\ 0 &\leq x_{-,surf} \leq 1, \\ 0 &\leq x_{+,surf} \leq 1, \\ V_{cell} &< 4V. \end{aligned} \quad (2-37)$$

The method used to solve this optimization problem is Dynamic Programming (DP).

### 2-3-3 Result of method 1

The strategy was tested experimentally on a graphite/LiFePO4 energy cells with 400 mAh nominal capacity. More details on the setup and the test conditions can be found in [44]. The strategies implemented were CCCV with charge rates of 1C, 2C, 3C, 4C, 5C, and a fast

charging strategy was used with  $\beta$  and  $\gamma$  in Eq.2-36 being 0 and  $\alpha$  being 1, and a health-conscious fast charging strategy has been used with  $\alpha = 1$  and  $\beta = \gamma = 5$ .

The experimental results can be shown in Fig.2-14. Starting with the cell voltage against time, it can be seen that all strategies cycle the battery between a cell voltage of 2.6 V and 3.6V. Looking also at the charge current against time, it can be seen that the health conscious fast charging strategy undergoes 3 stages. The first stage is when a constant high charge current is applied of around 4.2C for about 45s until the electrolyte concentration at the anode collector is almost reduced to 0. Then, in the second stage, the current is gradually lowered to around 2.4C in order to avoid full lithium depletion in the electrolyte. Lastly, in the third stage, the charge current is gradually lowered further in order to avoid lithium plating to minimize the aging of the battery.

It can be seen in Fig.2-14, that with the fast charging strategy, a charge time of 1158s (about 20 minutes) was achieved whereas the health-conscious fast charging strategy achieved a charging time of 1747s (about 30 minutes). The charging times for the CCCV strategy at the different charging rates can be found in current vs time plot in Fig.2-14, where it can be seen that fast charging and health conscious fast charging strategies achieve a 63.4 % and 45.5 % faster charging time respectively compared to the 1C CCCV charging strategy. The fast charging strategy outperforms all CCCV charging strategies as well as the health conscious fast charging strategy in terms of charging time.

On the other hand, looking at the long term effects each strategy has on the capacity fade, it can be seen that the health conscious fast charging strategy comes out on top. To test the aging of the battery, 7 identical Li-ion cells were cycled 300 times using the 7 different strategies mentioned in Fig.2-15. The discharge strategy used for cycling the cells was the 1C CCCV strategy. It can be seen from Fig.2-15 that using the health conscious fast charging, the capacity fade experienced across the 300 cycles was minimal with the normalized capacity reducing from 100 % to 95 %, showing similar aging performance to 1C CCCV strategy, but at almost twice the charging rate. The fast charging strategy shows significantly poorer performance having the normalized capacity reducing from 100 % to 40 % after 300 cycles, making the battery unusable since a battery becomes at the end of its life when the normalized capacity reduces to around 80%. It can also be noticed that the 3C, 4C and 5C CCCV charging strategies that show relatively good charging time performance (still fast charging is better), have even worse effects on the capacity fade of the battery compared to the fast charging strategy, with the worst performing one being 4C CCCV, having the normalized capacity reduce to 0 % at the 110th cycle. As a result, the best trade-off between charging time and the health of battery is achieved only by the health conscious fast charging strategy.

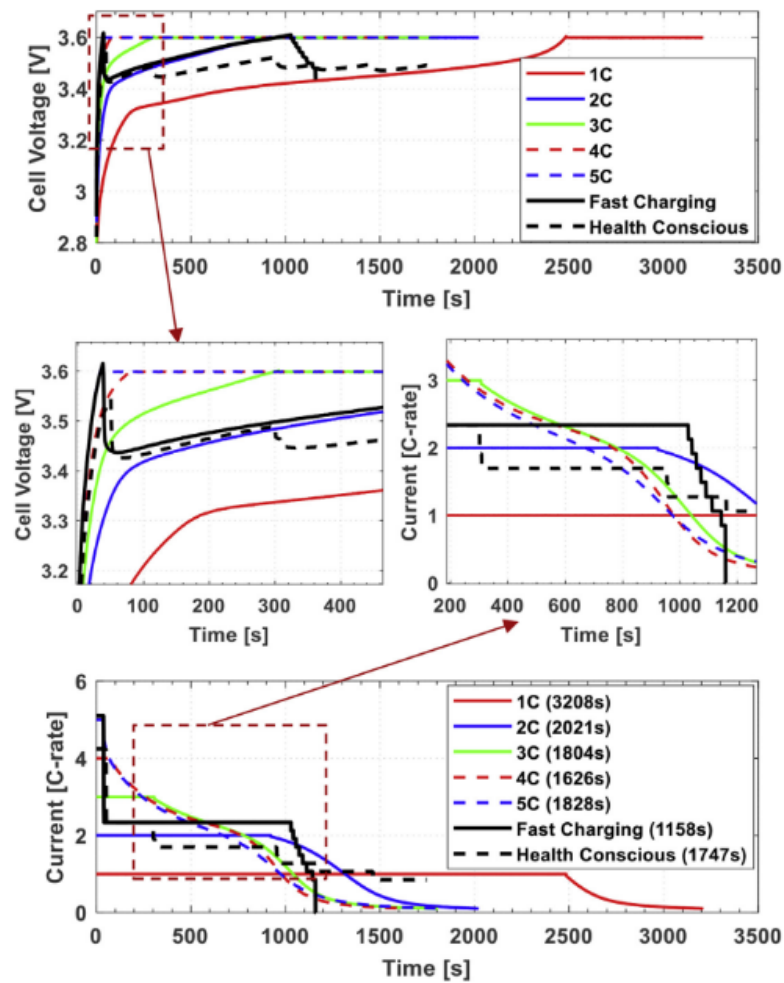


**Figure 2-14:** Experiment results for CCCV strategy at different charging rates, fast charging strategy and health-conscious fast charging for method 1. [44]

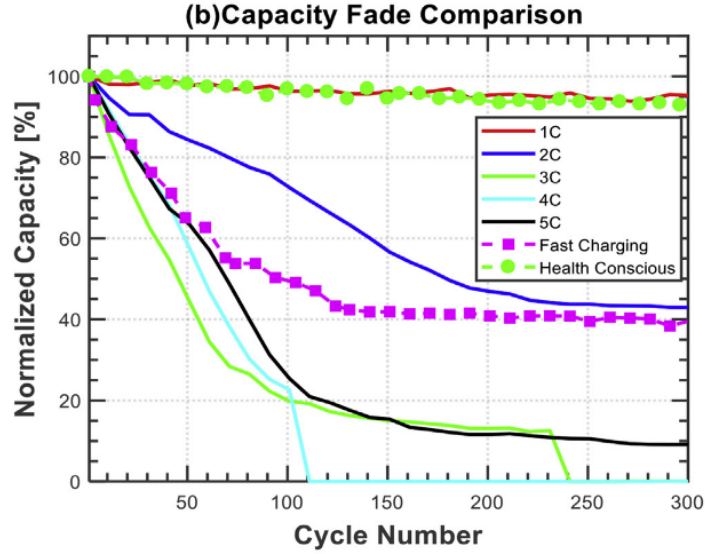


**Figure 2-15:** Capacity fade comparison between CCCV at different charge rates, fast charging and health conscious fast charging strategies for method 1. [44]

### 2-3-4 Method 2 [77]

#### Nonlinear Model Predictive Control (NMPC) Formulation

The second optimization based charging strategy to be discussed uses NMPC as a solver. NMPC is an advanced feedback control law with its main applications being stabilization and reference tracking problems [25]. This also makes it suitable for Battery Management System (BMS) applications to find optimal charging protocols.

The battery model used is based on a Full Order Model (FOM) of the P2D model in section 2-1-1, then it was simplified into a Reduced Order Model (ROM) [41] to reduce the complexity for real time control purposes. The ROM simplifies solid phase concentration of the Li-ion using a biquadratic polynomial approximation, in a similar manner to the 2-term polynomial approximation in the ESPM discussed in section 2-1-3. In addition, it can access internal immeasurable states such as ion concentrations side reaction rate, lithium plating rate and SOC. The accuracy of prediction of SOC is improved by a Sigma-Point Kalman Filter (SPKF) [77] [9]. The degradation mechanisms incorporated in the model is the side reactions which mainly includes SEI growth and the other degradation mechanism included in the model is the lithium plating/stripping rate. The model for such mechanisms used is the main electro-chemical degradation model dynamics discussed in section 2-2 of this chapter.

The optimal control problem used in [77] minimizes the following cost function,

$$J = \min_{I(k)} \sum_{k=1}^{k=N} \left( \alpha \cdot I(k) + \beta \dot{q}_{\text{loss}}^{SR}(k) \right), \quad (2-38)$$

where  $\alpha$  and  $\beta$  are the weighting factors that adjust the trade-off. between fast charging and aging processes.  $I(k)$  is the charging current at time step  $k$ .  $N$  is the control horizon which is generally equal to the prediction horizon which represents the length of the charging process.

$\dot{q}_{\text{loss}}^{SR}$  is the rate of ion loss over the volume of the composite anode, which is calculated using the side reaction, rate as follows

$$\dot{q}_{\text{loss}}^{SR}(k) = \int_{x=0}^{\delta-} \left( |j_{\text{side}}^{Li}(l, k)| \right) Adl. \quad (2-39)$$

The constraints include the model dynamics, input, and states as follows

$$\begin{aligned} I_{\min} &\leq I(k) \leq I_{\max}, \\ SOC(k) &\leq SOC_{\max}, \\ V_{\text{cell}}(k) &\leq V_{\text{cell},\max}, \\ c_{s,\text{surf},-} &\leq c_{s,\max,-}. \end{aligned} \quad (2-40)$$

It can be seen from the charging strategy the minimization of the lithium plating rate was not considered, which does not align with the pre-set objectives being the taking into account both SEI growth as well as lithium plating in the charging strategy. While lithium plating rate can be included in the cost function, Yin and Yul Choe [77] proposed a pulse discharging strategy to promote lithium stripping. In other studies, a 2C pulse discharging current with a frequency of 20mHz was concluded and validated experimentally to be the optimal [4] [66]. However, in the study by Yin and Yul Choe [77], they proposed an optimization based discharging strategy with the aim to completely recover the plated lithium. The optimization variables used were the charging time  $t_c$ , discharging time  $t_d$  and the amplitude of the discharging current  $I_d$ .

### 2-3-5 Results of method 2

In order to analyze the performance of the charging strategy developed, a simulation was performed on a 3.10 GHz desktop computer using a control/prediction horizon of 5 and a sampling time of 1 s. The method of determining such parameters is discussed [77]. The algorithm used to solve the optimization problem is Sequential Quadratic Programming (SQP) due to its robustness and constraint handling properties [49]. With such an algorithm and control/prediction horizon, the maximum and average execution time of the optimization problem were found to be 0.5s and 0.064s respectively, making it a suitable real time control algorithm. After simulation of the model under the real time control algorithm with the different combinations of the weighting factors  $\alpha$  and  $\beta$  as seen in Fig.2-16, the battery parameters such as charging current (A), cell terminal voltage (V), the surface Li-ion concentration (mol/cm<sup>3</sup>) and the reference temperature (°C) against charging time (min) as seen in Fig.2-16 a),b),c),d), respectively. It can be seen that in Fig.2-16 a),b),c) that the imposed constraints (black dashed lines) are not violated and the edge of the constraints are reached for all combinations of the  $\alpha$  and  $\beta$  weighting factors. In Fig.2-16d), it can be seen that the reference temperature stays within the range -1.5 °C and 38.9 °C. It is mentioned in [77] that at high charging currents, a high temperature is required to slow down the lithium plating rate whereas when the charging current is low, a low reference temperature is required to slow down side reaction (SEI formation) rate. While this is the case as seen in Fig.2-16 a) and Fig.2-16 d), this should be further validated as there is no definitive answer in literature on the temperature effects on the lithium plating and SEI growth.

As for the performance of the charging strategy in terms of charging time and the degradation

of the battery, the charging time (min) for each simulation as well as the ion loss (Ah) were plotted against the ratio of the weighting factors  $\beta/\alpha$  as illustrated in Fig.2-16 e) and Fig.2-16 f) respectively. From Fig.2-16e), it can be noticed that as the ratio  $\beta/\alpha$  increases, the time it takes to charge to 40% (pink line), 80% (orange line) and 100% (blue line) increases exponentially, thus a low  $\beta/\alpha$  optimizes charging time, having a lowest charging time of 48 min to reach 100 % at  $\beta/\alpha = 0$  and highest charging time to reach 100% of 95 min at  $\beta/\alpha = 25000$ . On the other hand, in Fig.2-16f) as the ratio  $\beta/\alpha$  increases, the ionic losses decrease, emphasizing the reduction of side reactions with increasing  $\beta$ . The highest degradation occurs when  $\beta = \beta/\alpha = 0$  having ionic losses of 0.0255 Ah whereas the lowest occurs at  $\beta/\alpha = 25000$  with ionic losses being 0.0149 Ah.

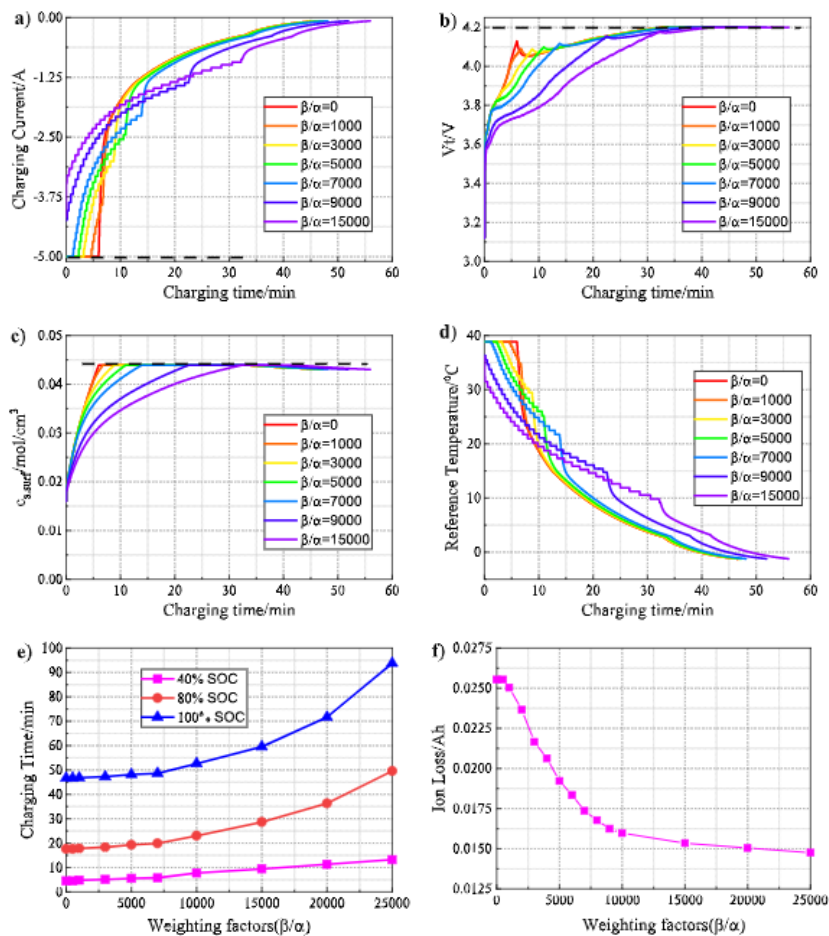


Figure 2-16: Simulation and experiment results for fast charging strategy for method 2. [77]

### 2-3-6 Other methods in literature

There are various other optimization based charging methods discussed in several studies. In this section, some of the most recent charging methods will be discussed.

A recent study developed a new health aware fast charging algorithm is developed from a computationally efficient, linear time varying MPC [83]. The battery model developed is an electro-chemical SPMe augmented with a thermal model. A reduction technique was then

used to simplify the dynamics further, resulting in an ODE that arose from a PDE due to 2 assumptions made for the simplified model. The degradation model used is an electro-chemical model similar to the one in the study by Yang and colleagues [76], however, in this study, side reactions (SEI growth) is considered as the only degradation mechanism. The battery charging algorithm is then formulated as a linear time varying MPC algorithm based on the ROM developed. This method continuously linearizes the nonlinear model around a reference point, in order to reduce computational complexity for real time control purposes. The method was shown to perform 22% better than the standard CCCV in terms of charging speed. The charging strategy is also computationally efficient, with an execution time of 3.3 ms, suitable for real time control applications. The battery degradation is not shown in this study, but the algorithm is shown to satisfy the current and temperature constraints imposed [83], which are known to be the main degradation causes. This method was not chosen since details on the results for the degradation performance were not shown, raising uncertainty with how well the method tackles degradation.

Another study implemented ROM SPMe model was used for the battery model, where the dynamics are transformed from nonlinear PDE to a linearized ODE model, for complexity reduction [78]. The degradation model used is an electro-chemical one, similar to the study by Yang and colleagues [76], with side reactions only considered. Additionally, an Extended Kalman Filter is used, to reduce the dynamic error which is caused from initial average Li-ion concentration and SOC values. The charging strategy used was based on a CCCV charging mechanism, with constraints on the capacity degradation, terminal cell voltage and surface concentrations. The method starts with constant charging current at maximum C-rate, with the constraints monitored continuously. If one of the constraints are violated, the constant charging current is reduced based on predefined change in SOC. This continuously occurs until stopping condition is satisfied. For this method, the health conscious fast charging strategy achieved the slowest charging time compared to fast charging strategies cases that do not consider degradation. The health conscious fast charging strategy charges a 15.7Ah Li-ion battery in 40 min, 27% slower than the fastest charging strategy. However, it achieved significantly lower degradation for the battery, with ionic losses of  $1.85 \times 10^{-3}$  Ah, 40% lower than the fastest charging strategy. This method was not chosen since real time control applicability was not shown, nor any information on the computational times of the methods implemented.

The last study to be discussed is by Lin and colleagues [47], where the battery model is an ESPM using the two term polynomial approximation. The electrolyte diffusion dynamics were simplified using a static map of the electrolyte concentration against a range of charging currents, where a first order transfer function was obtained. A thermal model based on the Arrhenius' correlation [43] was also incorporated to the ESPM. The degradation was not well modelled in this paper, as it was only incorporated as an electrolyte film resistance in the in the ESPM rather than monitoring the behaviour of the physical degradation states such as SEI and lithium plating molar fluxes. The charging strategy used is an optimization based charging strategy that minimizes the charging time, charging losses, as well as the temperature rise, having penalty factors  $\alpha$ ,  $\beta$  and  $\gamma$  to tradeoff between the optimization variables. The results were shown experimentally, proving the algorithm feasibility in real world applications. The trade-off between the 3 optimization variables, depending on the weighting factor choices were shown in detail. This method was not fully used as the electro-chemical degradation model is not incorporated, thus not showing how the main aging mechanisms change with time.

## 2-4 Literature Discussion

In this literature review, the following topics are covered: a general introduction Electric Vehicles (EVs), which includes the background on EVs and the current problems in the road transport sector in terms greenhouse gas emissions, some advantages and disadvantages that the adoption of EVs bring, a comparison of the different types of batteries used in EVs, where it was that the Li-ion battery will be studied in this report due to its high overall performance, then a brief introduction on the different types of Li-ion battery models, degradation models used in literature, where it was concluded that electro-chemical models will be the main focus due to their high accuracy, ability to access immeasurable states and flexibility in tuning various battery parameters in the model. Lastly, an introduction on the different types of health conscious charging strategies for Li-ion batteries in EVs, where optimization based charging strategies will be used, as they are the most recently developed in literature, they support the electro-chemical battery/degradation models, they do not require previous input/output data and constraints can be easily incorporated in the optimization problem.

In the second section, an in depth analysis on 3 types of electro-chemical models were discussed, the P2D model, the SPM and the ESPM. Due to the relatively high accuracy under a wide range of charge/discharge current densities as well as the low computational complexity, allowing for real time control to be applicable, a version of the ESPM will be the chosen model for the thesis. More specifically, the ROM by Yin and colleagues [78] will be the model of choice, as the diffusion dynamics are represented as ODE, simplifying the complexity of the model significantly. The third section discusses the different types of electro-chemical degradation models used in research where it was concluded that the dominating degradation mechanisms are the SEI growth rate and the lithium plating rate, thus an electro-chemical degradation model capturing both mechanisms will be considered in this report, also, since they are applicable to all the models mentioned. It presented high accuracy in almost all cases except at the end of the battery cycle life at high (3C) discharge currents. More specifically, the degradation models presented by Lin and colleagues [44], as well as Yang and colleagues [76], as they are considered the most complete, showing the 2 main degradation mechanisms as well as having high accuracy.

Lastly, 2 different optimization based health conscious fast charging strategies were discussed, analyzed and compared with each other. Then, a brief overview on some of the other charging strategies available in research were discussed. Since the optimization strategies presented in this literature review each have a unique element them, it was concluded that a combination of multiple studies were used. First of all, the cost function from method 1 [44] was chosen as it showcases both objectives required, being minimizing the charging time as well as degradation. On top of that, the degradation mechanisms, being the SEI growth and the lithium plating are shown separately in the cost function, adding an extra element of detail for analysis of the 2 mechanisms. Moreover, the NMPC formulation in the study by Yin and colleagues [77] was chosen for such a cost function and constraints due to the ease of implementation of the method/constraints and fast computational time.



# Mathematical Modelling and Implementation

## 3-1 Introduction

As concluded in the literature, a Reduced Order Model (ROM) based on the Electrolyte Enhanced Single Particle Model (SPMe) using a polynomial profile approximation for the solid phase diffusion dynamics was chosen for implementation [69], whereas a transfer function model with the equilibrium electrolyte concentration as input and the instantaneous electrolyte concentration as output for each electrode was chosen to obtain the surface electrolyte concentration dynamics [44]. As for the degradation dynamics, the full order electro-chemical model shown in [76] coupled with the battery dynamics. The next section will show the full battery and degradation model equations in detail. The symbol definitions, units and parameter values for the model equations presented in this chapter can be found in Table A-1 and Table A-2.

## 3-2 Battery Model Dynamics

### 3-2-1 Extended Single Particle Model (ESPM)

The ESPM is an extension to the SPMe model in which the solid phase diffusion dynamics in Eq.2-14 are approximated by making the assumption that the solid li-ion concentration has a polynomial profile shape as well as using volume averaging techniques to obtain volume averaged concentrations and fluxes. Furthermore, as part of the ESPM and some cases for the SPMe the molar flux in Eq.2-4 is approximated such that it is linearly dependent on the charge/discharge current. The approximated molar flux was used for the ESPM whereas the molar flux governed by the Butler Volmer equation in Eq.2-4 was used for the SPMe. As for the electrolyte dynamics, they could remain the same as Eq.2-20, but for the charging

strategy, avoiding electrolyte depletion is only needed from the strategy. Since the electrolyte concentrations on one of the anode or cathode surfaces depletes before electrolyte at any  $x$  position in the cell for charging or discharging respectively, the electrolyte behaviour on the electrode surfaces capture the information needed for implementing the control strategy. The degradation dynamics also require electrolyte information, however, since degradation mechanisms of interest occur on the surface of the anode, only electrode surface electrolyte information is needed. This leaves an opportunity to further approximate the electrolyte dynamics by obtaining a linear transfer function model that captures the electrolyte concentration evolution on the electrode surfaces. A version of this was implemented for the ESPM. Due to the fact that only electrode surface variables are considered, the  $x$  spatial dependency is also removed, simplifying the dynamics further, compared to the nonlinear, spatially dependent dynamics in Eq.2-20.

### Solid Phase Diffusion Dynamics [69]

The solid phase dynamics for the ESPM model portrays the evolution of two main state variables, the volume averaged solid phase concentration,  $\bar{c}_{s,j}(t)$ , and the volume averaged solid phase concentration flux  $\bar{q}_j(t)$  and one output variable being the solid phase surface concentration  $c_{s,\text{surf},j}(t)$ . The reason for addressing these variables in specific is that, the  $c_{s,j}$  for computing the State Of Charge (SOC) and  $c_{s,\text{surf},j}$  is used to compute the open circuit voltage  $U_{ocv}$ . The state evolution of  $\bar{c}_{s,j}(t)$  given as follows,

$$\frac{d}{dt}\bar{c}_{s,j}(t) + 3\frac{j_j}{R_p} = 0 \quad (3-1)$$

where  $j_j$  is the molar flux as in Eq.2-4, however, since only surface variables are relevant for the ESPM, the spatial dependency can be removed, and the molar flux on the electrode surfaces can be written as follows,

$$j_{j,\text{approx}} = \frac{j \cdot I}{F \cdot a_j \cdot L_j}. \quad (3-2)$$

The state evolution of the volume-averaged flux  $\bar{q}_j(t)$  is given as,

$$\frac{d}{dt}\bar{q}_{s,j}(t) + 30\frac{D_{s,j}}{R_p^2}\bar{q}_{s,j}(t) + \frac{45}{2}\frac{j_j}{R_p^2} \quad (3-3)$$

The output equation for the surface concentration is given as,

$$35\frac{D_{s,j}}{R_p}[c_{s,\text{surf},j} - \bar{c}_{s,j}(t)] - 8D_{s,j}\bar{q}_{s,j}(t) = -j_j \quad (3-4)$$

The full derivation for the equations above can be found in [69].

### Electrolyte Phase Diffusion Dynamics [44]

To simplify the electrolyte diffusion dynamics shown in Eq.2-20, a linear relationship can be generated from the full order Pseudo 2-Dimensional (P2D) model which predicts the Li-ion

concentration at the surface of the anode collector with respect to the charge rate (explained further in section 3-3). From there, a first order transfer function was obtained given by,

$$G(s) = \frac{c_{e,\text{surf},j}(s)}{c_{e,\text{surf}_{\text{eq}},j}(s)} = \frac{1}{\Delta T_j s + 1}, \quad (3-5)$$

where  $c_{e,\text{surf},j}(s)$  is the instantaneous electrolyte concentration (in Laplace domain) near current collector of electrode  $j$ .  $c_{e,\text{surf}_{\text{eq}},j}(s)$  is the equilibrium electrolyte concentration at a given charge rate near current collector of electrode  $j$ .  $\Delta T_j$  is the time constant for the diffusion dynamics. It can also be noticed that only electrode current collector surface variables were considered. The reasoning behind this is that in the charging strategy, a constraint only needs to be imposed on surface electrolyte concentrations, to avoid battery damage, making the electrolyte concentration across the rest of space  $x$  irrelevant. It can be seen that the electrolyte dynamics simplified from a nonlinear PDE in Eq.2-20, to a linear PDE.

### Voltages and Potentials

The cell output voltage is then defined as the solid phase potential difference,

$$V_{\text{cell}} = \phi_{s,+}(x = L) - \phi_{s,-}(x = 0) - R_{\text{cell}} \cdot I(t), \quad (3-6)$$

where  $\Phi_{s,+}$  and  $\Phi_{s,-}$  are the positive and negative electrode potentials respectively, given by,

$$\Phi_{s,\pm}(t) = \frac{2RT}{F} \operatorname{asinh} \left( \frac{\mp I(t)}{2a_{\pm}L_{\pm}r_{\text{eff}} \sqrt{c_s^0 c_{s,\text{surf}\pm}(t) (c_{s,\text{max}\pm}(t) - c_{s,\text{surf}\pm}(t))}} \right) + U_{\pm}(c_{s,\text{surf}\pm}(t)) + \frac{R_f \pm I(t)}{a_{\pm}L_{\pm}} \quad (3-7)$$

where  $U_{\pm}(c_{s,\text{surf},\pm}(t))$  is open circuit potential per electrode for the LGM50 5 Ah battery cell, given by [18],

$$\begin{aligned} U_+(c_{s,\text{surf},+}) &= -0.8090 \cdot \frac{c_{s,\text{surf},+}}{c_{s,\text{max},+}} + 4.4875 - 0.0428 \\ &\times \tanh \left( 18.5138 \left( \frac{c_{s,\text{surf},+}}{c_{s,\text{max},+}} - 0.5542 \right) \right) - 17.7326 \\ &\times \tanh \left( 15.7890 \left( \frac{c_{s,\text{surf},+}}{c_{s,\text{max},+}} - 0.3117 \right) \right) + 17.5842 \\ &\times \tanh \left( 15.9308 \left( \frac{c_{s,\text{surf},+}}{c_{s,\text{max},+}} - 0.3120 \right) \right), \\ U_-(c_{s,\text{surf},-}) &= 1.9793 \cdot e^{-39.3631 \frac{c_{s,\text{surf},-}}{c_{s,\text{max},-}}} + 0.2482 - 0.0909 \\ &\times \tanh \left( 29.8538 \left( \frac{c_{s,\text{surf},-}}{c_{s,\text{max},-}} - 0.1234 \right) \right) - 0.04478 \\ &\times \tanh \left( 14.9159 \left( \frac{c_{s,\text{surf},-}}{c_{s,\text{max},-}} - 0.2769 \right) \right) - 0.0205 \\ &\times \tanh \left( 30.4444 \left( \frac{c_{s,\text{surf},-}}{c_{s,\text{max},-}} - 0.6103 \right) \right). \end{aligned} \quad (3-8)$$

The SOC is given by the following equation,

$$SOC = \frac{\bar{c}_{s,-}}{c_{s,\max,-}}. \quad (3-9)$$

As for the electrolyte potential at the electrode surfaces,  $\Phi_{e,\text{surf},\pm}$ , it is given by [40],

$$\Phi_{e,\text{surf},\pm} = \left( \Phi_{0,e,\text{surf},\pm} + (1 - t_+) \frac{2 \cdot R \cdot T}{F} \right) \log \left( \frac{c_{e,\text{surf},+}}{c_{e,\text{surf},-}} \right), \quad (3-10)$$

where  $\Phi_{0,e,\text{surf},\pm}$  is the initial electrolyte potential at the surface of the positive/negative electrode. Finally, the terminal voltage, also known as the open circuit voltage is defined as,

$$U_{\text{ocv}} = U_+(c_{s,\text{surf},+}) - U_-(c_{s,\text{surf},-}). \quad (3-11)$$

### 3-3 Degradation Model Dynamics

The main influence that the electro-chemical degradation model by Yang and colleagues [76] has is the influence of the Solid Electrolyte Interphase (SEI) and lithium plating growth on the total molar flux. Without incorporation of degradation mechanisms, the total molar flux was only considered to be the intercalation molar flux such as in Eq.2-4 or Eq.3-2. With the degradation model included, the total pore wall flux,  $j_{\text{tot}}$ , is now defined as the sum of the intercalation flux, SEI flux and lithium plating flux,

$$j_{\text{tot}} = j_{\text{int}} + j_{\text{SEI}} + j_{\text{pl}}, \quad (3-12)$$

where  $j_{\text{sei}}$  is the SEI molar flux,  $j_{\text{pl}}$  is the lithium plating molar flux and  $j_{\text{int}}$  is the intercalation molar flux, which is governed by Eq.3-2 for the ESPM, with the intercalation overpotential having an additional term dependent on the film resistance  $R_{\text{film}}$  to incorporate degradation compared to the overpotential below Eq.2-4,

$$\eta_{\text{int}} = \phi_{s,-} - \phi_{e,-} - \frac{j_{\text{tot}}}{a} R_{\text{film}} - U_{\text{int},-}. \quad (3-13)$$

where  $U_{\text{int}} = U_-(SOC_-)$  as in Eq.3-8 is the equilibrium potential for lithium intercalation reaction, and  $R_{\text{film}}$  is the resistance of the surface film. Note that only anode molar wall fluxes are considered for the degradation since SEI and lithium plating are only formed on the anode.

#### 3-3-1 SEI Growth

For the SEI growth dynamics, it is mainly affected by activity on the film surface, such as surface kinetics and diffusion rate of Ethyl Carbonate (EC) at the film surface [62]. As a result, the dynamics of the SEI formation is governed by the tafel kinetics at the cathode [57] seen below,

$$j_{\text{SEI}} = -aFk_{0,\text{SEI}}c_{\text{EC}}^{\text{S}} \exp \left( -\frac{\alpha_{c,\text{SEI}}F}{RT} \left( \phi_{s,-}(x=0) - \phi_{e,\text{surf},-} - \frac{j_{\text{tot}}}{a} R_{\text{film}} - U_{\text{SEI}} \right) \right), \quad (3-14)$$

where  $k_{0,SEI}$  is the kinetic rate constant,  $\alpha_{c,SEI}$  is the charge transfer coefficient with regards to SEI,  $U_{SEI}$  is the equilibrium potential of SEI formation reaction, and  $c_{EC}^S$  is the concentration of EC on the surface of graphite, which is calculated based on the mass conservation of EC,

$$-D_{EC} \frac{c_{EC}^S - c_{EC}^0}{\delta_{film}} = \frac{j_{SEI}}{F}. \quad (3-15)$$

where  $D_{EC}$  is the diffusivity of EC,  $c_{EC}^0$  is the concentration of EC in the bulk electrolyte, and  $\delta_{film}$  is the thickness of the surface film.

### 3-3-2 Lithium Plating

With regards to Lithium plating, it is assumed to be irreversible in this model [76], meaning that the removal of plated lithium in the discharge process is considered to be insignificant. As a result, the pore wall flux with respect to Lithium plating,  $j_{lpl}$ , can be expressed by the cathodic tafel equation below,

$$j_{lpl} = -ai_{0,lpl} \exp\left(-\frac{\alpha_{c,lpl}F}{RT} \left(\phi_{s,-}(x=0) - \phi_{e,surf,-} - \frac{j_{tot}}{a} R_{film}\right)\right), \quad (3-16)$$

where  $i_{0,lpl}$  is the exchange current density of Li deposition and  $\alpha_{c,lpl}$  is the charge transfer coefficient with regards to lithium plating.

### 3-3-3 Diffusion Equations

The diffusion equations with regards to SEI growth and Lithium plating can be expressed as,

$$\begin{aligned} \frac{\partial c_{SEI}}{\partial t} &= -\frac{j_{SEI}}{2F} - \frac{j_{lpl}}{2F} \beta, \\ \frac{\partial c_{Li}}{\partial t} &= -\frac{j_{lpl}}{F} (1 - \beta), \end{aligned} \quad (3-17)$$

where  $c_{SEI}$  and  $c_{Li}$  are the molar concentrations of SEI and lithium metal per unit volume of the electrode. The parameter  $\beta$  represents the fraction of the Lithium plating that is converted to SEI. Since the graphite surface film constitutes of the both the SEI and the Lithium plating material, the thickness of the film  $\delta_{film}$  will include the volume of the SEI and Lithium metal together as seen in the equation below,

$$\delta_{film} = \frac{1}{a} \left( \frac{c_{SEI} \cdot M_{SEI}}{\rho_{SEI}} + \frac{c_{Li} \cdot M_{Li}}{\rho_{Li}} \right), \quad (3-18)$$

where  $M$  and  $\rho$  are molar weight and density respectively. The left term in the bracket is the specific volume of SEI, and the right term is the specific volume of lithium metal. Since the removal of Lithium material is not taken into account in this model, the Lithium material would be isolated from the electron conduction matrix. As a consequence, the film resistance is directly affected by the SEI only as given below, As stripping of lithium metal is neglected in this model (i.e. all lithium is lost once plated), the plated lithium is considered to be

isolated from the main electrode matrix. Hence, resistance of surface film is determined by SEI only, i.e.

$$R_{\text{film}} = \delta_{\text{film}} \cdot r_{\text{SEI}}, \quad (3-19)$$

where  $r_{\text{SEI}}$  is the SEI resistivity. As mentioned above, one feature of the present model is that lowering of anode porosity due to surface film growth is considered, which is implemented through relating the change of anode porosity with the increase of surface film thickness via the following expression:

$$\frac{d\varepsilon}{dt} = -a \frac{d\delta_{\text{film}}}{dt}. \quad (3-20)$$

### 3-4 Model Implementation and Simulation

This section explains how the Li-ion battery models in section 2-1-1, 2-1-2, 3-1-1 and 3-2 have been implemented and/or simulated. The charging experiment conditions, parameter values and software used per model are also stated.

#### 3-4-1 P2D Model and SPMe

Since the P2D model is known to be most accurate for a wide range of currents, it will be used as a base for comparison to the SPMe and ESPM models. The full P2D model and SPMe has been simulated as per Eq.2-1 to Eq.2-13 and Eq.2-14 to Eq.2-20 using the Python library PyBamm according to the parameter values in table A-2.

#### Modelling Experiment Conditions

Since the battery is initially charged, a discharging experiment at current  $C/10$  was performed to fully deplete the battery to reach the terminal voltage  $V_{\text{cell,min}}$ , then the experiments in Fig.3-1, Fig.3-2, Fig.3-3 and Fig.3-4 have been performed for the solid and electrolyte phase dynamics. The reasoning behind the constant charging experiments is to test the model under a constant current over a prolonged period of time and to check what is the maximum current range capability for the SPMe and ESPM models. The differing current experiment in Fig.3-3 and Fig.3-4 is to check if the SPMe and ESPM remain accurate under large changes in current in the charging process.

```
pybamm.Experiment(["Charge at 1C for 1 hour"],period = '1 second')
```

**Figure 3-1:** Charging Experiment 1.

```
charge_exp_OKane2C_SPMe= pybamm.Experiment(["Charge at 2C for 1 hour"],period = '1 second')
```

**Figure 3-2:** Charging experiment 2.

```
pybamm.Experiment([("Charge at 0.5C for 75 seconds",
                    "Charge at 1C for 75 seconds",
                    "Charge at 1.5C for 75 seconds",
                    "Charge at 2C for 75 seconds"),period = '1 second')
```

Figure 3-3: Charging Experiment 3.

```
pybamm.Experiment([("Charge at 0.25C for 37.5 seconds",
                    "Charge at 0.5C for 37.5 seconds",
                    "Charge at 0.75C for 37.5 seconds",
                    "Charge at 1C for 37.5 seconds",
                    "Charge at 1.25C for 37.5 seconds",
                    "Charge at 1.5C for 37.5 seconds",
                    "Charge at 1.75C for 37.5 seconds",
                    "Charge at 2C for 37.5 seconds"),period = '1 second')
```

Figure 3-4: Charging Experiment 4.

### 3-4-2 ESPM

Since the ESPM shown in Section 3-2-3 is unavailable in any software, it was implemented and simulated on MATLAB. The simulation data for the P2D and SPMe was obtained from Python and the model comparison was performed on MATLAB.

#### Solid Phase Diffusion Model

The ESPM solid phase diffusion model from Eq.3-1 to Eq.3-4 was implemented as a linear state space model with the following state matrices,

$$\begin{aligned}
 A &= \begin{bmatrix} -30 \cdot \frac{D_{s,+}}{R_{p,+}^2} & 0 & 0 & 0 \\ -30 \cdot \frac{D_{s,-}}{R_{p,-}^2} & 0 & 0 & 0 \\ 0 & 0 & 0 & 0 \\ 0 & 0 & 0 & 0 \end{bmatrix}, & B &= \begin{bmatrix} \frac{45}{2R_{p,+} \cdot F \cdot a_+ \cdot L_+} \\ \frac{45}{2R_{p,-} \cdot F \cdot a_- \cdot L_-} \\ 0 \\ 0 \end{bmatrix}, \\
 C &= \begin{bmatrix} \frac{8R_{p,+}}{35} & 0 & 1 & 0 \\ 0 & \frac{8R_{p,-}}{35} & 0 & 1 \end{bmatrix}, & D &= \begin{bmatrix} \frac{R_{p,+}}{35D_{s,+} \cdot F \cdot a_+ \cdot L_+} \\ \frac{R_{p,-}}{35D_{s,-} \cdot F \cdot a_- \cdot L_-} \end{bmatrix}.
 \end{aligned} \tag{3-21}$$

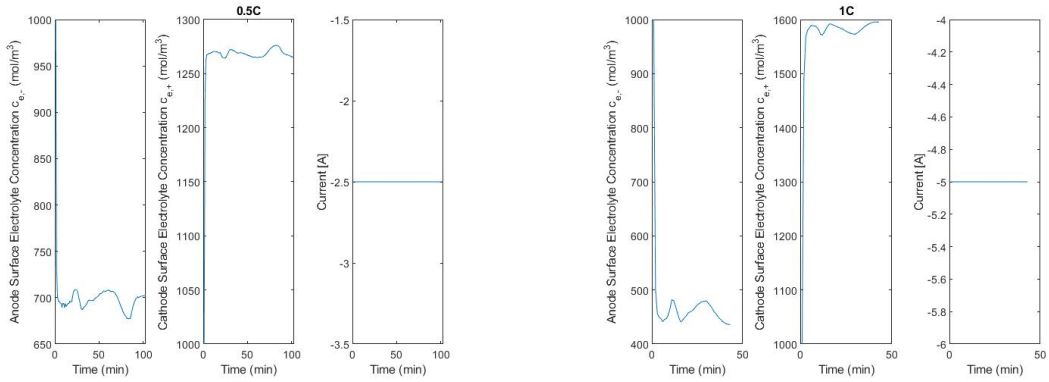
The solid phase states  $x_s$  and outputs  $y_s$  are as follows,

$$x_s = \begin{bmatrix} q_+ \\ q_- \\ \bar{c}_{s,+} \\ \bar{c}_{s,-} \end{bmatrix} \quad y_s = \begin{bmatrix} c_{s,\text{surf},+} \\ c_{s,\text{surf},-} \end{bmatrix} \tag{3-22}$$

#### Electrolyte Phase Diffusion Model

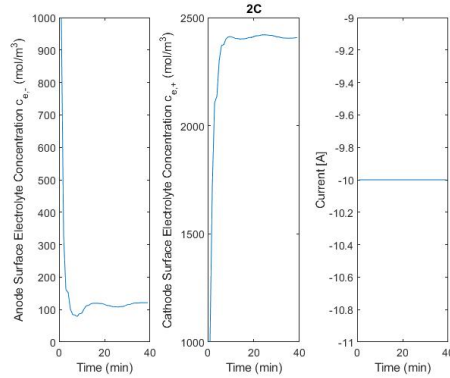
The electrolyte phase diffusion model in Eq.3-5 was implemented by first obtaining a relation between the charge current with the equilibrium electrolyte concentration at the surface of the

electrodes  $c_{e_{eq,j}}$ . Using from the full order P2D PyBamm model, 36 constant current charging experiments from a range 0C-2C were performed to obtain the equilibrium electrolyte concentration per current on the surface of each electrode. 3 examples of the results from the constant charging experiments can be found in Fig.3-5. The equilibrium electrolyte concentrations were obtained by taking the last data point for each charging case. For example, under 0.5C constant charging in Fig.3-5 (a), the equilibrium cathode and anode electrolyte concentrations would be  $1264 \frac{\text{mol}}{\text{m}^3}$  and  $701 \frac{\text{mol}}{\text{m}^3}$  respectively. Under 1C constant charging in Fig.3-5 (b), the equilibrium cathode and anode electrolyte concentrations would be  $1594 \frac{\text{mol}}{\text{m}^3}$  and  $440 \frac{\text{mol}}{\text{m}^3}$  respectively. Under 2C constant charging in Fig.3-5 (c), the equilibrium cathode and anode electrolyte concentrations would be  $2400 \frac{\text{mol}}{\text{m}^3}$  and  $110 \frac{\text{mol}}{\text{m}^3}$  respectively.



(a)  $c_{e,\text{surf},-}$  and  $c_{e,\text{surf},+}$  and the corresponding current profile the 0.5C constant charging experiment.  
Equilibrium  $c_{e,\text{surf},-}$  is  $701 \frac{\text{mol}}{\text{m}^3}$   
Equilibrium  $c_{e,\text{surf},+}$  is  $1264 \frac{\text{mol}}{\text{m}^3}$

(b)  $c_{e,\text{surf},-}$  and  $c_{e,\text{surf},+}$  and the corresponding current profile the 1C constant charging experiment.  
Equilibrium  $c_{e,\text{surf},-}$  is  $440 \frac{\text{mol}}{\text{m}^3}$   
Equilibrium  $c_{e,\text{surf},+}$  is  $1594 \frac{\text{mol}}{\text{m}^3}$



(c)  $c_{e,\text{surf},-}$  and  $c_{e,\text{surf},+}$  and the corresponding current profile the 2C constant charging experiment.  
Equilibrium  $c_{e,\text{surf},-}$  is  $110 \frac{\text{mol}}{\text{m}^3}$   
Equilibrium  $c_{e,\text{surf},+}$  is  $2400 \frac{\text{mol}}{\text{m}^3}$

**Figure 3-5:** Cathode and Anode Surface Electrolyte Concentrations  $c_{e,\text{surf},+}$  and  $c_{e,\text{surf},-}$  under constant charging experiment conditions

From the 36 cathode and anode equilibrium points and its corresponding charging C-rate, the fitting function was obtained as shown in Fig.3-6 and Fig.3-7 where the equilibrium concentrations and its respective C-rate can be found.

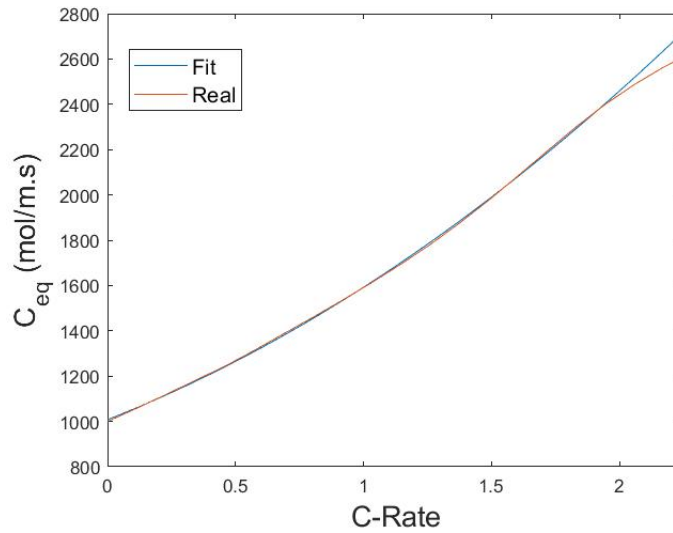


**Figure 3-6:** Plot of P2D model data of the equilibrium electrolyte concentration per current on the cathode current collector surfaces and its corresponding fitting function

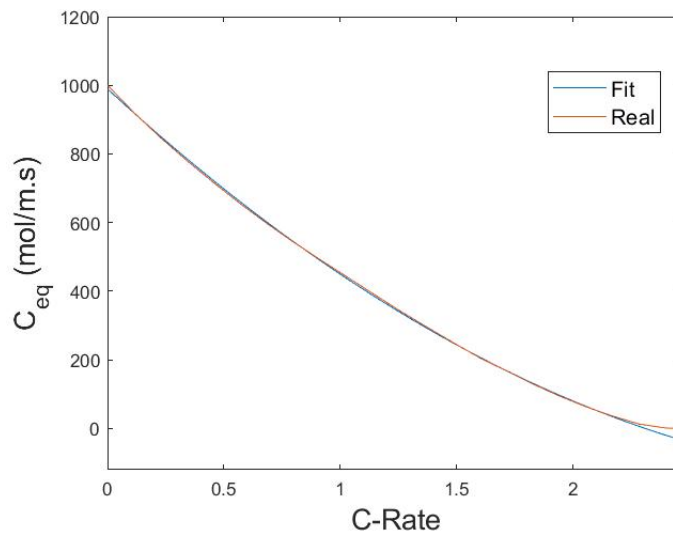


**Figure 3-7:** Plot of P2D model data of the equilibrium electrolyte concentration per current on the anode current collector surfaces and its corresponding fitting function.

It can be noticed that there is a parabolic relation between  $c_{\text{eq},j}$  and  $I$ , having the following functions per electrode,

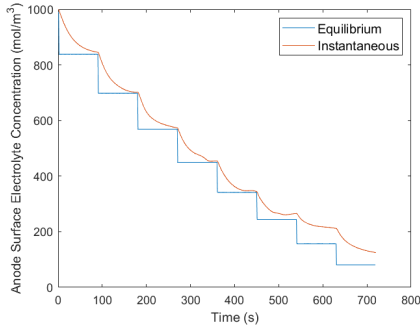
$$\begin{aligned} c_{\text{eq,surf,+}} &= 5.65361 \cdot I^2 - 88.5289 \cdot I + 1008.36, \\ c_{\text{eq,surf,-}} &= 3.40358 \cdot I^2 + 124.921 \cdot I + 989.228, \end{aligned} \quad (3-23)$$

which means the input of the transfer function in Eq.3-5 is indirectly the charging current.

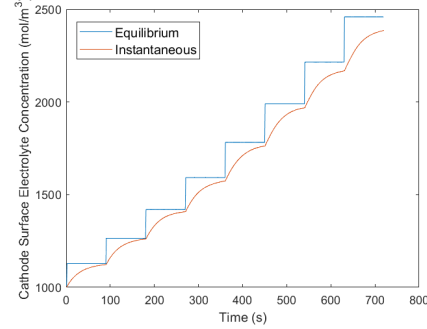
$$\begin{aligned} c_{e_{eq,surf,+}} &= 0.05 \cdot I^2 - 90.1 \cdot I + 998.1, \\ c_{e_{eq,surf,-}} &= 3.40358 \cdot I^2 + 124.921 \cdot I + 989.228, \end{aligned} \quad (3-24)$$

### Obtaining Electrolyte Concentration Transfer Function $G(s)$

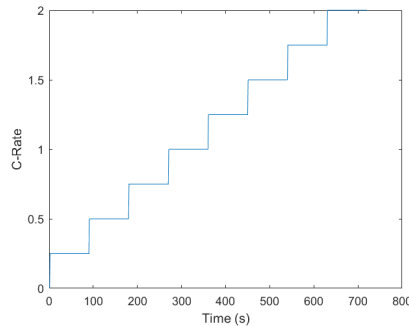
Using the information above, the surface equilibrium electrolyte concentration  $c_{e,surf_{eq,-}}$   $c_{e,surf,j}$  and the corresponding surface instantaneous electrolyte concentration  $c_{e,surf,j}$  at the anode and cathode were plotted as seen in Fig.3-8 (a) and Fig.3-8 (b) respectively, for a varying current profile with the range 0C-2C found in Fig.3-8 (c). The following data input output data was then used to obtain a transfer function using the MATLAB function "tfest". After the transfer function was tested, some manual tuning of the parameter  $\Delta T_j$  was done having the value per electrode as in Table A-2, to further improve the accuracy of the model.



**(a)** Plot of the Anode Surface Equilibrium Electrolyte Concentration  $c_{e,surf_{eq,-}}$  ( $\frac{\text{mol}}{\text{m}^3}$ ) and the corresponding Anode Surface Instantaneous Electrolyte Concentration  $c_{e,surf,j}$  ( $\frac{\text{mol}}{\text{m}^3}$ ) against time  $t$  (s).



**(b)** Plot of the Cathode Surface Equilibrium Electrolyte Concentration  $c_{e,surf_{eq,-}}$  ( $\frac{\text{mol}}{\text{m}^3}$ ) and the corresponding Cathode Surface Instantaneous Electrolyte Concentration  $c_{e,surf,j}$  ( $\frac{\text{mol}}{\text{m}^3}$ ) against time.



**(c)** Corresponding charging C-rate profile vs time  $t$  (s)

**Figure 3-8**

### 3-4-3 Degradation Model

The degradation model dynamics from Eq.3-12 to Eq.3-20 was implemented on MATLAB using the variables in the solid and electrolyte phase diffusion dynamics for the ESPM and the degradation parameter values found in Table A-2. The method at which the model was implemented on MATLAB will be discussed in the next section.

#### System Dynamics

Since the degradation model has nonlinear dependencies in the molar flux equations, it could not be implemented as a state space model. In addition, linearization would also not be straightforward, due to the highly complex jacobian calculations as well as variables changing at a fast rate. As a result, the nonlinear model was kept unchanged and discretized for MATLAB simulation.

Starting with the SEI molar flux evolution, Eq.3-12 and Eq.3-15 were combined with Eq.3-14, leading to the following,

$$j_{\text{SEI}}(k+1) = -aFk_{0,\text{SEI}} \left( \frac{-j_{\text{SEI}}(k) \cdot \delta_{\text{film}}(k)}{F \cdot D_{\text{EC}}} + c_{\text{EC}}^0 \exp \left( -\frac{\alpha_{c,\text{SEI}} F}{RT} \left( \phi_{\text{s},-}(x=0)(k) - \phi_{\text{e,surf},-}(k) - \frac{j_{\text{int}}(k) + j_{\text{sei}}(k) + j_{\text{lpl}}(k)}{a} R_{\text{film}}(k) - U_{\text{SEI}} \right) \right) \right). \quad (3-25)$$

The index  $k$  was introduced to simplify the circular dependency of  $j_{\text{sei}}$  due to the  $j_{\text{sei}}$  appearing in Eq.3-12 and Eq.3-15. The same occurs for the lithium plating molar flux, Eq.3-12 was combined with Eq.3-16 giving the following,

$$j_{\text{lpl}}(k+1) = -ai_{0,\text{lpl}} \exp \left( -\frac{\alpha_{c,\text{lpl}} F}{RT} \left( \phi_{\text{s},-}(k) - \phi_{\text{e},-}(k) - \frac{j_{\text{int}}(k) + j_{\text{SEI}}(k) + j_{\text{lpl}}(k)}{a} R_{\text{film}}(k) \right) \right). \quad (3-26)$$

As for the diffusion equations in Eq.3-17, it can be seen that they are partial differential equations, however, since all the variables within this equation are evaluated on the surface, the spatial dependency is removed, changing the Partial Differential Equation (PDE) to an Ordinary Differential Equation (ODE). The ODE is then approximated using the forward difference numerical method as follows,

$$f'(t) \approx \frac{f(t_{i+1}) - f(t_i)}{T_s}, \quad (3-27)$$

where  $T_s$  is the sampling time. This is done in order to reduce computational time per iteration in MATLAB, rather than computing many derivatives/integrals per iteration in the ODE. This brings the diffusion equations to be as follows,

$$\begin{aligned} c_{\text{SEI}}(k+1) &= c_{\text{SEI}}(k) + T_s \cdot \left( -\frac{j_{\text{SEI}}(k)}{2F} - \frac{j_{\text{lpl}}(k)}{2F} \beta \right), \\ c_{\text{lpl}}(k+1) &= c_{\text{lpl}}(k) + T_s \cdot \left( -\frac{j_{\text{lpl}}(k)}{F} (1 - \beta) \right). \end{aligned} \quad (3-28)$$

Lastly, the film thickness  $\delta_{\text{film}}$  and film resistance  $R_{\text{film}}$  are considered to be the outputs of the degradation and are computed after simulation of the dynamics as follows,

$$\delta_{\text{film}}(k) = \frac{1}{a} \left( \frac{c_{\text{SEI}}(k) \cdot M_{\text{SEI}}}{\rho_{\text{SEI}}} + \frac{c_{\text{Li}}(k) \cdot M_{\text{Li}}}{\rho_{\text{Li}}} \right), \quad (3-29)$$

$$R_{\text{film}}(k) = \delta_{\text{film}}(k) \cdot r_{\text{SEI}}, \quad (3-30)$$

### Battery Simulation Initialization

To emulate the real life experiment as much as possible, the degradation model is cycled for both charging and discharging cases. The battery is first initialized to be in the fully discharged case with the parameter in Table A-2, then after the battery is fully charged, it is initialized with the variables at the final time step for the battery to be discharged. As a result, the initial states for system varies every discharge cycle.

### Capacity Fade Calculation

The battery capacity fade per charge/discharge cycle is computed as follows [52],

$$Q_{\text{loss}} = \int_{t=0}^{t=T_{\text{charge}}} J_{\text{loss}}(t) S_- dt, \quad (3-31)$$

where  $J_{\text{loss}}$  are the molar flux losses due to SEI and lithium plating given by,

$$J_{\text{loss}}(t) = J_{\text{SEI}}(t) + J_{\text{pl}}(t). \quad (3-32)$$

To reduce computational complexity, the following rectangular numerical approximation was used,

$$\int_a^b f(t) dt \approx \Delta t [f(t(a+1)) + f(t(a+2)) + \dots + f(t(b))], \quad (3-33)$$

leading to the following,

$$Q_{\text{loss}} = \sum_{k=1}^{k=\frac{T_{\text{charge}}}{T_s}} J_{\text{loss}}(k) S_- T_s, \quad (3-34)$$

where  $S_j$  is the superficial surface area given by,

$$S_j = a_j V_j. \quad (3-35)$$

This means the capacity of the battery is updated per cycle as such,

$$Q_{\text{new}} = Q_{\text{nom}} - \sum_{\text{cycle}=1}^{\text{cycle}=\text{cycle}_{\text{curr}}} Q_{\text{loss}}(\text{cycle}), \quad (3-36)$$

where  $Q_{\text{new}}$  is the new capacity,  $Q_{\text{nom}}$  is the nominal capacity,  $\text{cycle}$  is the cycle number and  $\text{cycle}_{\text{curr}}$  is the current cycle. The anode maximum solid phase concentration  $c_{\text{s,max,-}}$  in Eq.(eq ref) is also reduced per cycle as follows,

$$c_{\text{s,max,-}} = c_{\text{s,max,-}} \cdot \left( \frac{Q_{\text{new}}}{Q_{\text{nom}}} \right). \quad (3-37)$$

## Degradation Validation Method

Since there is no electro-chemical degradation model for the LGM50 battery, there are no available degradation parameters in research. As a result, the degradation parameters in Table A-2 were chosen from a battery with similar properties, and 2 parameters,  $k_{0,SEI}$  and  $i_{0,lpl}$  were tuned, thus being considered fitting constants, to match the LGM50 capacity fade behaviour.

The only information for capacity fade found for the LGM50 battery, was in its specification sheet, where the battery was cycled under the conditions in Fig.3-9.

### 4.2.3 Charge / discharge condition (I)

Cells shall be charged at constant current of 0.33C to 4.20V with end current of 1/20C. Cells shall be discharged at constant current of 0.33C to 2.85V. Cells are to rest 10 minutes after charge and 20 minutes after discharge at 25 °C ± 2 °C.

**Figure 3-9:** Cycling Experiment Conditions for LGM50 Battery. Taken from LGM50 Battery Specification Sheet.

Under the conditions mentioned, it was given that the battery fully fades (reaches %80 of nominal capacity) after 500 charge/discharge cycles as shown in Fig.3-10.

4.3.4 Cycle Life	Cells shall be charged and discharged per 4.2.3 for 500 cycles. A cycle is defined as one charge and one discharge. 501st discharge energy shall be measured per 4.2.1 and 4.2.2.	≥ 80% (of $Wh_{min}$ in 2.1)
---------------------	---	------------------------------

**Figure 3-10:** Degradation Capacity Fade Criteria for the LGM50 battery. Taken from the LGM50 Battery Specification Sheet

As a result, the parameters were tuned such that the cycle life criteria are followed. Since there are infinite combinations of the  $k_{0,SEI}$  and  $i_{0,lpl}$  that could achieve this, the parameters were chosen such that  $j_{lpl}$  is a few orders of magnitude lower than  $j_{SEI}$  in the first cycle, since aging is dominated by SEI in the first cycles and the nonlinear aging due to lithium plating occurs near the end of the cycle life.

## 3-5 Results

### 3-5-1 Performance Indicators

The two measures used to assess the accuracy of ESPM and SPMe are the Root Mean Square Error (RMSE) and the Variance Accounted For (VAF). The RMSE is given by,

$$RMSE = \sqrt{\frac{\sum_{k=1}^{T_{charge}/\Delta t} (y_k - \hat{y}_k)^2}{\frac{T_{charge}}{\Delta t}}} \quad (3-38)$$

where  $y_k$  is the measured output, which in that case would be the P2D model data, and  $\hat{y}_k$  is the predicted output, which in that case would be either ESPM or SPMe data. The VAF gives the % similarity between two signals,

$$VAF = \left(1 - \frac{\text{var}(y - \hat{y})}{\text{var}(y)}\right) \cdot 100\% \quad (3-39)$$

where "var" is the variance.

### 3-5-2 Battery Diffusion Model

In this section, the terminal voltage, cathode/anode surface electrolyte concentration and the corresponding current profile for the P2D model, SPMe and the ESPM based on experiments in Fig.3-1 to Fig.3-4 will be presented for the battery diffusion model subsection. This is done to graphically compare the ESPM accuracy with the P2D and SPMe models for the range of constant currents 0C-2C for a prolonged period of time, as well as show whether the model stays accurate for rapid variation of the currents within the same range. The reasoning behind choosing these variables in specific is that the terminal voltage  $U_{ocv}$  is a function of the SOC as shown in Eq.3-11 which is a function of the cathode/anode solid phase concentration  $c_{s,\pm}$ , thus showing the accuracy of model in terms of terminal voltage would be a suitable representative on how accurate the solid phase model behaves. As for the electrode electrolyte concentrations, it would be straightforward to state that it would be a good representative of the performance of the electrolyte phase dynamics.

Starting with the 1C constant charging experiment in Fig.3-11, it can be seen that in subplot (a), the shape of terminal voltage,  $U_{ocv}$ , is followed in similar manner for all models, where there is a minor positive deviation between the ESPM and P2D with an RMSE of 0.065 V and VAF of 97.82% and a small negative deviation between the SPMe and P2D with an RMSE of 0.0378 V and a VAF of 99.85%. This makes the SPMe more accurate by 1.6 times for terminal voltage in this case. As for the electrolyte concentration at both the anode and cathode current collector surfaces in subplot (b) and (c) respectively, there is almost a one to one fashion between the ESPM and the SPMe at the cathode, both a similar minimal magnitude of deviation between the P2D model, with an RMSE of 11.79 mol/m<sup>3</sup> and 17.02 mol/m<sup>3</sup> for the ESPM and SPMe as well as a VAF of 98.03 % and 98.34 % compared to the P2D respectively. This makes the ESPM more accurate than SPMe more accurate by 1.55 times for this variable at 1C constant charging current. As for subplot (c), the deviation in magnitude for the electrolyte concentration at the anode collector surface is noticeably more

apparent, with the ESPM and SPMe having an RMSE of  $17.24 \text{ mol/m}^3$  and  $31.46 \text{ mol/m}^3$  as well as a VAF of 91.75 % and 90.95% compared to the P2D respectively. This makes the ESPM more accurate than the SPMe by 1.82 times for this variable at 1C constant charging. The current profile can be found in subplot (d) where -5 A corresponds to 1C charging. The values for RMSE and VAF can be found at experiment 1 in Table 3-1 and Table 3-2 respectively.

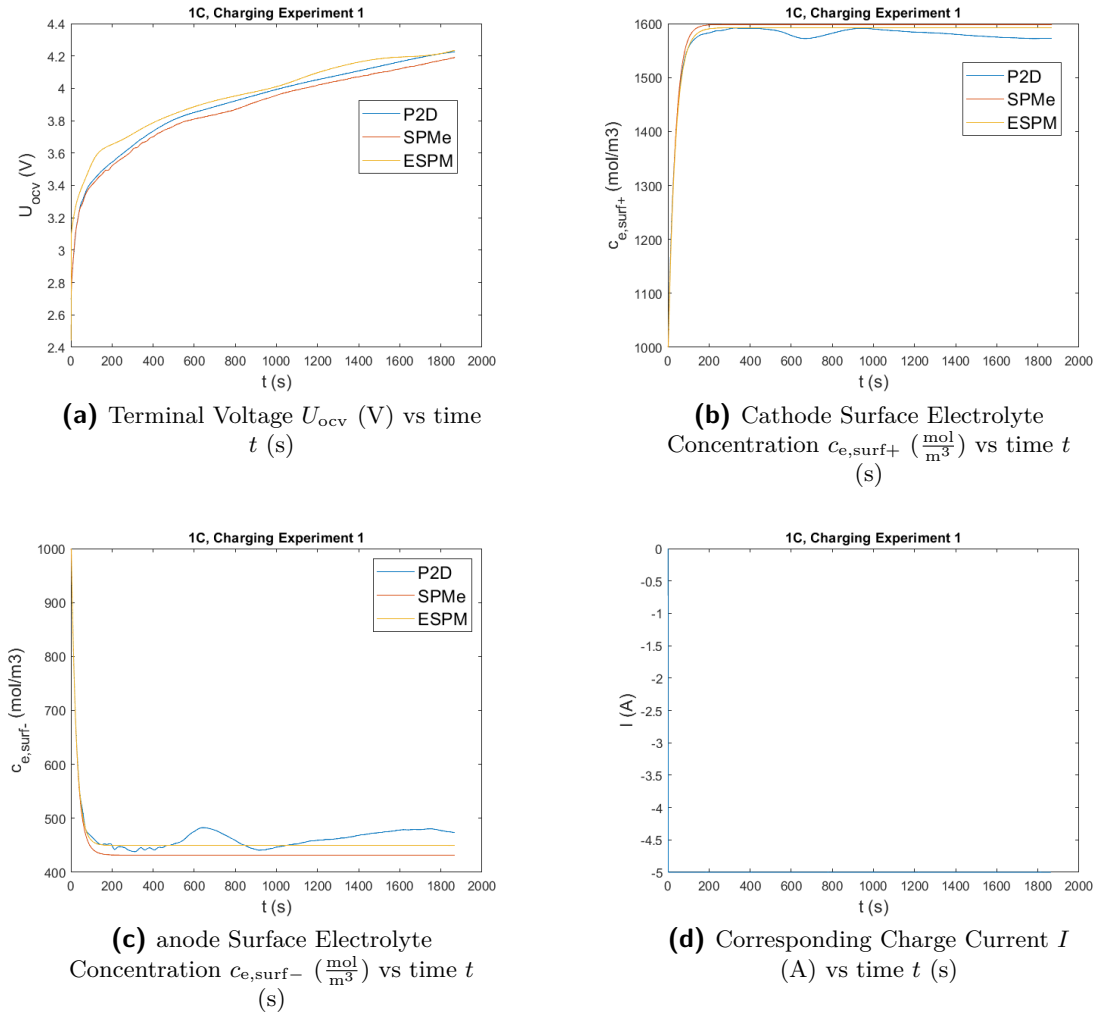


**Figure 3-11:** Experiment 1 (Fig.3-1) Results

As for the 2C constant charging experiment results shown in Fig.3-12, a lot of similarity is shown to the 1C constant charging experiment in terms of the performance of the SPMe compared to the ESPM with respect to the P2D model. Starting with the terminal voltage in subplot (a), it can be noticed that the SPMe shows almost a one to one similarity compared to the P2D model with an RMSE of 0.0099 V and VAF of 99.84 %, performing better than in the 1C constant charging experiment. The ESPM, however, expectedly performed worse than the 1C constant charging experiment, with an RMSE of 0.0913 and VAF of 92.33 % compared to the P2D model. As a result, the SPMe performs 9.22 times better than the ESPM for such

conditions. As for the cathode and anode current collector surface electrolyte concentrations in subplot (b) and (c) respectively, yet again, it can be seen that ESPM performed better than SPMe, with the ESPM and SPMe having an RMSE at the cathode of  $46.03 \text{ mol/m}^3$  and  $68.56 \text{ mol/m}^3$  as well as a VAF of 99.65 % and 98.98 % compared to the P2D respectively, meaning the ESPM performed 1.48 times better for that case. At the anode in subplot (c), the electrolyte concentration for the ESPM clearly performs better than the SPMe, with the ESPM and SPMe having an RMSE of  $28.89 \text{ mol/m}^3$  and  $90.70 \text{ mol/m}^3$  as well as a VAF of 96.20 % and 95.58 % compared to the P2D model respectively making the performance of both models are similar in terms of RMSE, whereas the VAF shows otherwise, with ESPM performing better by 3.14 times than the SPMe for this variable at such conditions. The current profile can be shown in subplot (d). The values for RMSE and VAF can be found at experiment 2 in Table 3-1 and Table 3-2 respectively.

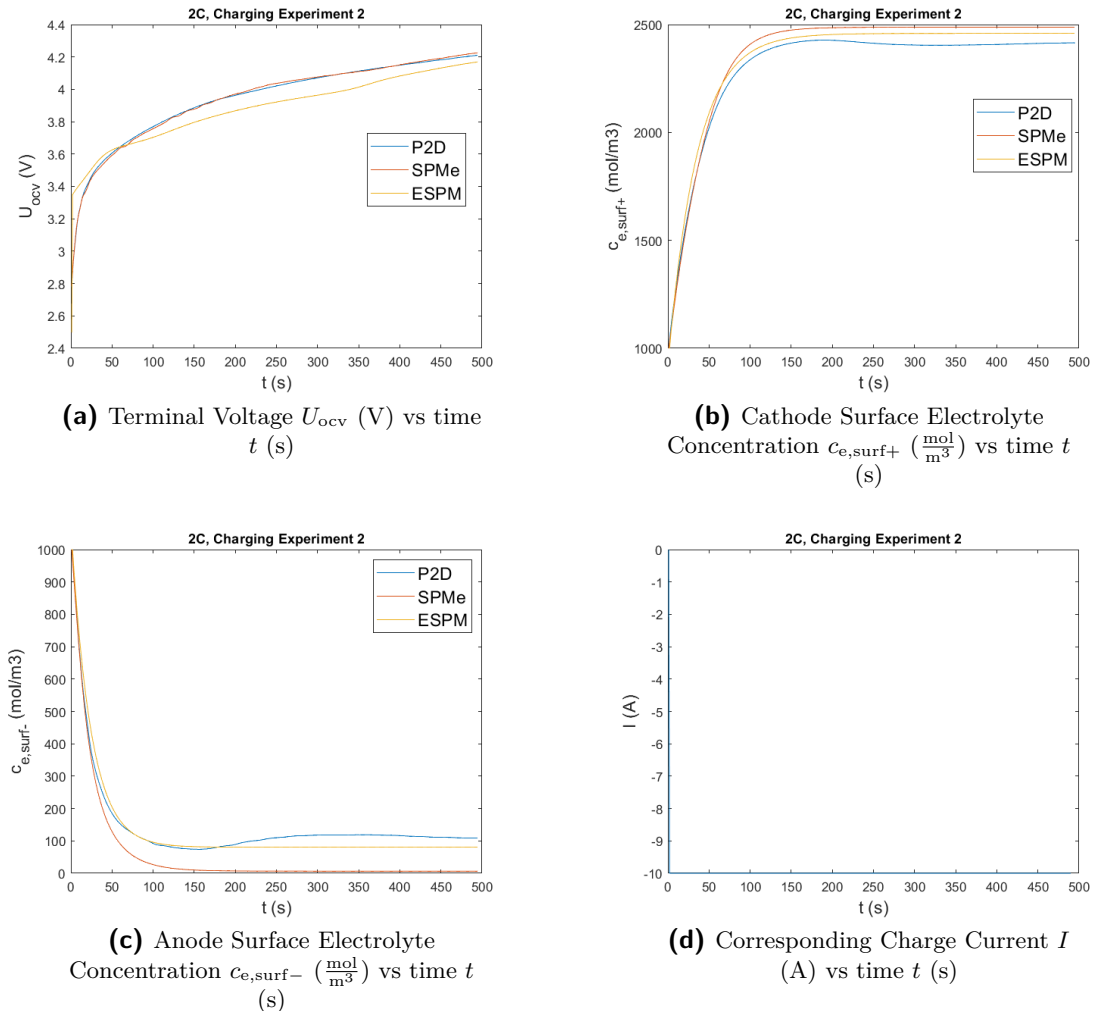


**Figure 3-12:** Experiment 2 (Fig.3-2) Results

The models were then tested under the varying charging current experiment in Fig.3-3 to show how the approximated models behave under rapid variation of current. The results for

this experiment can be found in Fig.3-13. It can be seen that for the terminal voltage in subplot (a), the SPMe is unaffected showing very high accuracy whereas the ESPM accuracy reduced, with the ESPM and SPMe having an RMSE 0.1612 V and 0.0115 V as well as a VAF of 93.42 % and 99.92 % compared to the P2D model respectively, thus the SPMe performing 14.7 times better in that case. As for the cathode surface electrolyte concentration in subplot (b), the accuracy is not heavily influenced with rapid variation of current, with the ESPM and SPMe having an RMSE of 14.8 mol/m<sup>3</sup> and 28.11 mol/m<sup>3</sup> as well as a VAF of 99.87 % and 99.75% compared to the P2D respectively, making the ESPM 2 times better than SPMe for that case. Similarly, the accuracy of the ESPM and SPMe are minimally affected for variation in current for the anode collector surface concentration in subplot (c), with an RMSE of 8.21 mol/m<sup>3</sup> and 37.84 mol/m<sup>3</sup> as well as a VAF of 99.97 % and 99.1 % compared to the P2D model respectively with the ESPM performing 4.61 times better for this variable at that case. The charge current profile in [A] can be found in subplot (d). The values for RMSE and VAF can be found at experiment 3 in Table 3-1 and Table 3-2 respectively.

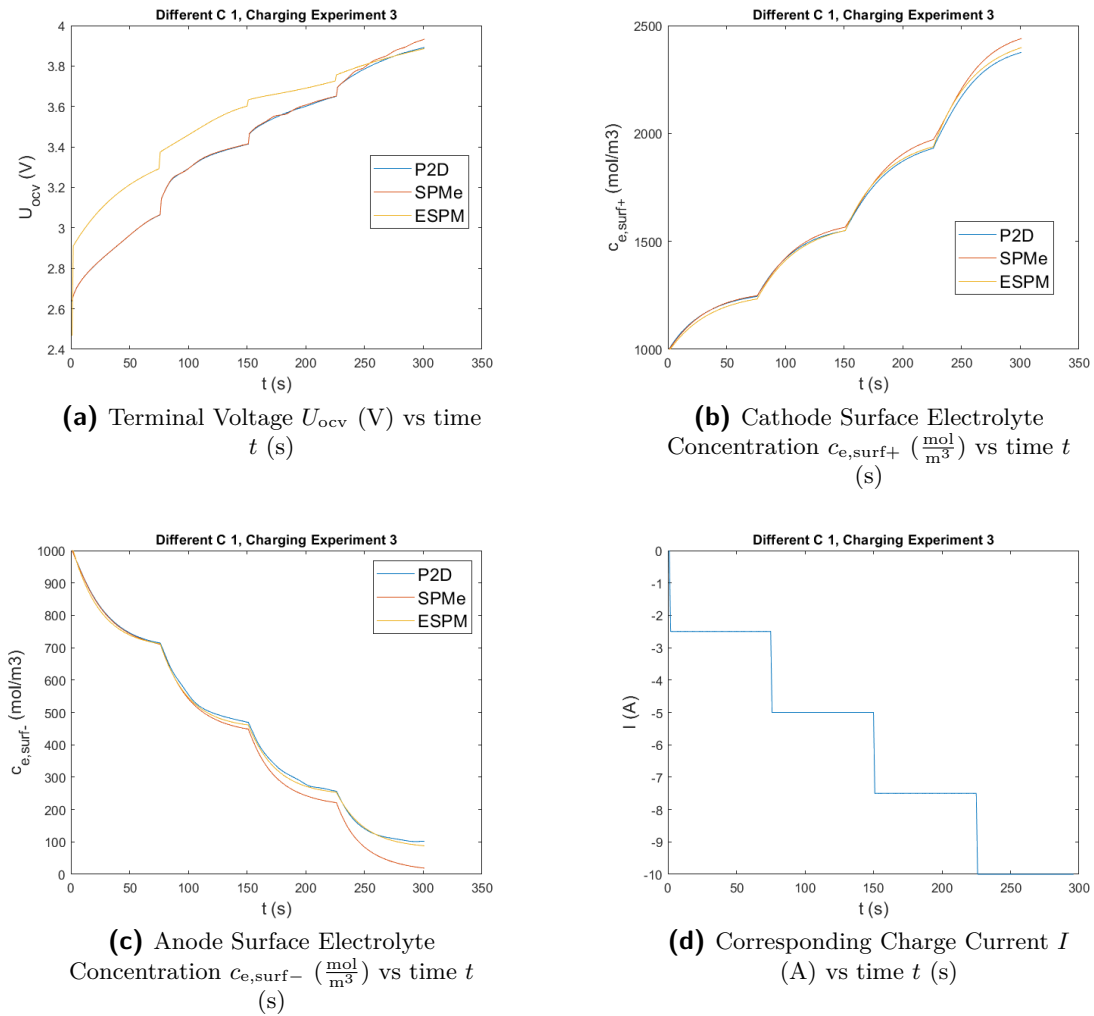


**Figure 3-13:** Experiment 3 (Fig.3-3) Results

To further validate the varying charge current profile case, the varying current experiment in Fig.3-4 results were plotted as shown in Fig.3-14. Similar results were shown for that case, with ESPM and SPMe having an RMSE of 0.1224 V and 0.0066 V as well as a VAF of 94.98 % and 99.98 for the terminal voltage case in subplot (a), an RMSE of 23.51 mol/m<sup>3</sup> and 23.14 mol/m<sup>3</sup> as well as VAF of 99.69 % and 99.81 % for the cathode surface electrolyte concentration case in subplot (b), an RMSE of 17.77 mol/m<sup>3</sup> and 31.52 mol/m<sup>3</sup> as well as a VAF of 99.79 % and 99.38 % for the anode surface electrolyte concentration case in subplot (c), all compared to the P2D model. This means the SPMe performs better by 19 times for the terminal voltage, whereas same performance is shown for the cathode surface electrolyte concentration and the ESPM performs better by 1.77 times for the anode surface electrolyte concentration. The charging current profile in [A] can be found in subplot (d). The values for RMSE and VAF can be found at experiment 4 in Table 3-1 and Table 3-2 respectively.

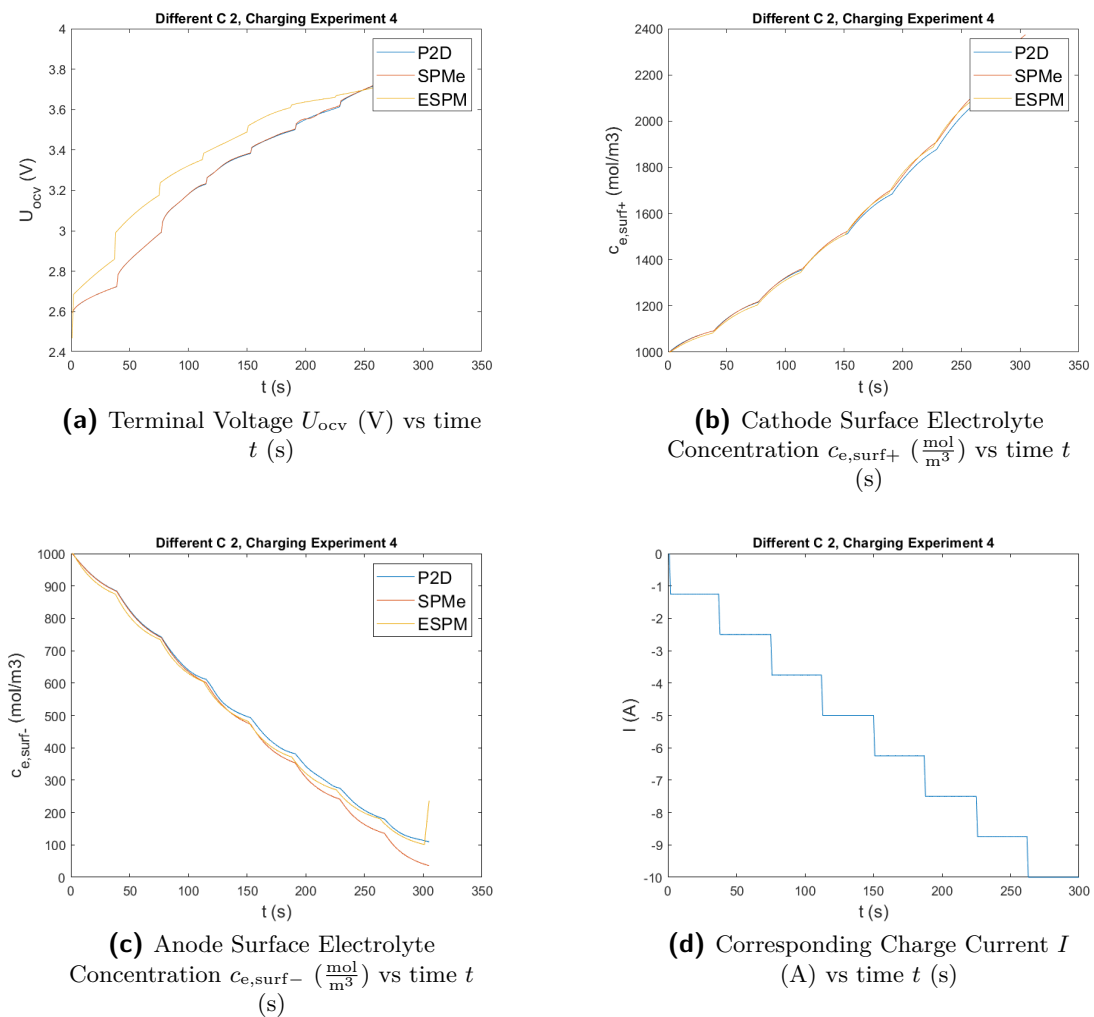


**Figure 3-14:** Experiment 4 (Fig.3-4) Results

<i>Variable</i>	Experiment no.	VAF SPMe vs P2D	VAF ESPM vs P2D
$U_{ocv}$ (V)	1	99.85	97.82
$U_{ocv}$ (V)	2	99.84	92.33
$U_{ocv}$ (V)	3	99.92	93.42
$U_{ocv}$ (V)	4	99.98	94.98
$c_{e,surf+}$	1	98.34	98.03
$c_{e,surf+}$	2	98.98	99.65
$c_{e,surf+}$	3	99.75	99.87
$c_{e,surf+}$	4	99.81	99.69
$c_{e,surf-}$	1	90.95	91.75
$c_{e,surf-}$	2	95.58	96.20
$c_{e,surf-}$	3	99.10	99.97
$c_{e,surf-}$	4	99.38	99.79

**Table 3-2:** Table of VAF between SPMe and P2D model as well as between ESPM and P2D model for the results in Fig.3-11 to Fig.3-14. The experiment numbers 1 to 4 follow experiments in Fig.3-1 to Fig.3-4 respectively.

<i>Variable</i>	Experiment no.	RMSE SPMe vs P2D	RMSE ESPM vs P2D
$U_{ocv}$ (V)	1	0.0378	0.0605
$U_{ocv}$ (V)	2	0.0099	0.0913
$U_{ocv}$ (V)	3	0.0115	0.1612
$U_{ocv}$ (V)	4	0.0066	0.1224
$c_{e,surf+}$ ( $\frac{mol}{m^3}$ )	1	17.02	11.79
$c_{e,surf+}$ ( $\frac{mol}{m^3}$ )	2	68.56	46.03
$c_{e,surf+}$ ( $\frac{mol}{m^3}$ )	3	28.11	14.80
$c_{e,surf+}$ ( $\frac{mol}{m^3}$ )	4	23.14	23.51
$c_{e,surf-}$ ( $\frac{mol}{m^3}$ )	1	31.46	17.24
$c_{e,surf-}$ ( $\frac{mol}{m^3}$ )	2	90.70	28.89
$c_{e,surf-}$ ( $\frac{mol}{m^3}$ )	3	37.84	8.21
$c_{e,surf-}$ ( $\frac{mol}{m^3}$ )	4	31.52	17.77

**Table 3-1:** Table of RMSE between SPMe and P2D model as well as between ESPM and P2D model for the results in Fig.3-11 to Fig.3-14. The experiment numbers 1 to 4 follow experiments in Fig.3-1 to Fig.3-4 respectively.

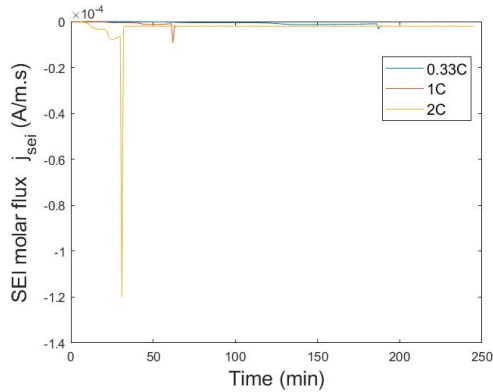
### 3-5-3 Degradation Model

For this subsection, 3 constant charging experiments, 0.33C, 1C and 2C were performed and were cycled 1000 times, meaning 500 charge cycles and 500 discharge cycles were performed. The discharge cycle performed is according to Fig.3-9. The 0.33C charging experiment was performed under the conditions in Fig.3-9. The 1C and 2C charge experiments were performed such that battery is fully charged and the total simulation time (resting + charging) is the same for all experiments for a fair comparison.

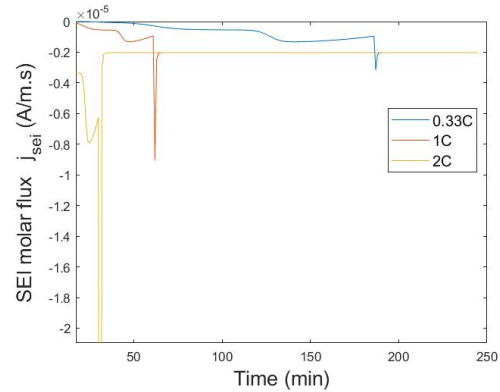
As a recap from the methodology section, the two main criteria that are expected to be followed after properly tuning  $k_{0,sei}$  and  $i_{0,lpl}$  are as follows,

- In the first charging cycle, the magnitude of  $j_{sei}$  is a few orders higher than  $j_{lpl}$ .
- Under the experiment conditions in Fig.3-9, the battery is cycled and shows capacity fade behaviour according to Fig.3-10.

After several adjustments, the degradation tuning parameters following both criteria were chosen to be  $k_{0,sei} = 2.481.14 \times 10^{-13}$  and  $i_{0,lpl} = 21.14 \times 10^{-3}$ , where they can also be found in Table A-2. Firstly, for the 3 constant charging experiments, the SEI and lithium plating molar fluxes  $j_{sei}$  and  $j_{lpl}$  from the first charging cycle were plotted as in Fig.3-15 and Fig.3-16. Comparing the magnitude of the  $j_{sei}$  and  $j_{lpl}$  it can be seen that  $j_{sei}$  has an order of magnitude of  $10^{-4}$ , 4 orders of magnitude higher than  $j_{lpl}$  with an order of magnitude of  $10^{-8}$ , following the first criteria, since the degradation is dominated by  $j_{sei}$  in the first few cycles, then the effect of lithium plating becomes more prevalent in the last few cycles, and mostly at high charge/discharge rates. It can also be noticed that the magnitude of  $j_{sei}$  and  $j_{lpl}$  increases as the current increases, with  $j_{sei}$  having an average value of  $-1.4771.14 \times 10^{-8}$ ,  $-1.53651.14 \times 10^{-6}$  and  $-5.68e1.14 \times 10^{-6} \frac{A}{m.s}$  across the charging period for 0.33C, 1C and 2C charging experiments respectively. The same occurs with  $j_{lpl}$ , with an average of  $-1.621.14 \times 10^{-13}$ ,  $-3.391.14 \times 10^{-11}$  and  $-1.621.14 \times 10^{-10} \frac{A}{m.s}$  for 0.33C, 1C and 2C charging experiments respectively. The shape of  $j_{sei}$  and  $j_{lpl}$  for the different currents can be seen to be closely similar to each other as seen for 0.33C in Fig.3-15 (a) and Fig.3-16 (a) respectively, for 1C and 2C showed in the zoomed in plots in Fig.3-15 (b) and Fig.3-16 (b), where a gradual increase in magnitude occurs, then a peak in  $j_{sei}$  and  $j_{lpl}$  right before the end of a charging period, and finally as the battery goes to rest (0C),  $j_{sei}$  and  $j_{lpl}$  settle at an equilibrium point which is non-zero, meaning the model incorporates calendar aging as well. Note that as the battery settles from a higher current, the peak  $j_{sei}$  and  $j_{lpl}$  increases drastically, specifically at high charge rates. For example, tripling the current from 0.33C to 1C changes such a peak  $j_{sei}$  from  $-6.321.14 \times 10^{-6} \frac{A}{m.s}$  to  $-1.81.14 \times 10^{-5} \frac{A}{m.s}$ , 2.85 times increase, whereas doubling the current from 1C to 2C increases the peak  $j_{sei}$  from  $-1.81.14 \times 10^{-5} \frac{A}{m.s}$  to  $0.00024 \frac{A}{m.s}$ , increasing by 11.1 times, showing the significance of degradation at high charge rates. The same case goes for  $j_{lpl}$  where tripling the current from 0.33C to 1C changes such a peak  $j_{lpl}$  from  $-1.561.14 \times 10^{-10} \frac{A}{m.s}$  to  $-5.321.14 \times 10^{-10} \frac{A}{m.s}$ , 3.41 times increase, whereas doubling the current from 1C to 2C increases the peak  $j_{lpl}$  from  $-5.321.14 \times 10^{-10} \frac{A}{m.s}$  to  $-1.091.14 \times 10^{-8} \frac{A}{m.s}$ , increasing by 69.87 times. When the battery is at rest,  $j_{sei}$  settles at an equilibrium of  $-4.061.14 \times 10^{-6} \frac{A}{m.s}$  for all charge cases, whereas  $j_{lpl}$  settles at an equilibrium of  $-9.321.14 \times 10^{-11} \frac{A}{m.s}$  for all charge cases.

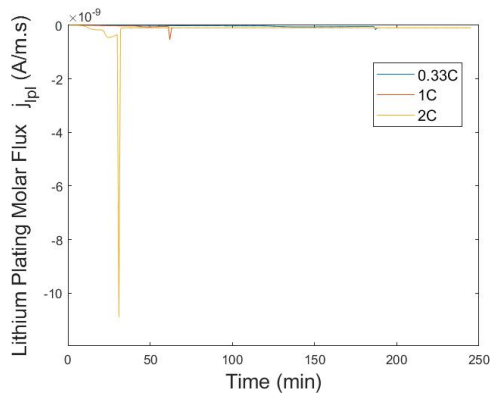


(a) Plot of the  $j_{sei}$  ( $\frac{A}{m \cdot s}$ ) for 0.33C, 1C and 2C constant current charging strategies.

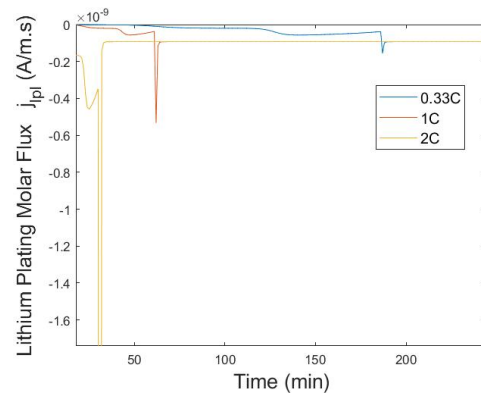


(b) Zoomed in plot of the SEI molar flux  $j_{sei}$  ( $\frac{A}{m \cdot s}$ ) for 0.33C, 1C and 2C constant current charging strategies.

Figure 3-15



(a) Plot of the Lithium plating molar flux  $j_{pl}$  for 0.33C, 1C and 2C constant current charging strategies.



(b) Zoomed in plot of the Lithium plating molar flux  $j_{pl}$  for 0.33C, 1C and 2C constant current charging strategies.

Figure 3-16

The updated capacity per cycle is then plotted for the 1000 cycles (500 charge/discharge cycles) for the 3 charge experiments as shown in Fig.3-17. It can be seen in Fig.3-17 that the capacity fade model under the conditions in Fig.3-10 is captured in this model, since under 0.33C constant charging, the capacity reaches 80% of its nominal capacity. The nonlinear relationship between current and capacity fade is shown, since tripling the current from 0.33C to 1C causes only a 6.9 % decrease in the capacity reaching 74.5% after 500 charge/discharge cycles, whereas doubling the current from 1C to 2C causes a 22.8% decrease in the capacity reaching 57.5% of its nominal capacity after 500 charge/discharge cycles, showing the degradation significantly increases at high charge rates.

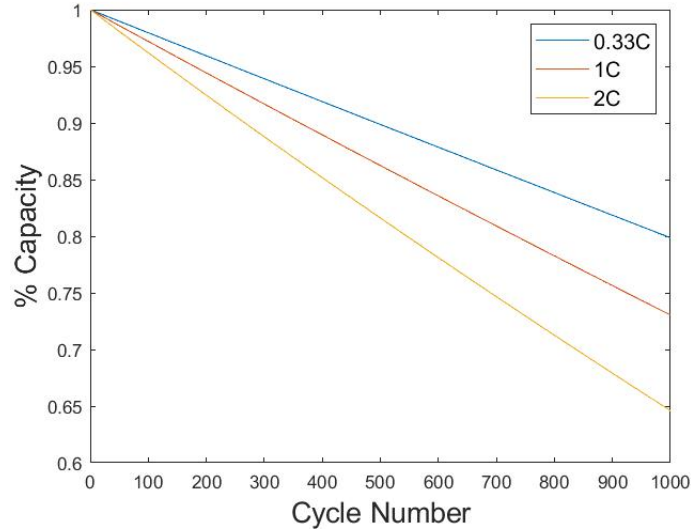


**Figure 3-17:** Plot of capacity fade against number of cycles for the LGM50 battery for 0.33C, 1C and 2C constant charging experiments. Discharging experiment is according to Fig.3-9.

## 3-6 Discussion

### 3-6-1 Battery Diffusion Model

Overall, it can be concluded that for terminal voltage estimation, the SPMe outperforms the ESPM by on average 11.1 times, whereas for the electrolyte concentration, the ESPM on average is more accurate by 1.25 and 2.85 times for the cathode and anode respectively. Even though the SPMe shows higher accuracy for the terminal voltage, the VAF for the ESPM is higher than 90 % for all the experiments performed, meaning the ESPM would be applicable for use for modelling the terminal voltage the range of currents 0C-2C. At higher charging C-rates, the accuracy for specifically the terminal voltage reduces, having VAF below 90 %, thus not being shown. For the electrolyte concentration, it can be concluded that it can be used for the range of currents 0C-2C, as shown in the result plots, as well the minimal RMSE and VAF near 100 % for most cases.

The reason for the differences in  $U_j$  between the ESPM and the P2D/SPMe would be the initial jumps in terminal voltage in the first time step then the shape is followed for all cases. The reason for this is how the molar fluxes and solid phase concentrations are modelled for the ESPM compared to the P2D and SPMe. Since terminal voltage  $U_j$  is directly influenced by the solid phase concentration  $c_{s,surf,j}$  as in Eq.3-11 or below Eq.2-4, a deeper look is taken on the  $c_{s,j}$  or  $\bar{c}_{s,j}$  evolution equations that are directly proportional with  $c_{s,surf,j}$ . Starting with the ESPM, it can be seen that rate of change of the volume averaged solid phase concentration  $\bar{c}_{s,j}$  in Eq.3-1 is linearly dependent on the molar flux  $j_j$ . Looking at the equation for  $j_j$  in Eq.3-2, it can be seen that it is only a function of the current  $I$ . As a result, when initially current switches from 0C to any value, an initial positive or negative jump of concentration occurs depending on the electrode which results in the initial jump in terminal voltage. As for the P2D and SPMe, the nonlinear dependencies of the rate of change in  $c_{s,j}$  observed in

Eq.2-1 or Eq.2-14 as well as the nonlinearity  $j_j$  seen in Eq.2-4, results in a smoother overall  $U_j$  curve with changing currents.

### 3-6-2 Degradation Model

The results have mainly shown that the capacity fade conditions in Fig.3-10 are followed under the experiment conditions in Fig.3-9, and the nonlinear relation between the current and the capacity fade is shown from the curvature in the capacity fade lines as cycles progress. The second validation criteria is also followed by looking at the SEI and lithium plating molar fluxes  $j_{SEI}$  and  $j_{lpl}$  in Fig.3-15 and Fig.3-16 respectively, where  $j_{lpl}$  is shown to be 3 orders of magnitude lower than  $j_{sei}$ . Since the 2 criteria are followed, it could be concluded that the capacity fade model represents a good approximation of how the LGM50 capacity fade behaviour. On the other hand, there are infinite combinations of  $k_{0,sei}$  and  $i_{0,lpl}$  degradation fitting parameters that could satisfy the 2 criteria mentioned, thus to further improve the model, real experimental degradation validation data for the LGM50 battery is needed to correct on the capacity fade model currently developed.

For the degradation molar fluxes  $j_{sei}$  and  $j_{lpl}$ , the main discussion point is the sudden peaks of  $j_{sei}$  and  $j_{lpl}$  occurring at the the instant the battery goes to rest and fully charged for all strategies, then settling at an equilibrium  $j_{sei}$  and  $j_{lpl}$ , showing the influence of calendar aging. The peaks occur due to the slow response of the surface electrolyte concentrations  $c_{e,surf,-}$  and  $c_{e,surf,+}$  with respect to change in current. Looking at the variables in the exponent in  $j_{sei}$  and  $j_{lpl}$  Eq.3-14 and Eq.3-16 respectively, as the current goes to 0, it can be seen that the solid phase electrode potential  $\Phi_s$  in Eq.3-7 instantly goes to 0 as well as  $j_-$  (Eq.3-2) in  $j_{tot}$  (Eq.3-12) goes to 0 due to the explicit relation with current. As for the electrolyte potentials at the surface of the anode  $\Phi_{e,-}$  in Eq.3-10, there is an explicit dependence with the electrolyte concentrations at the surface of the electrodes. For example, when the current changes to 0 from any current, it takes 2 samples for the electrolyte surface concentration to reach equilibrium, as shown in Fig.4-5 (a) and (b) (Note: this plot is referred to once here, but will be explained in detail in the next chapter), meaning that  $\Phi_{e,-}$  is the dominant term influencing both  $j_{sei}$  and  $j_{lpl}$  at these time instances. Similarly, it takes the  $j_{sei}$  and  $j_{lpl}$  2 samples to reach equilibrium, the first sample it reaches the peak, then the second sample reaching the rest value. Moreover, the larger the difference in anode and cathode surface concentrations leads to a larger peak in both  $j_{sei}$  and  $j_{lpl}$ . The influence of the  $j_{sei}$  and  $j_{lpl}$  from the previous time step in  $j_{tot}$  is neglected due to having insignificantly low orders of magnitude.

The nonlinear relation between the current and the capacity fade is due to the exponential relation between the current in  $j_{int}$  (Eq.3-2) in  $j_{tot}$  (Eq.3-12) in the degradation molar flux equations  $j_{sei}$  and  $j_{lpl}$  in Eq.3-14 and Eq.3-16 respectively. Also, the significant change in the capacity fade with changing current show that high charge rates show to be the main aging mechanism. A more in depth analysis on relation between current and capacity fade will be given in the next chapter.

As for the constant relation of the resting equilibrium  $j_{sei}$  and equilibrium  $j_{lpl}$  with time, given that the capacity fade equation is given by Eq.3-31, shows that the relation of capacity fade due to calendar aging is linear with time, since the integral of a constant function is a linear function.

### 3-7 Conclusion

In this chapter, the solid phase, electrolyte phase and the degradation models were discussed, in detail. Starting with solid phase model the P2D model and the SPMe, experiment conditions as well simulation methodology were discussed. As for the ESPM, since this model has been implemented from scratch in MATLAB, the model equations were introduced, as well as how it was implemented and simulated on MATLAB.

For the electrolyte phase dynamics, the linear transfer function model arising from the P2D model was described, as well as the methodology at which how the transfer function was obtained using MATLAB and Python (PyBamm) was explained.

Following this, the results for the full battery model implemented were shown and discussed, in which it was concluded that the battery model is applicable for the range of current 0C-2C. Afterwards, the equations for the degradation model implemented were introduced, then the method at which how they are implemented on MATLAB was shown, and lastly the results for the degradation model were shown and discussed, where it was concluded that while the real degradation parameters for the LGM50 battery are not available, the degradation model is still a good representative of how the capacity fade of this battery would behave, since the 2 degradation validation criteria of followed. However, accuracy can be significantly improved if real degradation data is available for the LGM50.

# Charging Strategy Implementation

## 4-1 Introduction

As concluded in the literature, the charging strategy to be implemented is an optimization based charging strategy, where in particular a combination of 2 papers were chosen. A variation of the cost function by Lin and colleagues [44] that tackles the 2 main aging mechanisms, Solid Electrolyte Interphase (SEI) and lithium plating growth, as well as the charging time, combined with the NMPC formulation discussed by Yin and colleagues [77]. As a note, while some inspiration is taken from previous studies, the following method combined with the battery and degradation model being applied implemented, is considered new. This is discussed in more detail in the "Conclusions and Recommendations" chapter. The symbol definitions, units and parameter values can be found in Table A-1 and A-2 in Appendix A-1.

## 4-2 Model Formulation

### 4-2-1 Nonlinear Model Predictive Control (NMPC) Description

The Model Predictive Control (MPC) is a multi-variable, feedback optimization based control method, which is currently widely popular as it is one of the few feedback control strategies with constraint handling properties. The general linear MPC algorithm is that at each time step, a convex, quadratic programming problem is solved as many times as the number of time steps within a prediction horizon. This then gives an optimal predicted trajectory with the length of the prediction horizon and an optimal input trajectory with the length of the control horizon. The first input is then chosen as the optimal one for that time step, then the problem is shifted one step into the future. The same procedure is then repeated every time step across the simulation horizon. A summarized step by step description of the algorithm can be found in Fig.4-1.

- Given:** Mathematical model  $f$ , initial condition  $x(0)$ , prediction horizon  $p$ , control horizon  $m$ , sampling time  $\Delta t$ , and weighting matrices  $Q$ , and  $R$
- Step 1:** At the current sampling time  $t_k$ , set  $x(t_{k-1}) \leftarrow x(t_k)$
- Step 2:** Solve Formulation II for a sequence of  $m$  optimal input variables  $\{U(1), U(2), \dots, U(m)\}$
- Step 3:** Set  $u(t_k) \leftarrow U(1)$  and inject the input to the plant
- Step 4:** At the sampling time instant  $t_{k+1}$ , obtain the plant measurement  $y_m$
- Step 5:** Corresponding to  $y_m$ , estimate the states  $x^+(t_{k+1})$   
(this work assumes full state feedback, for which all the states are measurable)
- Step 6:** Set  $t_k \leftarrow t_{k+1}$
- Step 7:** If state/input constraints are violated, terminate algorithm, else go to Step 8
- Step 8:** Shift the prediction horizon  $p$  forward and repeat Step 1

**Figure 4-1:** MPC/NMPC algorithm description [37].

An extension to MPC is NMPC, when the model dynamics are nonlinear, making the optimization problem to be solved more complex, due to the change of constraints from linear to nonlinear, and the cost function changing from a quadratic to a non-convex function. As a result, non-convex optimization algorithm is required to solve this problem, increasing computational cost.

In the case of the charging strategy formulation, since there are nonlinear dynamics, for example in the degradation dynamics from Eq.3-14 to Eq.3-17, an NMPC charging strategy will be formulated and solved. The computational time will then be assessed to check real time control applicability, and whether further simplifications to the control problem are needed.

#### 4-2-2 NMPC Charging Strategy Formulation

The general NMPC cost function to be solved looks as follows,

$$\begin{aligned}
 J(\mathbf{x}(k+i), u(k+i)) &= \varphi(\mathbf{x}(k+i), u(k+i)) \quad \forall k = 1, \dots, N_T, \quad i = 1, \dots, p \\
 \text{Subject to:} \\
 \mathbf{x}(k+i+1) &= f(\mathbf{x}(k+i), u(k+i)) \quad k = 1, \dots, N_T, \quad i = 1, \dots, p \\
 u_{LB} &\leq u(k+i) \leq u_{UB}, \quad k = 1, \dots, N_T, \quad i = 1, \dots, m \\
 \mathbf{x}_{LB} &\leq \mathbf{x}(k+i) \leq \mathbf{x}_{UB} \quad k = 1, \dots, N_T, \quad i = 1, \dots, p
 \end{aligned} \tag{4-1}$$

where  $N_T$  is the simulation horizon (sum of charging and resting period),  $i$  is the step in the prediction/control horizon,  $p$  is the prediction horizon which is taken to be the same as the control horizon  $m$  to reduce complexity of the problem,  $\mathbf{x}$  is the state vector,  $u$  is the input to be optimized in the control problem,  $\mathbf{x}_{UB}$  and  $\mathbf{x}_{LB}$  are upper and lower bounds on the states

respectively, and  $u_{UB}$  and  $u_{LB}$  are upper and lower bounds on the input, with

$$\mathbf{x} = \begin{bmatrix} \bar{q}_+ \\ \bar{q}_- \\ \bar{c}_{s,+} \\ \bar{c}_{s,-} \\ c_{e,\text{surf},+} \\ c_{e,\text{surf},-} \\ c_{\text{sei}} \\ c_{\text{lpl}} \\ j_{\text{int}} \\ j_{\text{sei}} \\ j_{\text{lpl}} \end{bmatrix}, \quad u = I. \quad (4-2)$$

Thus there are  $n_x = 11$  states and  $n_u = 1$  inputs. Following [16], the cost  $\varphi$  given as,

$$\begin{aligned} \varphi = & \sum_{i=1}^p \left( \mathbf{x}(k+i) - \mathbf{x}^{\text{set}} \right)^T Q \left( \mathbf{x}(k+i) - \mathbf{x}^{\text{set}} \right) \\ & + \sum_{i=1}^m \left( u(k+i) - u(k+i-1) \right)^T R \left( u(k+i) - u(k+i-1) \right) \end{aligned} \quad (4-3)$$

where  $Q$  is an  $n_x \times n_x$  square diagonal matrix penalizing the difference between the states and the reference state vector  $\mathbf{x}^{\text{set}}$ .  $R$  is an  $n_u \times n_u$  matrix penalizing the change in the input.  $Q$ ,  $R$  and  $\mathbf{x}^{\text{set}}$  are chosen in way such that the following cost is minimized,

$$\begin{aligned} \varphi = & \sum_{i=1}^p \left( (\bar{c}_{s,-}(k+i) - c_{s,\text{max},-})^2 \cdot q_4 + (j_{\text{sei}}(k+i))^2 \cdot q_{10} + (j_{\text{lpl}}(k+i))^2 \cdot q_{11} \right) \\ & + \sum_{i=1}^m \left( u(k+i) - u(k+i-1) \right)^T R \left( u(k+i) - u(k+i-1) \right) \end{aligned} \quad (4-4)$$

The values for  $N_T, m, p$  can be found in section 4-3-3 and  $u_{LB}$ ,  $u_{UB}$ ,  $\mathbf{x}_{LB}, \mathbf{x}_{UB}$ ,  $Q$  and  $R$  can be found in the appendix Section B-2.

It can be seen that the optimal current profile is chosen based on a the minimization of the square of 3 main variables, the  $\bar{c}_{s,-} - c_{s,\text{max}}$ ,  $j_{\text{sei}}$  and  $j_{\text{lpl}}$ . Starting with  $\bar{c}_{s,-} - c_{s,\text{max}}$ , the purpose of this is for the volume-averaged anode concentration to track a reference volume-averaged concentration for the fully charged case. Since, there is a direct relation between this variable and the State Of Charge (SOC) as in Eq.3-9, this variable is responsible for tracking the SOC towards an SOC for the fully charged case. As a result, the penalty weighting for this variable influences the charging time. As for the  $j_{\text{sei}}$  and  $j_{\text{lpl}}$ , since these variables are directly proportional with the capacity fade, minimizing such variables would correspond to minimizing the capacity fade per cycle and how much weighting penalty on each variable corresponds to how much influence on removing SEI or lithium plating degradation respectively.

As for the constraints in Eq.4-1, the first constraint is an equality constraint which represents the battery and degradation model for the Extended Single Particle Model (ESPM) described in Section 3-1 and 3-2. This is used as a verification that the state is correctly updated each

time step. The second and third constraints are inequality constraints that bound the states and inputs to be within acceptable ranges. The main bound constraints are as follows,

$$\begin{aligned}
c_{s,\max,-} \times stoic_{d,-} &\leq \bar{c}_{s,-} \leq c_{s,\max,-} \times stoic_{c,-}, \\
c_{s,\max,+} \times stoic_{c,+} &\leq \bar{c}_{s,+} \leq c_{s,\max,+} \cdot stoic_{d,+}, \\
c_{e,\text{surf},-} &\geq 0, \\
c_{e,\text{surf},+} &\geq 0 \\
0 &\leq I \leq 2C
\end{aligned} \tag{4-5}$$

where the first 2 constraints are to prevent overcharging and undercharging, and the second 2 constraints are to prevent battery permanent damage.

## 4-3 Methodology

Details on how the NMPC problem above was formulated and simulated using MATLAB are given.

### 4-3-1 MATLAB Nonlinear Optimizer "fmincon"

The MATLAB function "**fmincon**" is a nonlinear solver, that finds the local/global minimum of a constrained optimization problem. The function has the following form,

$$u^* = fmincon(fun, u_0, A, b, A_{eq}, b_{eq}, lb, ub, nonlcon, options), \tag{4-6}$$

where  $u^*$  is the optimal solution obtained, which in this case is the optimal current profile for a certain prediction/control horizon, **fun** is the cost function to be minimized, which in this case is in Eq.4-3,  $u_0$  is the initial solution to the problem across a certain prediction/control horizon, having the following input arguments, **A** and **b** are used to set up the linear inequality constraints of the problem, which is left unused for this case, **A<sub>eq</sub>** and **b<sub>eq</sub>** are the linear equality constraints, which are also unused, **lb** and **ub** are lower and upper bounds on  $u$ , thus bounding the current, **nonlcon** is used to formulate the nonlinear/linear inequality and equality constraints, **options** are the solver options.

#### Setting up "fun"

The first argument considered in the problem is the cost function **fun**, which takes the symbolic vector **u** which is the vector to be optimized. The symbolic vector **u** has the same length as the initial solution  $u_0$ , which is the length of the prediction/control horizon, since an optimal state trajectory of length  $n_x \cdot (p+1)$  is obtained from an optimal solution of inputs  $u^*$  of length  $n_u \cdot (p)$ . An initial state vector  $x_0$  is given, and the cost function to be minimized is then written as follows,

$$\begin{aligned}
\mathbf{u}^* = \min_{\mathbf{u}} & \left( X_p(\mathbf{u}) - X_p^{\text{set}} \right)^T Q_p \left( X_p(\mathbf{u}) - X_p^{\text{set}} \right) + \\
& \left( \mathbf{u}(2:p) - \mathbf{u}(1:p-1) \right)^T R_{p-1} \left( \mathbf{u}(2:p) - \mathbf{u}(1:p-1) \right)
\end{aligned} \tag{4-7}$$

where,

$$\begin{aligned}
 X_p &= \begin{bmatrix} \mathbf{x}_0 \\ \mathbf{x}_1 \\ \vdots \\ \mathbf{x}_p \end{bmatrix}_{\{n_x(p+1)\}} & \mathbf{u}_{p-1} &= \begin{bmatrix} u_0 \\ u_1 \\ \vdots \\ u_{p-1} \end{bmatrix}_{\{n_u \times p\}} \\
 Q_p &= \begin{bmatrix} Q & 0 & 0 & \dots & 0 \\ 0 & Q & 0 & \dots & 0 \\ \vdots & \vdots & \vdots & & \vdots \\ 0 & 0 & 0 & \dots & Q \end{bmatrix}_{\{(n_x \cdot (p+1)) \times (n_x \cdot (p+1))\}} & R_{p-1} &= \begin{bmatrix} R & 0 & 0 & \dots & 0 \\ 0 & R & 0 & \dots & 0 \\ \vdots & \vdots & \vdots & & \vdots \\ 0 & 0 & 0 & \dots & R \end{bmatrix}_{\{n_u \cdot (p+1) \times (n_u \cdot (p+1))\}}
 \end{aligned} \tag{4-8}$$

### Setting up "nonlcon"

The argument **nonlcon** is a function with 1 input  $\mathbf{u}$ , and 2 outputs  $c_{\text{eq}}$ , which represents the nonlinear or linear equality constraints and  $c_{\text{ineq}}$  for the nonlinear or linear inequality constraints. Both types of constraint sets consist of constraints for each time step of the prediction/control horizon. This function will be used for the state inequality constraints  $c_{\text{ineq}}$ . As for the state equality constraints (state dynamics), they will be neglected since they are indirectly included in the **fmincon** arguments, for example to obtain the state trajectory  $p$  steps in the future, for obtaining both cost function in **fun** and  $c_{\text{ineq}}$  across the prediction/control horizon. The format of  $c_{\text{ineq}}$  is as follows,

$$c_{\text{ineq}} \leq 0. \tag{4-9}$$

Following such format,  $c_{\text{ineq}}$  can be split as follows,

$$\begin{aligned}
 c_{\min} &= -X_p(p \cdot n_x + 3 : p \cdot n_x + 6) + \mathbf{x}_{\min}, \\
 c_{\max} &= X_p(p \cdot n_x + 3 : p \cdot n_x + 4) - \mathbf{x}_{\max}, \\
 c_{\text{ineq}} &= \begin{bmatrix} c_{\min} \\ c_{\max} \end{bmatrix}.
 \end{aligned} \tag{4-10}$$

where,

$$\mathbf{x}_{\min} = \begin{bmatrix} c_{s,\max,-} \cdot \text{stoic}_{d,-} \\ c_{s,\max,+} \cdot \text{stoic}_{c,+} \\ 0 \\ 0 \end{bmatrix} \quad \mathbf{x}_{\max} = \begin{bmatrix} c_{s,\max,-} \cdot \text{stoic}_{c,-} \\ c_{s,\max,+} \cdot \text{stoic}_{d,+} \end{bmatrix} \tag{4-11}$$

It can be seen that the lower bound constraints have been imposed on state 3 to state 6, being  $\bar{c}_{s,+}$  to  $c_{e,\text{surf},-}$  and upper bound on states 3 and 4, being states  $\bar{c}_{s,+}$  and  $\bar{c}_{s,-}$  respectively following Eq.4-2, thus covering the state inequality constraints in Eq.4-5. It can also be noticed that constraints were only imposed on the final time step of the prediction horizon. This is done to reduce complexity, as the bound state constraints do not vary with time, and constraining only the last time step of the prediction horizon would ensure that the states chosen would not violate the constraints for all previous steps within a prediction horizon.

### Setting up "lb" and "ub"

The arguments **lb** and **ub** in **fmincon** are used to set lower and upper bounds for the solutions respectively across a prediction horizon, thus covering the last inequality constraint on the charging current. Since the charge current bound is across the prediction horizon, **lb** and **ub** will be vectors looking as follows,

$$lb = \begin{bmatrix} -10 \\ -10 \\ \vdots \\ -10 \end{bmatrix}_{\{p \times 1\}} \quad ub = \begin{bmatrix} 0 \\ 0 \\ \vdots \\ 0 \end{bmatrix}_{\{p \times 1\}} \quad (4-12)$$

where -10 [A] represents 2C charging.

### Setting up "options"

The argument **options** in **fmincon** are the solver options. They are mostly kept as the default options, but 2 main options are adjusted to reduced the computational complexity, 'MaxFunctionEvaluations' and 'TypicalX'. 'MaxFunctionEvaluations' is the maximum number of function evaluations allowed in the optimization algorithm, which has been reduced from the default value of 3000 to 500, which was tested to minimally influence the local/global optimal solution. 'TypicalX' is an option which gives a guess on what the optimal solution profile (current profile) might look like for a certain prediction horizon. This is set to the optimal current profile for the prediction horizon at the previous time step of the charging period. This showed to significantly increase computational speed. The algorithm to solve the optimization problem was kept to the default one, being the 'interior point method' due to the ability to handle large, sparse problems, and the fastest compared to the rest of the algorithms available in **fmincon**.

### Obtaining Optimal Charge Profile

For each step of the charging period, an optimal charge profile with the length of the prediction horizon is obtained using **fmincon**. From that charge profile, only the first current point is applied, the dynamics are shifted one step with that current, and the process is repeated until the constraints are violated, or the preset charging period done.

#### 4-3-2 Choosing the weights $Q$ and $R$

The method used to choose the penalty weighting  $Q$ , is choosing the base  $Q$  in a way such that normalizes the 3 main states to have an equal contribution to the cost. For example, looking the first state cost  $(\bar{c}_{s,-} - c_{s,\max,-})^2$  in Eq.4-4, the range of values this cost term can take are  $[0, (c_{s,\max,-} - stoic_{d,-} \cdot c_{s,\max,-})^2]$ . As a result, an initial value for  $q_4$  is  $q_{4,base} = \frac{1}{(c_{s,\max,-} - stoic_{d,-} \cdot c_{s,\max,-})^2}$ . As for the second term in the cost,  $j_{sei}^2$  in Eq.4-4, first to determine the maximum value the  $j_{sei}^2$ , an constant charging experiment with the maximum possible current while satisfying

the constraints (in this case 2C) was performed, since this would achieve the maximum possible  $j_{sei}$ . From this experiment, the peak  $j_{sei,max}^2$  was recorded and the weighting  $q_{10}$  was chosen to be  $q_{10} = \frac{1}{j_{sei,max}^2}$ . The same procedure was performed  $j_{lpl}$  and  $q_{11}$  was chosen to be  $q_{11} = \frac{1}{j_{lpl,max}^2}$ . This would then result in having an equal cost contribution for the 3 variables, when solving the optimization algorithm. The weights are then adjusted according to the charging goals. Results of the max current (2C) constant charging experiments for  $j_{sei}$  and  $j_{lpl}$ , showing the peak values for both, can be found in Fig.4-2 and Fig.4-3 respectively. A table of the peak values for the  $(\bar{c}_{s,-} - stoicd_{,-} \cdot c_{s,max,-})^2$ ,  $j_{sei,max}^2$ ,  $j_{lpl,max}^2$  and their corresponding base weights can be found in Table.4-1. The same approach is performed, for obtaining the weighting on  $R$ , where the maximum magnitude obtained for the change in current is 2C (abs(-10) A) and the square peak magnitude is  $2C^2$  (100), thus the base weight for  $R$  is  $\frac{1}{100}$ .

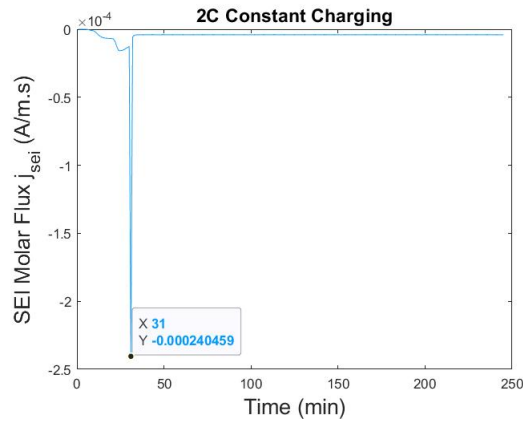


**Figure 4-2:** Plot of the  $j_{sei}$  against time (min) under a 2C constant charging experiment. The peak  $abs(j_{j_{sei,max}}) = 0.00024 \frac{A}{m \cdot s}$ .

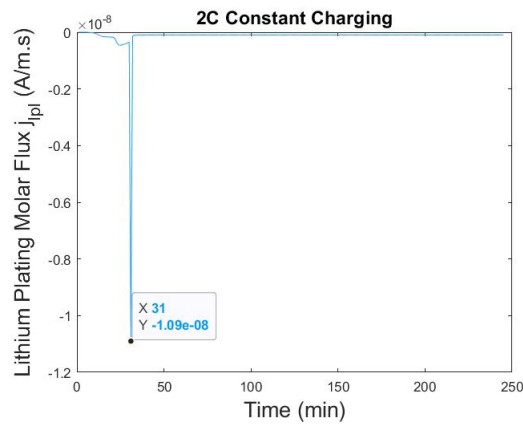


**Figure 4-3:** Plot of the  $j_{lpl}$  against time (min) under a 2C constant charging experiment. The peak  $abs(j_{j_{lpl,max}}) = 1.09e - 08 \frac{A}{m \cdot s}$ .

Variable	Peak Magnitude	Peak Squared Magnitude	Base $q$
$\bar{c}_s, -c_{s,\max,-}$	29583	875153889	1.14e-9
$\dot{j}_{sei}$	0.00024	5.76e-8	1736111
$\dot{j}_{lpl}$	1.09e-8	1.1881e-16	8.41e15

**Table 4-1:** Table of the maximum possible magnitude and squared magnitude of the 3 variables to be minimized  $\bar{c}_s - c_{s,\max,-}$ ,  $\dot{j}_{sei}$ ,  $\dot{j}_{lpl}$ .

### 4-3-3 NMPC Parameters

#### Sampling Period $T_s$

The sampling period has been chosen to be 60 s since it is the highest  $T_s$  where the battery and degradation dynamics do not fail, as well reducing computational time. A higher sampling period heavily reduces accuracy, as well as the solid/electrolyte phase model going unstable.

#### Prediction Horizon $p$ and Control Horizon $m$

The prediction Horizon  $p$  has been chosen to be  $p = 5$  samples, meaning the NMPC algorithm looks 5 minutes in the future when computing an optimal current for a specific time instance. After some trials, 5 minutes was seen to be sufficient, with the optimal solution minimally affected at higher values for  $p$ , meaning that the optimal solution is almost the same with increasing  $p$ , thus the lowest value not affecting the optimal solution significantly was chosen to save computational time per iteration. The control horizon  $m$  was chosen to be equal to the prediction horizon for the same reason being reducing the complexity of the NMPC problem.

#### Simulation Horizon $N_T$

The simulation horizon was chosen in a way such that the full charging period is captured for all charging strategies, as well as not increasing simulation time per strategy heavily.  $N_T = 80$  (80 minutes) was chosen for all strategies, meaning the total simulation time for all strategies are the same for a fair capacity fade comparison.

## 4-4 Results

The NMPC control charging strategy has been performed for 6 different cases as follows,

- Case 1 "Fast": Only charging speed focus with  $q_4 =$ ,  $q_{10} = 0$  and  $q_{11} = 0$  and  $R = 0$  in Eq.4-3
- Case 2 "SEI focus": Only SEI growth reduction focus with  $q_4 = 1.14 \times 10^{-11}$ ,  $q_{10} = 17361110$  and  $q_{11} = 0$  and  $R = 0$  in Eq.4-3
- Case 3 "LPL focus" : Only Lithium Plating growth reduction focus with  $q_4 = 1.14 \times 10^{-11}$ ,  $q_{10} = 0$  and  $q_{11} = 8.41 \times 10^{14}$  and  $R = 0$  in Eq.4-3.

- Case 4: Both SEI and Lithium Plating growth reduction focus with  $q_4 = 1.14 \times 10^{-11}$ ,  $q_{10} = 1736111$  and  $q_{11} = 8.41 \times 10^{15}$  and  $R = 0$  in Eq.4-3.
- Case 5 "Health Conscious Fast + Delta u": Tradeoff between charging speed and degradation as well as penalizing the changing current with  $q_4 = 1.14 \times 10^{-9}$ ,  $q_{10} = 1736111$  and  $q_{11} = 8.41 \times 10^{15}$  and  $R = 0.01$  in Eq.4-3.

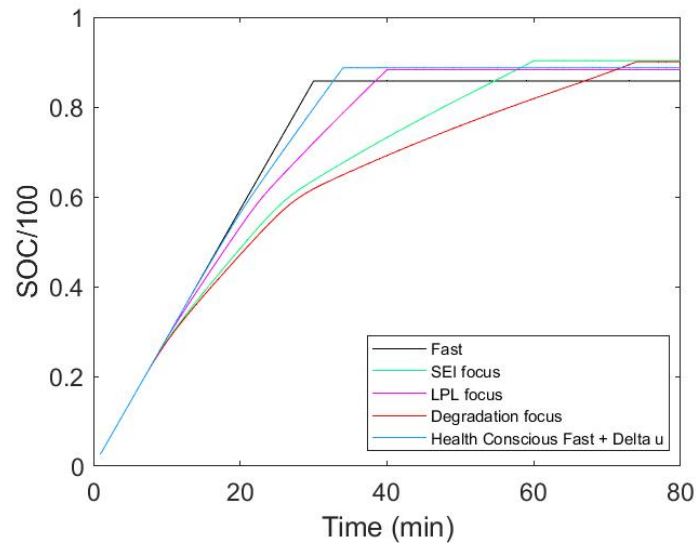
the first case being focusing only on charging speed, the second case focusing mainly on reduction of the SEI growth, the third case focusing on the reduction lithium plating growth, fourth focusing on penalizing both degradation mechanisms, the fifth being penalizing the 3 variables as well as the change in input current in a way to achieve health conscious fast charging. The results can be found in Fig.4-4, Fig.4-5, Fig.4-6, Fig.4-7 and Fig.4-8.

#### 4-4-1 Constraint Satisfaction

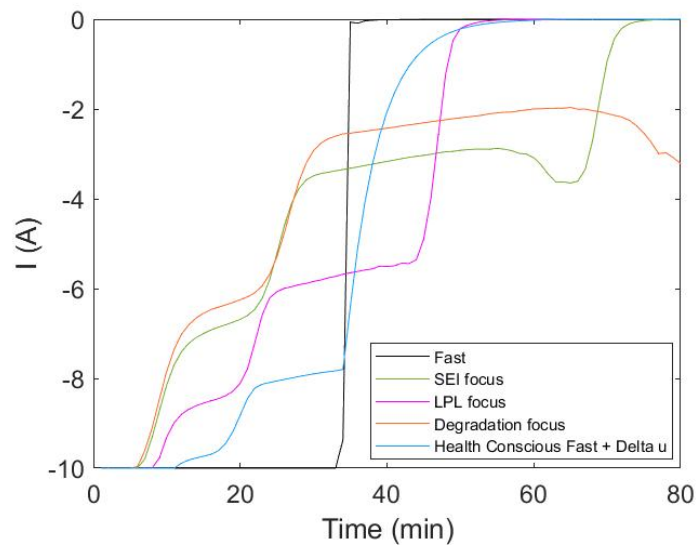
In order to check how each strategy performs in terms charging speed and whether the constraints in Eq.4-5 are satisfied, the SOC, current (A) and the surface electrolyte concentration ( $\frac{\text{mol}}{\text{m}^3}$ ) at the anode and cathode were plotted against time (min) in Fig.4-4 and Fig.4-5 respectively. It can be noticed that the constraints are all followed, where no over or undercharging occurs since the SOC stays within the specified limits for all charging cases in Fig.4-4 (a). The current profiles for all charging cases stay within the specified  $[0 \text{ 2C}]$  ( $[-10 \text{ 0}]$  A) as seen in Fig.4-4. Lastly, the surface electrolyte concentrations at the anode and cathodes in Fig.4-5 (a) and Fig.4-5 (b) respectively, where it can be seen that the electrolyte concentrations are always above 0, following the constraints.

#### 4-4-2 Charging Speeds

As for charging speeds, by looking at the SOC plot in Fig.4-4 (a), the fastest charging strategy is the "Fast" charging strategy, having a charge time of 31 minutes. The corresponding current profile is expectedly a constant max charge current (-10 A) satisfying the bounds throughout the whole charge period. The slowest strategies are the ones focusing only on either one or both degradation mechanisms, with the slowest being "Degradation focus" with a charge time of 74 minutes, followed by "SEI focus" with a charge time of 60 minutes, then "LPL focus" with a charge time of 40 minutes. The corresponding charge profiles have a similar shape, showing a nonlinear response to the degradation, SEI and lithium plating focus strategies. The "Health Conscious Fast +Delta u" charging algorithm, focusing on both charging speed and degradation, turned to be the second fastest charging algorithm, with a charging time of 34 minutes. One thing noticed about the corresponding current profile in Fig.4-4 (b), is that there are no sharp peaks or changes in current and the current profile is smooth throughout the charging period. This shows the effect of penalizing the changing current, compared to the rest of the other strategies that do not include change in current influence, where sharp fluctuations are noticed.

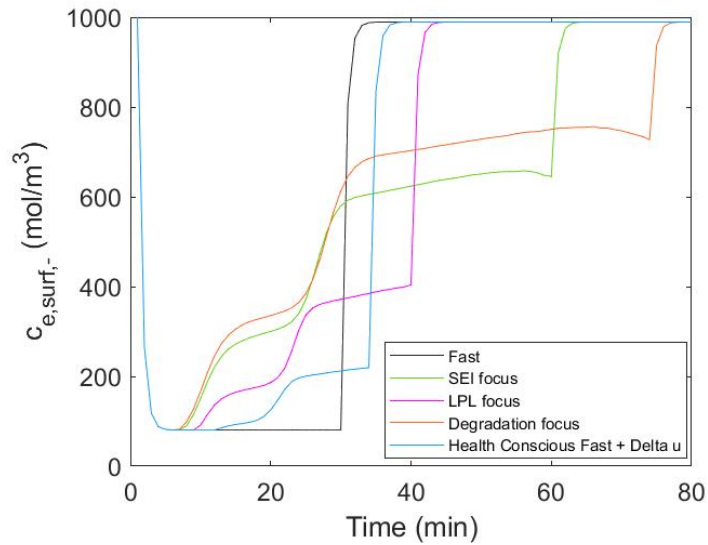


(a) Plot of the SOC against time (min) for the various charging strategies.

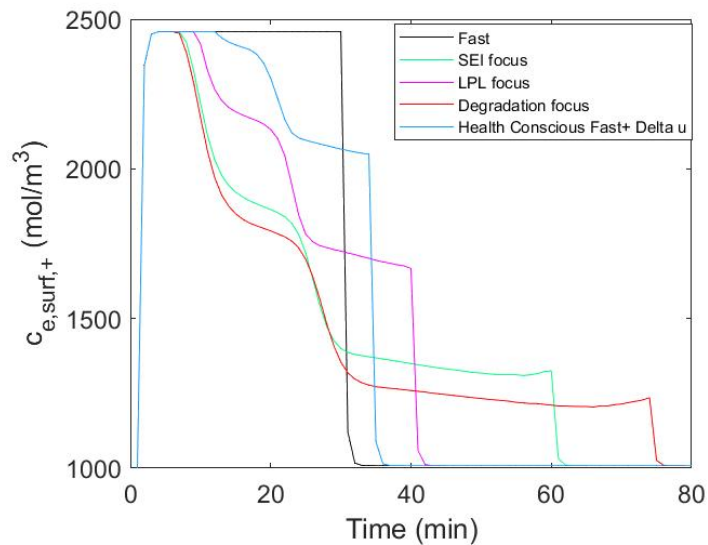


(b) Plot of the current profile  $I$  (A) against time (min) for the various charging strategies.

**Figure 4-4:** Plot of SOC and the corresponding charging profile against time for the various charging strategies.



(a) Plot of the anode surface electrolyte concentration  $c_{e,surf,-}$  ( $\frac{\text{mol}}{\text{m}^3}$ ) against time (min) for the various charging strategies.



(b) Plot of the cathode surface electrolyte concentration  $c_{e,surf,+}$  ( $\frac{\text{mol}}{\text{m}^3}$ ) against time (min) for the various charging strategies.

**Figure 4-5:** Plots of Anode and Cathode Electrolyte Concentrations  $c_{e,surf,+}$  and  $c_{e,surf,-}$  under various charging strategies.

### 4-4-3 Degradation Results

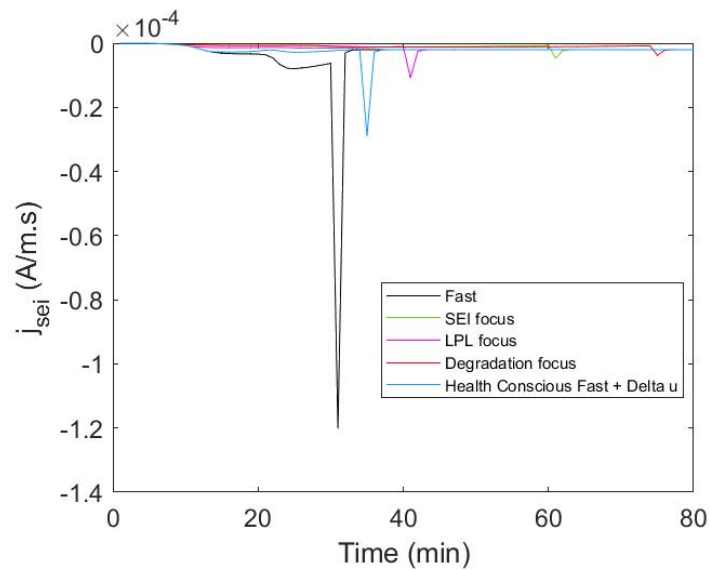
For degradation, it can be noticed from  $j_{sei}$  and  $j_{lpl}$  plots in Fig.4-6 and Fig.4-7 respectively that the highest peak was shown for the "Fast" charging strategy, having a peak  $j_{sei,max} = -0.00012$  and peak  $j_{lpl,max} = -1.09 \times 10^{-8}$ . It also showed the highest aver-

age, with average  $j_{sei,avg} = 3.57 \times 10^{-6}$  and average  $j_{lpl,avg} = -2.25 \times 10^{-10}$ . Consequently, the capacity fade was highest for the "Fast" charging strategy shown in Fig.4-8, losing 8.1 % of its capacity 550 cycles.

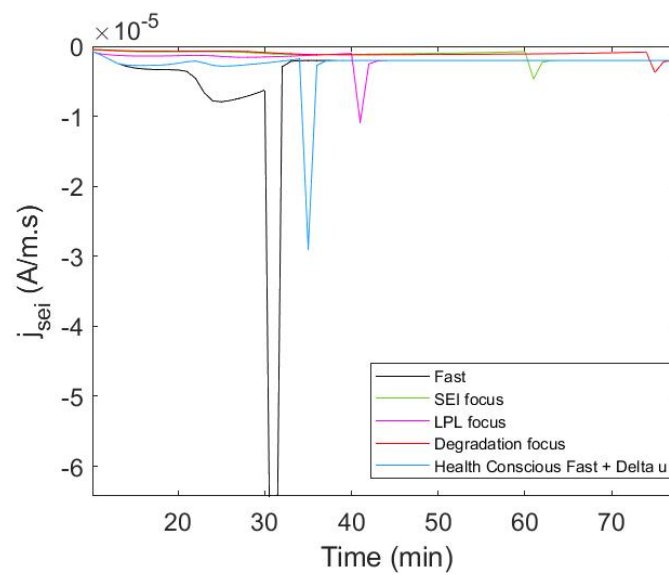
At the other end of the spectrum, the strategy showing the least degradation is the "Degradation Focus" strategy, where from Fig.4-6 and Fig.4-7 (b) respectively it can be noticed that peak  $j_{sei,max} = -3.75 \times 10^{-6}$  and peak  $j_{lpl,max} = -1.9 \times 10^{-10}$  and average  $j_{sei,avg} = -7.43 \times 10^{-7}$  and  $j_{lpl,avg} = -2.98 \times 10^{-11}$  are the lowest amongst all other charging strategies. The "SEI focus" showed similar behaviour to the "Degradation focus" strategy as noticed in Fig.4-6 and Fig.4-7, showing a peak  $j_{sei,max} = -4.70 \times 10^{-6}$  and  $j_{lpl,max} = -2.48 \times 10^{-10}$ . as well as  $j_{sei,avg} = -1.09 \times 10^{-6}$  and  $j_{lpl,avg} = -4.63 \times 10^{-11}$ . The similarity is reflected in the capacity fade plot, where the "Degradation focus" and "SEI focus" lost 6.3% and 6.4% capacity after 550 cycles respectively.

The "LPL focus" strategy showed higher degradation, having a peak  $j_{sei,max} = -1.09 \times 10^{-5}$  and  $j_{lpl,max} = -6.6 \times 10^{-10}$  as well as average  $j_{sei,avg} = -6.9 \times 10^{-7}$  and average  $j_{lpl,avg} = -2.74 \times 10^{-11}$ . The higher degradation is reflected in the capacity fade plot in Fig.4-8, losing 7 % capacity after 550 cycles.

Lastly, the "Health Conscious Fast +Delta u" charging showed the lowest degradation after the strategies focusing only on either one or both degradation mechanisms, having a peak  $j_{sei,max} = -2.9 \times 10^{-5}$  and peak  $j_{lpl,max} = -2.07 \times 10^{-9}$  as well as average  $j_{sei,avg} = -2.23 \times 10^{-6}$  and average  $j_{lpl,avg} = -1.14 \times 10^{-10}$  by looking at Fig.4-6 and Fig.4-7 respectively. As for capacity fade, it can be seen from Fig.4-8, that the "Health Conscious Fast+Delta u" charging strategy caused a loss of 7.1% capacity of 550 cycles. A table summarizing the most important results can be found in Table 4-2.

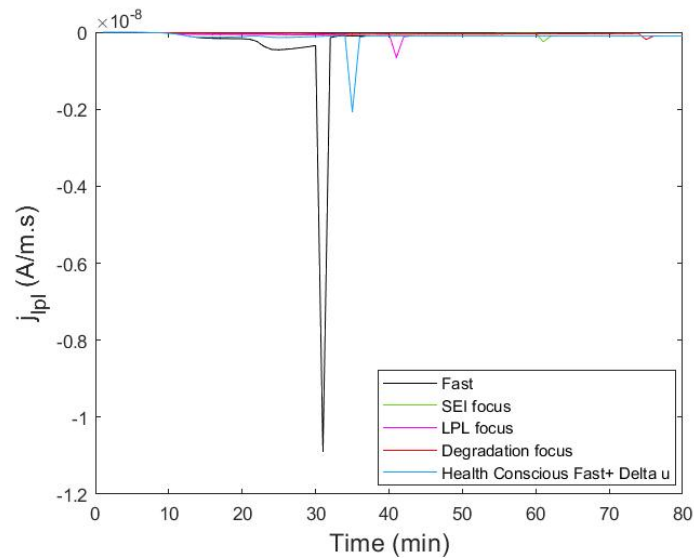


(a) Plot of the  $j_{sei}$  ( $\frac{A}{m \cdot s}$ ) against time (min) for the various charging strategies.

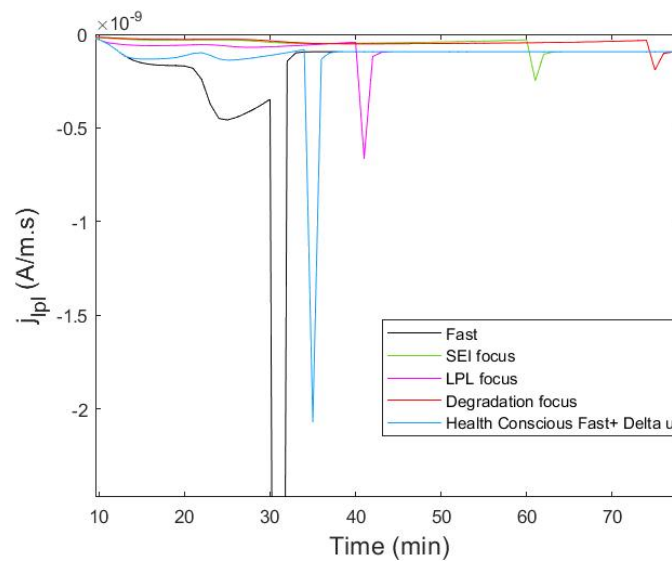


(b) Zoomed in plot of the  $j_{sei}$  ( $\frac{A}{m \cdot s}$ ) against time (min) for the various charging strategies.

**Figure 4-6:** Original and zoomed in plots of SEI molar flux  $j_{sei}$  ( $\frac{A}{m \cdot s}$ ) against time (min) for the various NMPC charging strategies.



(a) Plot of the  $j_{lpl}$  ( $\frac{A}{m \cdot s}$ ) against time (min) for the various charging strategies.



(b) Zoomed in plot of the  $j_{lpl}$  ( $\frac{A}{m \cdot s}$ ) against time (min) for the various charging strategies.

**Figure 4-7:** Original and zoomed in plots of Lithium Plating molar flux  $j_{lpl}$  ( $\frac{A}{m \cdot s}$ ) against time (min) for the various NMPC charging strategies.

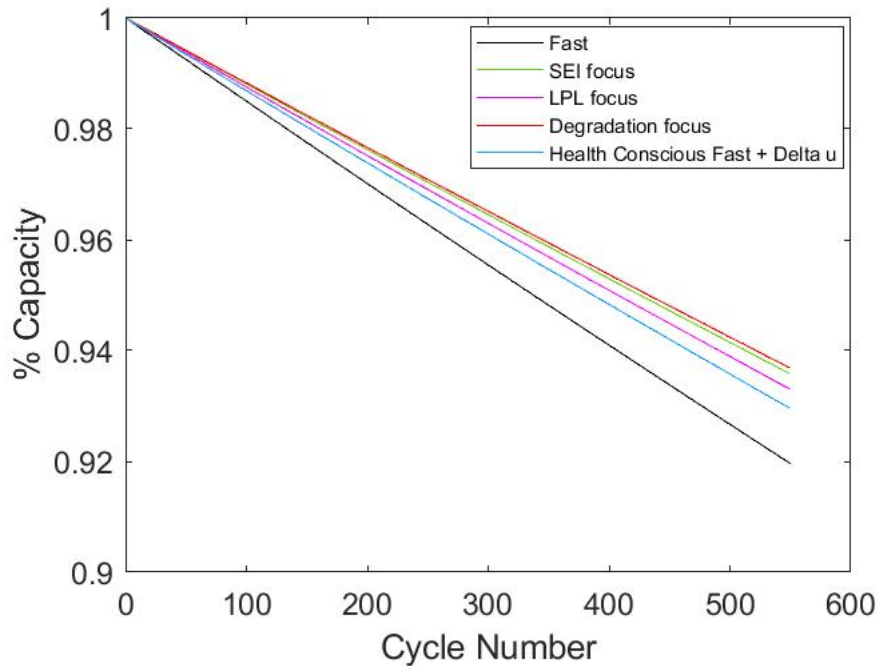


**Figure 4-8:** Plot of the capacity (%) against the cycle number for for the various charging strategies. 2 cycles correspond to one charge and one discharge. The method at which this plot is obtained is closely similar to the methodology in Section 3-3-3

Charging Strategy	Charging Time (min)	Capacity Fade (%) After 550 Cycles	Cycle number at 80 % Capacity
Fast (1)	31	8.1%	1358
SEI focus (2)	60	6.4 %	1720
LPL (3)	40	7 %	1571
Degradation focus (4)	74	6.3 %	1750
Health Conscious Fast + Delta u (5)	34	7.1 %	1550

**Table 4-2:** Summary of Charging Speed and Degradation Results per Strategy.

Charging Strategy	Average CPU time per iteration (s) $T_s = 30s$	Average CPU time per iteration (s) $T_s = 60s$
Fast (1)	6.6172	4.2933
SEI focus (2)	76.0602	14.82
LPL focus (3)	45.8917	17.2449
Degradation focus (4)	65.7082	18.9207
Health Conscious Fast + Delta u (5)	36.4646	6.6172

**Table 4-3:** Computational time (s) of the different charging strategies.

#### 4-4-4 Computational Time

The computational time per iteration for all charging strategies were assessed for  $T_s = 30s$  and  $T_s = 60s$ . For  $T_s = 60s$ , an average computational time per iteration 12.37 s over all strategies, showing that real time control is applicable at this sampling period, since CPU time is significantly lower than the sampling time. On the other hand, reducing the sampling period to  $T_s = 30s$  heavily increases the computational time having an average computational time of 46.15 s, thus real time control is not applicable for this case. The average CPU time per iteration for each strategy can be found in Table 4-3.

## 4-5 Discussion

Starting with the charging times, the main charging strategy, "Health Conscious Fast + Delta u" showed to be 1.13 times slower than the fastest charging strategy "Fast", and 2.17 times faster than the slowest strategy "Degradation Focus" charging strategy. The difference in charging speeds is reflected on the current profiles of each of the strategies in Fig.4-4 (b), where the average current is highest for the "Fast" strategy  $I_{avg} = -10A$ , and lowest for "Degradation Focus" with  $I_{avg} = -5.1472A$  and second highest for the "Health Conscious Fast +Delta u" strategy with  $I_{avg} = -9A$ . Looking at the volume averaged concentration at the anode  $\bar{c}_{s,j}$  in Eq.3-1, it can be seen that the rate of change of  $\bar{c}_{s,j}$  is directly proportional with the intercalation molar flux at the anode  $j_-$ , which is given in Eq.3-2, which is seen to be directly proportional to the magnitude of the charge current. As a result, a higher average charge current would result a faster increase in SOC since  $\bar{c}_{s,-}$  is related to the SOC by Eq.3-9. The magnitude of the rate of change in  $\bar{c}_{s,-}$ , a direct consequence of the penalty weights on the terms in the cost function in Eq.4-4. For example, the "Fast" strategy only penalizes  $\bar{c}_{s,-} - c_{s,max,-}$ , making it the only cost contributor in the cost function, thus the NMPC algorithm outputs the maximum charging current satisfying the constraints such that  $\bar{c}_{s,-}$  reaches  $c_{s,max}$  as quickly as possible.

As for the degradation, the main charging strategy "Health Conscious Fast + Delta u" experienced significantly lower degradation than the "Fast" strategy, have 1.6 times less total degradation average flux  $j_{sei,avg} + j_{lpl,avg}$ . Moreover, 197 charge+discharge (98 charge/discharge) cycles in "Health Conscious Fast + Delta u" are saved before full battery deterioration. On the other hand, the strategy with the least degradation "Degradation Focus" achieved 2.05 times less  $j_{sei,avg} + j_{lpl,avg}$  than the "Health Conscious Fast + Delta u", as well as saving 200 cycles before battery full deterioration. The table showing the main degradation results can be found in Table 4-2. The reason for the significant differences yet again mainly is resulting from the current dependency in  $j_{tot}$  term in both Eq.3-14 and Eq.3-16, thus the higher average current in a certain current profile would result in higher degradation. The differences in degradation for the varying current profiles is more apparent due to the exponential dependency of current with  $j_{sei}$  and  $j_{lpl}$  in Eq.3-14 and Eq.3-16, with the current being the main dominating term in the exponent, since all terms in the exponent,  $\Phi_{s,-}$ ,  $\Phi_{e,-}$  and  $j_-$  in  $j_{tot}$  are directly dependent on the current  $I$ . As a result, since there is a nonlinear proportional dependency of the current with  $j_{sei}$  and  $j_{lpl}$ , penalizing the either  $j_{sei}$  or  $j_{lpl}$  in the cost function in Eq.4-4 would result in a reduction in the overall average current as well as a change in the current in a nonlinear fashion.

To conclude the discussion regarding charging time and degradation, the "Health Conscious Fast + Delta u" achieves a suitable trade-off between charging time and degradation, since the charging time achieved is close to the "Fast" charging strategy while achieving significantly lower degradation.

A more in more depth analysis on the variables plotted is also performed. Starting with the SOC in Fig.4-4 (a), minor discrepancies in the final SOC value are noticed between each charging strategy, when in reality the final SOC for all strategies should be the same. This is mainly due to the stopping condition applied on the model, where it assesses if the next state violates the SOC constraints, the battery is put to rest for the next time instance. With the varying currents at that specific time instance as well as the high sampling period  $T_s = 60$  s, the discrepancies in the final SOC are noticed. One way to reduce this is to reduce the

sampling period  $T_s$  such that the model is run for less time at a specific current, reducing the differences in the final SOC. However, reducing the  $T_s$ , would result in an increased computational time. For example, making  $T_s = 30s$ , increased since double the number of samples are used.

As for the electrolyte concentration at the surface of the electrodes  $c_{e,surf,-}$  and  $c_{e,surf,+}$  in Fig.4-5 (a) and (b) respectively, the LGM50 battery is near the edge of the constraint for the 2C charge current, with  $c_{e,surf,-}$  approaching an equilibrium of  $85 \frac{\text{mol}}{\text{m}^3}$ . Comparing this with the recommended charge rate of 0.7C in the LGM50 specification which achieves an equilibrium  $c_{e,surf,-}$  of  $530 \frac{\text{mol}}{\text{m}^3}$ , it can be seen that such a threshold is placed such that the electrolyte concentration at the surface of the anode is kept within safe bounds. However, with the new results, while there could be a risk with 2C charging rate, it still keeps the anode surface electrolyte concentration not fully depleted and is the maximum possible charge rate allowable for the LGM50 battery.

Lastly, it was concluded that the NMPC strategy is applicable for real time control at  $T_s = 60s$ , but not  $T_s = 30s$ . The reason for this is that for  $T_s = 30s$ , the number of samples per NMPC iteration doubled, as well as the prediction/control horizon  $p = m$  doubled to match the same simulation conditions as for the  $T_s = 60s$ , significantly increasing complexity.

## 4-6 Conclusion

In this chapter, the NMPC/MPC algorithms have been briefly described, then the NMPC charging strategy formulation has been described, where the cost function and constraints in terms of the physical states were shown. The method at which the NMPC charging strategy has been implemented using the "fmincon" function in MATLAB has been explained. Moreover, results on the most relevant variables have been shown and discussed, where it was shown that the "Health Conscious Fast + Delta u" strategy achieved the best trade-off between charging time and degradation. Lastly, it was concluded that the real time control is applicable using NMPC strategy on the battery diffusion and degradation model developed for a sampling period  $T_s = 60s$ , as opposed to not be applicable for  $T_s = 30s$ .



# Conclusions and Recommendations

## 5-1 Conclusions

This study developed real-time control health conscious Fast Charging Strategy based on the steps below. An Extended Single Particle Model (ESPM) physics based Li-ion battery dynamical model was implemented, where for the solid phase dynamics, a 3-parameter approximation from the Single Particle (SP) has been used and for the electrolyte dynamics, a transfer function model obtaining the equilibrium electrolyte concentrations on the surface of the current collectors has been implemented. The model implemented was validated to be accurate for a charge range of [0,2C], by comparing it with data from the highly accurate Full Order Model (FOM), known as the Pseudo 2-Dimensional (P2D) model. Along side this model, an electro-chemical degradation model based on the study by Yang and colleagues [76] was implemented, showing the main aging mechanisms in the battery, being the Solid Electrolyte Interphase (SEI) growth, lithium plating. The degradation model was validated as in the 2 criteria previously mentioned, being that at the first charge cycle  $j_{sei}$  is a few orders of magnitude higher than  $j_{lpl}$ , and second criteria being that the capacity fade behaviour is followed as per the LGM50 battery specification sheet, shown in Fig.3-17. Using the battery diffusion and degradation model, a Nonlinear Model Predictive Control (NMPC) based charging strategy has been developed with the aim to minimize a combination of charging time, SEI growth and lithium plating growth. It was then concluded that the health conscious fast charging strategy has similar charging times to the traditional DC fast charging strategy, while increasing cycle life by 14.1 %.

The implementation of the combination of the physics-based battery model (ESPM), mainly the 3 parameter approximate solid phase diffusion model and electro-chemical degradation model, applicable in real time control applications has not been implemented before in literature, and is considered an extension to the work done by Lin and colleagues [44] , since a variation of the methods used have been incorporated in my thesis. The extensions would be the solid phase diffusion model, where instead of the 2-parameter model, a 3 parameter model has been used to improve accuracy for a wider range of currents. As for the degradation model, the extension made is the incorporation of the full electro-chemical degradation model

in the study by Yang and colleagues [76] instead of obtaining a static SEI and lithium plating map from the electro-chemical degradation model in the work by Lin and colleagues [44]. First of all, the model Lin and colleagues [44] have obtained is only applicable to the battery used in the study, and if another battery is used, the full process of obtaining the static maps would need to be implemented again, as opposed to implementation of the electro-chemical degradation model, where just some degradation parameters need to be adjusted. Moreover, the static maps obtained by Lin and colleagues [44] show that at 0C charge rate, there is no degradation, which in reality is not the case, since calendar aging is another significant form of degradation. As explained previously, the electro-chemical degradation model implemented incorporated calendar aging effects, having an equilibrium  $j_{sei}$  and  $j_{ipl}$  when the battery is at rest, showing the linear relation between capacity fade and time.

On the other hand, since there is no electro-chemical capacity fade model for this specific battery (LGM50), nor any experimental data for degradation, the degradation model parameters were chosen such that the 2 main criteria mentioned previously are followed, which are SEI molar flux should be a few orders of magnitude higher than the lithium plating molar flux, and the capacity fade of the battery follows the criteria in Fig.3-10 under experiment conditions in Fig.3-9. Such criteria would give an estimate on how the capacity fades per cycle for the LGM50 battery, but would not guarantee an exact model of it.

Lastly, the NMPC charging strategy is considered an extension to work done by Lin and colleagues [44], where they have implemented an open loop optimization based strategy has been implemented minimizing the same 3 variables as in the thesis. The optimization based strategy was solved using dynamic programming. In this thesis, a closed loop strategy was performed, which also takes into account future states when deciding an optimal charge current at a certain time step.

## 5-2 Recommendations

It was concluded that [0C 2C] charge range is sufficient for the LGM50 battery, however, for other batteries, such a C-rate range could need to be enlarged. A possible extension to the solid phase diffusion model is incorporation of an Extended Kalman Filter as in paper [9], to correct for the errors in terminal voltage between the ESPM and P2D model, however, computational time and whether real-time control is feasible after such an addition needs to be researched.

As for the degradation model, an extension to it could be the incorporation of a temperature model since the temperature is assumed to be a constant in the thesis. Such an addition would mean that the temperature effects on degradation would be more realistic, since the temperature would be changing over the charge/discharge period. The study made by Yin and colleagues [77] is one example where a temperature model is incorporated in the battery model. Again, computational complexity would need to be reassessed if such an addition would be implemented. Since the study by Okane and colleagues [53] used the LGM50 battery, showing the effect of varying different degradation parameters on the loss of lithium inventory in the LGM50 battery using an electro-chemical degradation model similar to the one used in the present work, an extension could be to combine the work done in the present work and Okane and colleague's [53] work, then finding the exact degradation parameters using experimental degradation validation.

Lastly, an extension to the NMPC charging strategy implemented in the thesis, is the incorpo-

---

ration of additional constraints, such as limit output cell voltage to be within a certain range to avoid battery over-voltage (not applicable for a range of [0 2C]), or posing constraints on the temperature, if a temperature model is included in the future.



---

# Appendix A

---

## **The Back of the Thesis**

Appendices are found in the back.



## A-1 Battery and Degradation model (LGM50 5 Ah battery)

### A-1-1 Symbol Definition and Parameter Sets

Symbol	Definition	Unit
$c_{s,j}$	Solid phase concentration in electrode j	$\frac{\text{mol}}{\text{m}^3}$
$r$	Radial distance from center of Li-ion particle	m
$R_p$	Particle Radius	m
$D_{s,j}$	Solid phase diffusivity in electrode j	$\frac{\text{m}^2}{\text{s}}$
$D_{e,j}^{\text{eff}}$	Electrolyte Effective Diffusivity in electrode j	$\frac{\text{m}^2}{\text{s}}$
$j_j$	Intercalation Molar Flux in electrode j	$\frac{\text{mol}}{\text{m}^2 \cdot \text{s}}$
$i_{0,j}$	Intercalation Exchange Current Density	$\frac{\text{A}}{\text{m}^2}$
$\eta_{\text{int},j}$	Intercalation Overpotential	V
$\Phi_{s,j}$	Solid Phase potential in electrode j	V
$\Phi_{e,j}$	Electrolyte Potential in electrode j	V
$U_{\text{int},j}$	Intercalation open circuit potential in electrode j	V
$c_{s,\text{max},j}$	Maximum Solid Phase Concentration in Electrode j	$\frac{\text{mol}}{\text{m}^3}$
$j_{\text{SEI}}$	Solid Electrolyte Interphase (SEI) Molar Flux	$\frac{\text{mol}}{\text{m}^2 \cdot \text{s}}$
$a$	Electroactive Surface Area	$\frac{\text{m}^2}{\text{m}^3}$
$F$	Faradays Constant	$\frac{\text{mol}}{\text{m}^3}$
$k_{0,\text{SEI}}$	SEI reaction rate constant	$\frac{\text{m}}{\text{s}}$
$c_{\text{EC}}^{\text{S}}$	Surface Ethyl Carbonate (EC) Bulk electrolyte Concentration	$\frac{\text{mol}}{\text{m}^3}$
$c_{\text{EC}}^{\text{I}}$	Initial Surface EC Bulk electrolyte Concentration	$\frac{\text{mol}}{\text{m}^3}$
$R$	Universal Gas Constant	K·mol
$t_+^0$	Transference Number	-
$i_{e,j}$	Electrolyte Current Density	$\frac{\text{A}}{\text{m}^2}$
$T$	Temperature	K
$D_{\text{EC}}$	EC Diffusivity	$\frac{\text{m}^2}{\text{s}}$
$R_{\text{film}}$	Film Resistance	$\Omega$
$U_{\text{SEI}}$	Equilibrium SEI Open Circuit Potential	V
$\alpha_{e,\text{SEI}}$	SEI Charge Transfer Coefficient	-
$\delta_{\text{film}}$	Film Thickness	m
$j_{\text{pl}}$	Lithium Plating Molar Flux	$\frac{\text{mol}}{\text{m}^2 \cdot \text{s}}$
$i_{0,\text{pl}}$	Lithium Plating Exchange Current Density	$\frac{\text{A}}{\text{m}^2}$
$\alpha_{e,\text{pl}}$	Lithium Plating Charge Transfer Coefficient	-
$j_{\text{tot}}$	Total molar flux	$\frac{\text{mol}}{\text{m}^2 \cdot \text{s}}$
$C_{\text{SEI}}$	SEI concentration	$\frac{\text{mol}}{\text{m}^3}$
$C_{\text{Li}}$	Lithium Plating Concentration	$\frac{\text{mol}}{\text{m}^3}$
$M_{\text{SEI}}$	SEI Molar Mass	$\frac{\text{kg}}{\text{mol}}$
$\rho_{\text{SEI}}$	SEI Molar Density	$\frac{\text{mol}}{\text{kg}}$
$M_{\text{Li}}$	Lithium Plating Molar Mass	$\frac{\text{kg}}{\text{mol}}$
$\rho_{\text{Li}}$	Lithium Plating Molar Density	$\frac{\text{mol}}{\text{kg}}$
$\omega_{\text{SEI}}$	SEI Volume Fraction	$\frac{\text{mol}}{\text{m}^3 \cdot \text{mol}}$
$\kappa_{\text{SEI}}$	SEI Ionic Conductivity	$\frac{\text{S}}{\text{m}}$
$\epsilon$	Anode porosity	-
$\text{stoic}_c$	Stoichiometry for the fully charged case	-
$\text{stoic}_d$	Stoichiometry for the fully discharged case	-
$L$	Electrode Thickness	m
$A$	Electrode Plate Area	$\text{m}^2$
$W$	Electrode Width	m
$c_{e,0,j}$	Initial Electrolyte Concentration	$\frac{\text{mol}}{\text{m}^3}$
$\sigma$	Electronic Conductivity of Solid Matrix	$\frac{\text{mol}}{\text{m}^2 \cdot \text{s}}$
$\alpha_{\text{int}}$	Intercalation Reaction Rate Constant	-
$V_{\text{cell}}$	Cell Voltage	V
$V_{\text{cell}}$	Cell Voltage	V
$\kappa_{\text{eff}}$	Ionic Conductivity of Electrolyte	$\frac{\text{S}}{\text{m}}$
$x$	Horizontal Position in Cell	m
$\Delta T_j$	Electrolyte Diffusion Dynamics Time Constant per Electrode j	m
$f_A$	Activity Coefficient in the Salt	-
$V_{\text{cell}}$	Cell Output Voltage	V
$U_{\text{ocv},\text{min}}$	Cell Terminal Voltage For The Fully Discharged Case	V
$U_{\text{ocv},\text{max}}$	Cell Terminal Voltage For The Fully Charged Case	V
$Q_{\text{cap}}$	Cell Capacity	Ah
$c_{e,\text{surf},j}$	Electrolyte Concentration near Current Collector Surface of Electrode j	$\frac{\text{mol}}{\text{m}^3}$
$c_{e,\text{surf},\text{eq},j}$	Equilibrium Electrolyte Concentration near Current Collector Surface of Electrode j	$\frac{\text{mol}}{\text{m}^3}$
$c_{s,\text{surf},j}$	Solid Phase Surface Concentration at Electrode j	$\frac{\text{mol}}{\text{m}^3}$
$c_{s,j}$	Solid Phase Concentration at Electrode j	$\frac{\text{mol}}{\text{m}^3}$
$\bar{c}_{s,j}$	Volume Averaged Solid Phase Concentration at Electrode j	$\frac{\text{mol}}{\text{m}^3}$
$q_{s,j}$	Solid Phase Concentration Flux at Electrode j	$\frac{\text{mol}}{\text{m}^2 \cdot \text{s}}$
$\bar{q}_{s,j}$	Volume Average Solid Phase Concentration Flux at Electrode j	$\frac{\text{mol}}{\text{m}^2 \cdot \text{s}}$
$R_{\text{cell}}$	Cell Internal Resistance	$\Omega$
$c_{e,j}$	Electrolyte Phase Concentration in Electrode j	$\frac{\text{mol}}{\text{m}^3}$
$V_{\text{SEI}}$	SEI Volume	$\text{m}^3$
$r_{\text{eff}}$	Reaction Rate Constant	-
$S_j$	Superficial Surface Area	$\text{m}^2$

**Table A-1:** List of Symbols for the Pseudo 2-Dimensional (P2D), Electrolyte Enhanced Single Particle Model (SPMe), Extended Single Particle Model (ESPM) and the electrochemical degradation Model.

$V_{\text{cell,min}}$	2.5
$V_{\text{cell,min}}$	4.2
$Q_{\text{cap}}$	5
$t_+$	0.2594
$F$	96485
$R$	8.3144
$T$	298
$R_{\text{cell}}$	0

**Table A-3:** List of whole cell constants LGM50.

Constant	Cathode	Separator	Anode
$D_s$	1.48e-15 [18]	-	$1.74 \times 10^{-15}$ [18]
$D_e$	-	-	-
$a$	$3.8218 \times 10^{-13}$ c	-	$3.8395 \times 10^5$ c
$k_{0,\text{SEI}}$	-	-	$2.48 \times 10^{-13}$ adj
$i_{0,\text{lpl}}$	-	-	$2 \times 10^{-3}$ adj
$c_{\text{EC}}^0$	-	-	4541.0 [61]
$D_{\text{EC}}$	-	-	$2 \times 10^{-18}$ [76]
$U_{\text{SEI}}$	-	-	0.4 [76]
$\alpha_{e,\text{SEI}}$	-	-	0.6 [61]
$i_{0,\text{lpl}}$	-	-	$10^{-5}$ adj
$\alpha_{c,\text{lpl}}$	-	-	0.7 [61]
$\rho_{\text{SEI}}$	-	-	0.6 [76]
$\rho_{\text{Li}}$	-	-	0.62 [76]
$\omega_{\text{SEI}}$	-	-	0.62 [76]
$\kappa_{\text{SEI}}$	-	-	$5 \times 10^{-6}$ adj
$\text{stoic}_c$	0.2661 [18]	-	0.9014 [18]
$\text{stoic}_d$	0.9085 [18]	-	0.0279 [18]
$L$	$75.6 \times 10^{-6}$ [18]	-	$75.6 \times 10^{-6}$ [18]
$A$	0.1027 [18]	-	0.1027 [18]
$W$	$6.5 \times 10^{-2}$ [18]	-	$6.5 \times 10^{-2}$ [18]
$c_{e,0}$	1000 [18]	1000 [18]	1000 [18]
$\Delta T$	35 <sup>adj</sup>	-	45 <sup>adj</sup>
$c_{s,\text{max}}$	51765 [18]	-	29583 [18]
$r_{\text{SEI}}$	-	-	200000 [61]
$V_{\text{SEI}}$	-	-	-
$f_A$	N/A	N/A	N/A

**Table A-2:** List of the LGM50 cell electrode parameters used for the P2D,SPMe,ESPM and the electro-chemical degradation Model. c: Calculated, <sup>adj</sup>: Adjusted, N/A : Not available.

---

## Appendix B

---

# Nonlinear Model Predictive Control (NMPC)

## B-1 Parameters per Strategy

### B-1-1 State $x$ and Input $u$ Bounds

The upper and lower bounds for the state and input vectors in Eq.4-2 are as follows,

$$\mathbf{x}_{lb} = \begin{bmatrix} -\infty \\ 0 \\ 0 \\ 0 \\ 0 \\ 0 \\ 0 \\ 0 \\ -\infty \\ -\infty \\ -\infty \\ -\infty \\ \mathbf{u}_{lb} = -10 \end{bmatrix} \quad \mathbf{x}_{ub} = \begin{bmatrix} 0 \\ \infty \\ c_{s,max,+} \\ c_{s,max,-} \\ \infty \\ 0 \\ 0 \\ 0 \\ 0 \\ -\infty \\ -\infty \\ -\infty \\ \mathbf{u}_{ub} = 0 \end{bmatrix} \quad (\text{B-1})$$

### B-1-2 Weighting Matrices $Q$ and $R$

#### "Fast" Strategy

$$Q = \begin{pmatrix} 0 & 0 & 0 & 0 & 0 & 0 & 0 & 0 & 0 & 0 \\ 0 & 0 & 0 & 0 & 0 & 0 & 0 & 0 & 0 & 0 \\ 0 & 0 & 0 & 0 & 0 & 0 & 0 & 0 & 0 & 0 \\ 0 & 0 & 0 & 1.14 \times 10^{-9} & 0 & 0 & 0 & 0 & 0 & 0 \\ 0 & 0 & 0 & 0 & 0 & 0 & 0 & 0 & 0 & 0 \\ 0 & 0 & 0 & 0 & 0 & 0 & 0 & 0 & 0 & 0 \\ 0 & 0 & 0 & 0 & 0 & 0 & 0 & 0 & 0 & 0 \\ 0 & 0 & 0 & 0 & 0 & 0 & 0 & 0 & 0 & 0 \\ 0 & 0 & 0 & 0 & 0 & 0 & 0 & 0 & 0 & 0 \\ 0 & 0 & 0 & 0 & 0 & 0 & 0 & 0 & 0 & 0 \\ 0 & 0 & 0 & 0 & 0 & 0 & 0 & 0 & 0 & 0 \end{pmatrix} \quad (B-2)$$

$$R = 0$$

#### "SEI focus" Strategy

$$Q = \begin{pmatrix} 0 & 0 & 0 & 0 & 0 & 0 & 0 & 0 & 0 & 0 \\ 0 & 0 & 0 & 0 & 0 & 0 & 0 & 0 & 0 & 0 \\ 0 & 0 & 0 & 0 & 0 & 0 & 0 & 0 & 0 & 0 \\ 0 & 0 & 0 & 1.14 \times 10^{-11} & 0 & 0 & 0 & 0 & 0 & 0 \\ 0 & 0 & 0 & 0 & 0 & 0 & 0 & 0 & 0 & 0 \\ 0 & 0 & 0 & 0 & 0 & 0 & 0 & 0 & 0 & 0 \\ 0 & 0 & 0 & 0 & 0 & 0 & 0 & 0 & 0 & 0 \\ 0 & 0 & 0 & 0 & 0 & 0 & 0 & 0 & 0 & 0 \\ 0 & 0 & 0 & 0 & 0 & 0 & 0 & 0 & 0 & 0 \\ 0 & 0 & 0 & 0 & 0 & 0 & 0 & 0 & 17361110 & 0 \\ 0 & 0 & 0 & 0 & 0 & 0 & 0 & 0 & 0 & 0 \end{pmatrix} \quad (B-3)$$

$$R = 0$$

#### "LPL focus" Strategy

$$Q = \begin{pmatrix} 0 & 0 & 0 & 0 & 0 & 0 & 0 & 0 & 0 & 0 \\ 0 & 0 & 0 & 0 & 0 & 0 & 0 & 0 & 0 & 0 \\ 0 & 0 & 0 & 0 & 0 & 0 & 0 & 0 & 0 & 0 \\ 0 & 0 & 0 & 1.14 \times 10^{-11} & 0 & 0 & 0 & 0 & 0 & 0 \\ 0 & 0 & 0 & 0 & 0 & 0 & 0 & 0 & 0 & 0 \\ 0 & 0 & 0 & 0 & 0 & 0 & 0 & 0 & 0 & 0 \\ 0 & 0 & 0 & 0 & 0 & 0 & 0 & 0 & 0 & 0 \\ 0 & 0 & 0 & 0 & 0 & 0 & 0 & 0 & 0 & 0 \\ 0 & 0 & 0 & 0 & 0 & 0 & 0 & 0 & 0 & 0 \\ 0 & 0 & 0 & 0 & 0 & 0 & 0 & 0 & 0 & 0 \\ 0 & 0 & 0 & 0 & 0 & 0 & 0 & 0 & 0 & 8.41 \times 10^{14} \end{pmatrix} \quad (B-4)$$

$$R = 0$$

**"Degradation focus" Strategy**

$$Q = \begin{pmatrix} 0 & 0 & 0 & 0 & 0 & 0 & 0 & 0 & 0 & 0 \\ 0 & 0 & 0 & 0 & 0 & 0 & 0 & 0 & 0 & 0 \\ 0 & 0 & 0 & 0 & 0 & 0 & 0 & 0 & 0 & 0 \\ 0 & 0 & 0 & 1.14 \times 10^{-11} & 0 & 0 & 0 & 0 & 0 & 0 \\ 0 & 0 & 0 & 0 & 0 & 0 & 0 & 0 & 0 & 0 \\ 0 & 0 & 0 & 0 & 0 & 0 & 0 & 0 & 0 & 0 \\ 0 & 0 & 0 & 0 & 0 & 0 & 0 & 0 & 0 & 0 \\ 0 & 0 & 0 & 0 & 0 & 0 & 0 & 0 & 0 & 0 \\ 0 & 0 & 0 & 0 & 0 & 0 & 0 & 0 & 0 & 0 \\ 0 & 0 & 0 & 0 & 0 & 0 & 0 & 1736111 & 0 & 0 \\ 0 & 0 & 0 & 0 & 0 & 0 & 0 & 0 & 8.41 \times 10^{15} & 0 \end{pmatrix} \quad (\text{B-5})$$

$$R = 0$$

**"Health Conscious Fast + Delta u" Strategy**

$$Q = \begin{pmatrix} 0 & 0 & 0 & 0 & 0 & 0 & 0 & 0 & 0 & 0 \\ 0 & 0 & 0 & 0 & 0 & 0 & 0 & 0 & 0 & 0 \\ 0 & 0 & 0 & 0 & 0 & 0 & 0 & 0 & 0 & 0 \\ 0 & 0 & 0 & 1.14 \times 10^{-9} & 0 & 0 & 0 & 0 & 0 & 0 \\ 0 & 0 & 0 & 0 & 0 & 0 & 0 & 0 & 0 & 0 \\ 0 & 0 & 0 & 0 & 0 & 0 & 0 & 0 & 0 & 0 \\ 0 & 0 & 0 & 0 & 0 & 0 & 0 & 0 & 0 & 0 \\ 0 & 0 & 0 & 0 & 0 & 0 & 0 & 0 & 0 & 0 \\ 0 & 0 & 0 & 0 & 0 & 0 & 0 & 0 & 0 & 0 \\ 0 & 0 & 0 & 0 & 0 & 0 & 0 & 1736111 & 0 & 0 \\ 0 & 0 & 0 & 0 & 0 & 0 & 0 & 0 & 8.41 \times 10^{15} & 0 \end{pmatrix} \quad (\text{B-6})$$

$$R = 0.01$$



---

# Bibliography

- [1] EV-Volumes - The Electric Vehicle World Sales Database.
- [2] How Does a Lithium-ion Battery Work?, <https://www.energy.gov/eere/articles/how-does-lithium-ion-battery-work>, 2017.
- [3] Climate Action: Transport emissions, 2021.
- [4] Mohamed Abdel Monem, Khiem Trad, Noshin Omar, Omar Hegazy, Bart Mantels, Grietus Mulder, Peter Van den Bossche, and Joeri Van Mierlo. Lithium-ion batteries: Evaluation study of different charging methodologies based on aging process. *Applied Energy*, 152:143–155, 8 2015.
- [5] Aiman M Albatayneh, Mohammed N Assaf, Aiman Albatayneh, Mohammad N Assaf, Dariusz Alterman, and Mustafa Jaradat. Comparison of the Overall Energy Efficiency for Internal Combustion Engine Vehicles and Electric Vehicles Adsorption retrogression system View project Comparison of the Overall Energy Efficiency for Internal Combustion Engine Vehicles and Electric Vehicles. 24(1):669–680, 2020.
- [6] D. Anseán, M. González, J. C. Viera, V. M. García, C. Blanco, and M. Valledor. Fast charging technique for high power lithium iron phosphate batteries: A cycle life analysis. *Journal of Power Sources*, 239:9–15, 2013.
- [7] Pankaj Arora, Marc Doyle, and Ralph E White. Mathematical Modeling of the Lithium Deposition Overcharge Reaction in Lithium-Ion Batteries Using Carbon-Based Negative Electrodes. Technical Report 10, 1999.
- [8] Harikesh Arunachalam and Simona Onori. Full Homogenized Macroscale Model and Pseudo-2-Dimensional Model for Lithium-Ion Battery Dynamics: Comparative Analysis, Experimental Verification and Sensitivity Analysis. *Journal of The Electrochemical Society*, 166(8):A1380–A1392, 2019.
- [9] Yalan Bi and Song Yul Choe. An adaptive sigma-point Kalman filter with state equality constraints for online state-of-charge estimation of a Li(NiMnCo)O<sub>2</sub>/Carbon battery using a reduced-order electrochemical model. *Applied Energy*, 258, 1 2020.

- [10] Christoph R. Birkl, Matthew R. Roberts, Euan McTurk, Peter G. Bruce, and David A. Howey. Degradation diagnostics for lithium ion cells. *Journal of Power Sources*, 341:373–386, 2 2017.
- [11] Bernhard Bitzer and Andreas Gruhle. A new method for detecting lithium plating by measuring the cell thickness. *Journal of Power Sources*, 262:297–302, 9 2014.
- [12] Gerardine G Botte, Venkat R Subramanian, and Ralph E White. Mathematical modeling of secondary lithium batteries. Technical report, 2000.
- [13] M. Broussely, Ph Biensan, F. Bonhomme, Ph Blanchard, S. Herreyre, K. Nechev, and R. J. Staniewicz. Main aging mechanisms in Li ion batteries. In *Journal of Power Sources*, volume 146, pages 90–96, 8 2005.
- [14] Thomas S. Bryden, George Hilton, Andrew Cruden, and Tim Holton. Electric vehicle fast charging station usage and power requirements. *Energy*, 152:322–332, 6 2018.
- [15] Long Cai and Ralph E. White. Mathematical modeling of a lithium ion battery with thermal effects in COMSOL Inc. Multiphysics (MP) software. *Journal of Power Sources*, 196(14):5985–5989, 7 2011.
- [16] E. F. Camacho and C. Bordons. *Model Predictive control*. Springer London, London, 2007.
- [17] Rajeswari Chandrasekaran. Quantification of bottlenecks to fast charging of lithium-ion-insertion cells for electric vehicles. *Journal of Power Sources*, 271:622–632, 12 2014.
- [18] Chang-Hui Chen, Ferran Brosa Planella, Kieran O’Regan, Dominika Gastol, W. Dhammika Widanage, and Emma Kendrick. Development of Experimental Techniques for Parameterization of Multi-scale Lithium-ion Battery Models. *Journal of The Electrochemical Society*, 167(8):080534, 1 2020.
- [19] Sukyoung Choi, Gyujin Jung, Jong Eun Kim, Tae Young Kim, and Kwang S. Suh. Lithium intercalated graphite with preformed passivation layer as superior anode for Lithium ion batteries. *Applied Surface Science*, 455:367–372, 10 2018.
- [20] Edmund J.F. Dickinson and Andrew J. Wain. The Butler-Volmer equation in electrochemical theory: Origins, value, and practical application. *Journal of Electroanalytical Chemistry*, 872, 9 2020.
- [21] Marc Doyle and John Newman. The use of mathematical modeling in the design of lithium or polymer battery systems. *Electrochimica Acta*, 40(13):2191–2196, 4 1995.
- [22] João P.D. Faria, Ricardo L. Velho, Maria R.A. Calado, José A.N. Pombo, João B.L. Fermeiro, and Sílvio J.P.S. Mariano. A New Charging Algorithm for Li-Ion Battery Packs Based on Artificial Neural Networks. *Batteries*, 8(2), 2 2022.
- [23] I. J. Fernández, C. F. Calvillo, A. Sánchez-Miralles, and J. Boal. Capacity fade and aging models for electric batteries and optimal charging strategy for electric vehicles. *Energy*, 60:35–43, 10 2013.

- 
- [24] Parthasarathy M Gomadam, John W Weidner, Roger A Dougal, and Ralph E White. Mathematical modeling of lithium-ion and nickel battery systems. *Journal of Power Sources*, 110:267–284, 2002.
- [25] Lars Grüne and Jürgen Pannek. *Nonlinear Model Predictive Control*. Springer London, London, 2011.
- [26] W B Gu and C Y Wang. Thermal-Electrochemical Modeling of Battery Systems. Technical Report 8, 2000.
- [27] Pengjian Guan, Lin Liu, and Xianke Lin. Simulation and Experiment on Solid Electrolyte Interphase (SEI) Morphology Evolution and Lithium-Ion Diffusion. *Journal of The Electrochemical Society*, 162(9):A1798–A1808, 2015.
- [28] Meng Guo, Godfrey Sikha, and Ralph E. White. Single-Particle Model for a Lithium-Ion Cell: Thermal Behavior. *Journal of The Electrochemical Society*, 158(2):A122, 2011.
- [29] Sangwoo Han, Yifan Tang, and Saeed Khaleghi Rahimian. A numerically efficient method of solving the full-order pseudo-2-dimensional (P2D) Li-ion cell model. *Journal of Power Sources*, 490, 4 2021.
- [30] M. A. Hannan, F. A. Azidin, and A. Mohamed. Hybrid electric vehicles and their challenges: A review, 2014.
- [31] C. C. Hua and M. Y. Lin. A study of charging control of lead-acid battery for electric vehicles. In *IEEE International Symposium on Industrial Electronics*, volume 1, pages 135–140, 2000.
- [32] Shahid Hussain, Mohamed A. Ahmed, Ki Beom Lee, and Young Chon Kim. Fuzzy logic weight based charging scheme for optimal distribution of charging power among electric vehicles in a parking lot. *Energies*, 13(12), 6 2020.
- [33] Tomohiko Ikeya, Nobuyuki Sawada, Jun-Ich Murakami, Kazsuyuki Kobayashi, Masanori Hattori, Nobuo Murotani, Satoru Ujiie, Katuya Kajiyama, Hideki Nasu, Hayato Narisoko, Yuichi Tomaki, Kazuyuki Adachi, Yuichi Mita, and Kaoru Ishihara. Multi-step constant-current charging method for an electric vehicle nickel/metal hydride battery with high-energy efficiency and long cycle life. Technical report, 2001.
- [34] Ali Jokar, Barzin Rajabloo, Martin Désilets, and Marcel Lacroix. Review of simplified Pseudo-two-Dimensional models of lithium-ion batteries, 9 2016.
- [35] Paulo Kemper, Shengbo Eben Li, and Dongsuk Kum. Simplification of pseudo two dimensional battery model using dynamic profile of lithium concentration. *Journal of Power Sources*, 286:510–525, 7 2015.
- [36] Saeed Khaleghi Rahimian, Sean Rayman, and Ralph E. White. Extension of physics-based single particle model for higher charge-discharge rates. *Journal of Power Sources*, 224:180–194, 2 2013.
- [37] Suryanarayana Kolluri, Sai Varun Aduru, Manan Pathak, Richard D. Braatz, and Venkat R. Subramanian. Real-time Nonlinear Model Predictive Control (NMPC) Strategies using Physics-Based Models for Advanced Lithium-ion Battery Management System (BMS). *Journal of The Electrochemical Society*, 167(6):063505, 1 2020.

- [38] Changlong Li, Naxin Cui, Chunyu Wang, and Chenghui Zhang. Reduced-order electrochemical model for lithium-ion battery with domain decomposition and polynomial approximation methods. *Energy*, 221, 4 2021.
- [39] J. Li, K. Adewuyi, N. Lotfi, R. G. Landers, and J. Park. A single particle model with chemical/mechanical degradation physics for lithium ion battery State of Health (SOH) estimation. *Applied Energy*, 212:1178–1190, 2 2018.
- [40] J. Li, N. Lotfi, R. G. Landers, and J. Park. A Single Particle Model for Lithium-Ion Batteries with Electrolyte and Stress-Enhanced Diffusion Physics. *Journal of The Electrochemical Society*, 164(4):A874–A883, 2017.
- [41] Xueyan Li, Meng Xiao, and Song Yul Choe. Reduced order model (ROM) of a pouch type lithium polymer battery based on electrochemical thermal principles for real time applications. *Electrochimica Acta*, 97:66–78, 5 2013.
- [42] Yunjian Li, Kuining Li, Yi Xie, Jiangyan Liu, Chunyun Fu, and Bin Liu. Optimized charging of lithium-ion battery for electric vehicles: Adaptive multistage constant current–constant voltage charging strategy. *Renewable Energy*, 146:2688–2699, 2 2020.
- [43] Bor Yann Liaw, E. Peter Roth, Rudolph G. Jungst, Ganesan Nagasubramanian, Herbert L. Case, and Daniel H. Doughty. Correlation of Arrhenius behaviors in power and capacity fades with cell impedance and heat generation in cylindrical lithium-ion cells. In *Journal of Power Sources*, volume 119-121, pages 874–886, 6 2003.
- [44] Xianke Lin, Xiaoguang Hao, Zhenyu Liu, and Weiqiang Jia. Health conscious fast charging of Li-ion batteries via a single particle model with aging mechanisms. *Journal of Power Sources*, 400:305–316, 10 2018.
- [45] Xianke Lin, Jonghyun Park, Lin Liu, Yoonkoo Lee, A. M. Sastry, and Wei Lu. A Comprehensive Capacity Fade Model and Analysis for Li-Ion Batteries. *Journal of The Electrochemical Society*, 160(10):A1701–A1710, 2013.
- [46] Xianke Lin, Jonghyun Park, Lin Liu, Yoonkoo Lee, A. M. Sastry, and Wei Lu. A Comprehensive Capacity Fade Model and Analysis for Li-Ion Batteries. *Journal of The Electrochemical Society*, 160(10):A1701–A1710, 2013.
- [47] Xianke Lin, Siyang Wang, and Youngki Kim. A framework for charging strategy optimization using a physics-based battery model. *Journal of Applied Electrochemistry*, 49(8):779–793, 8 2019.
- [48] Lin Liu, Jonghyun Park, Xianke Lin, Ann Marie Sastry, and Wei Lu. A thermal-electrochemical model that gives spatial-dependent growth of solid electrolyte interphase in a Li-ion battery. *Journal of Power Sources*, 268:482–490, 12 2014.
- [49] Zhe Liu, Fahim Forouzanfar, and Yu Zhao. Comparison of SQP and AL algorithms for deterministic constrained production optimization of hydrocarbon reservoirs. *Journal of Petroleum Science and Engineering*, 171:542–557, 12 2018.
- [50] Weilin Luo, Chao Lyu, Lixin Wang, and Liqiang Zhang. A new extension of physics-based single particle model for higher charge-discharge rates. *Journal of Power Sources*, 241:295–310, 2013.

- 
- [51] Weilin Luo, Chao Lyu, Lixin Wang, and Liqiang Zhang. A new extension of physics-based single particle model for higher charge-discharge rates. *Journal of Power Sources*, 241:295–310, 2013.
- [52] Gang Ning and Branko N. Popov. Cycle Life Modeling of Lithium-Ion Batteries. *Journal of The Electrochemical Society*, 151(10):A1584, 2004.
- [53] Simon E.J. O’Kane, Weilong Ai, Ganesh Madabattula, Diego Alonso-Alvarez, Robert Timms, Valentin Sulzer, Jacqueline Sophie Edge, Billy Wu, Gregory J. Offer, and Monica Marinescu. Lithium-ion battery degradation: how to model it. *Physical Chemistry Chemical Physics*, 24(13):7909–7922, 3 2022.
- [54] Aloke Paul, Tomi Laurila, Vesa Vuorinen, · Sergiy, and V Divinski Thermodynamics. *Diffusion and the Kirkendall Effect in Solids*. Springer, 2014.
- [55] Grigorios A. Pavliotis. The Fokker–Planck Equation. pages 87–137. 2014.
- [56] Delfim Pedrosa, Vitor Monteiro, Henrique Gonçalves, Júlio S. Martins, and João L. Afonso. A case study on the conversion of an internal combustion engine vehicle into an electric vehicle. In *2014 IEEE Vehicle Power and Propulsion Conference, VPPC 2014*. Institute of Electrical and Electronics Engineers Inc., 1 2015.
- [57] Oleg A. Petrii, Renat R. Nazmutdinov, Michael D. Bronshtein, and Galina A. Tsirlina. Life of the Tafel equation: Current understanding and prospects for the second century. *Electrochimica Acta*, 52(11):3493–3504, 3 2007.
- [58] Harry J. Ploehn, Premanand Ramadass, and Ralph E. White. Solvent Diffusion Model for Aging of Lithium-Ion Battery Cells. *Journal of The Electrochemical Society*, 151(3):A456, 2004.
- [59] P Ramadass, Bala Haran, Ralph White, and Branko N Popov. Capacity fade of Sony 18650 cells cycled at elevated temperatures Part I. Cycling performance. Technical report, 2002.
- [60] Elisha Rejovitzky, Claudio V. Di Leo, and Lallit Anand. A theory and a simulation capability for the growth of a solid electrolyte interphase layer at an anode particle in a Li-ion battery. *Journal of the Mechanics and Physics of Solids*, 78:210–230, 2015.
- [61] M. Safari, M. Morcrette, A. Teysso, and C. Delacourt. Multimodal Physics-Based Aging Model for Life Prediction of Li-Ion Batteries. *Journal of The Electrochemical Society*, 156(3):A145, 2009.
- [62] M. Safari, M. Morcrette, A. Teysso, and C. Delacourt. Life-Prediction Methods for Lithium-Ion Batteries Derived from a Fatigue Approach. *Journal of The Electrochemical Society*, 157(6):A713, 2010.
- [63] Julio A. Sanguesa, Vicente Torres-Sanz, Piedad Garrido, Francisco J. Martinez, and Johann M. Marquez-Barja. A review on electric vehicles: Technologies and challenges, 3 2021.
- [64] Weixang Shen, Thanh Tu Vo, and Ajay Kapoor. *Charging Algorithms of Lithium-Ion Batteries: an Overview*. 2011.

- [65] Kandler A. Smith, Christopher D. Rahn, and Chao Yang Wang. Control oriented 1D electrochemical model of lithium ion battery. *Energy Conversion and Management*, 48(9):2565–2578, 9 2007.
- [66] Minseok Song and Song Yul Choe. Fast and safe charging method suppressing side reaction and lithium deposition reaction in lithium ion battery. *Journal of Power Sources*, 436, 10 2019.
- [67] Franz B. Spingler, Wilhelm Wittmann, Johannes Sturm, Bernhard Rieger, and Andreas Jossen. Optimum fast charging of lithium-ion pouch cells based on local volume expansion criteria. *Journal of Power Sources*, 393:152–160, 7 2018.
- [68] Venkat Srinivasan and C. Y. Wang. Analysis of Electrochemical and Thermal Behavior of Li-Ion Cells. *Journal of The Electrochemical Society*, 150(1):A98–A106, 1 2003.
- [69] Venkat R. Subramanian, Vinten D. Diwakar, and Deepak Tapriyal. Efficient Macro-Micro Scale Coupled Modeling of Batteries. *Journal of The Electrochemical Society*, 152(10):A2002, 2005.
- [70] Xiaoli Sun, Zhengguo Li, Xiaolin Wang, and Chengjiang Li. Technology development of electric vehicles: A review. *Energies*, 13(1), 12 2019.
- [71] A. A. Tahmasbi, T. Kadyk, and M. H. Eikerling. Statistical Physics-Based Model of Solid Electrolyte Interphase Growth in Lithium Ion Batteries. *Journal of The Electrochemical Society*, 164(6):A1307–A1313, 2017.
- [72] And Ts, Rosamar a Fong, Ulrich Yon Sacken, and J R Dahn. s163163 SCIs163 Studies of Lithium Intercalation into Carbons Using Nonaqueous Electrochemical Cells. Technical report, 1990.
- [73] Walter A. van Schalkwijk and Bruno Scrosati. *Advances in Lithium-Ion Batteries*. 2002.
- [74] Thomas Waldmann, Michael Kasper, and Margret Wohlfahrt-Mehrens. Optimization of Charging Strategy by Prevention of Lithium Deposition on Anodes in high-energy Lithium-ion Batteries - Electrochemical Experiments. *Electrochimica Acta*, 178:525–532, 10 2015.
- [75] Nikolaos Wassiliadis, Jakob Schneider, Alexander Frank, Leo Wildfeuer, Xue Lin, Andreas Jossen, and Markus Lienkamp. Review of fast charging strategies for lithium-ion battery systems and their applicability for battery electric vehicles, 12 2021.
- [76] Xiao Guang Yang, Yongjun Leng, Guangsheng Zhang, Shanhai Ge, and Chao Yang Wang. Modeling of lithium plating induced aging of lithium-ion batteries: Transition from linear to nonlinear aging. *Journal of Power Sources*, 360:28–40, 2017.
- [77] Yilin Yin and Song Yul Choe. Actively temperature controlled health-aware fast charging method for lithium-ion battery using nonlinear model predictive control. *Applied Energy*, 271, 8 2020.
- [78] Yilin Yin, Yang Hu, Song Yul Choe, Hana Cho, and Won Tae Joe. New fast charging method of lithium-ion batteries based on a reduced order electrochemical model considering side reaction. *Journal of Power Sources*, 423:367–379, 5 2019.

- 
- [79] D Zhang, B S Haran, A Durairajan, R E White, Y Podrazhansky, and B N Popov. Studies on capacity fade of lithium-ion batteries. Technical report, 2000.
- [80] S. S. Zhang, K. Xu, and T. R. Jow. Study of the charging process of a LiCoO<sub>2</sub>-based Li-ion battery. *Journal of Power Sources*, 160(2 SPEC. ISS.):1349–1354, 10 2006.
- [81] Martin Zier, Frieder Scheiba, Steffen Oswald, Jürgen Thomas, Dietrich Goers, Torsten Scherer, Markus Klose, Helmut Ehrenberg, and Jürgen Eckert. Lithium dendrite and solid electrolyte interphase investigation using OsO<sub>4</sub>. *Journal of Power Sources*, 266:198–207, 11 2014.
- [82] Changfu Zou, Xiaosong Hu, Zhongbao Wei, and Xiaolin Tang. Electrothermal dynamics-conscious lithium-ion battery cell-level charging management via state-monitored predictive control. *Energy*, 141:250–259, 2017.
- [83] Changfu Zou, Xiaosong Hu, Zhongbao Wei, Torsten Wik, and Bo Egardt. Electrochemical Estimation and Control for Lithium-Ion Battery Health-Aware Fast Charging. *IEEE Transactions on Industrial Electronics*, 65(8):6635–6645, 8 2018.
- [84] Ghassan Zubi, Rodolfo Dufo-López, Monica Carvalho, and Guzay Pasaoglu. The lithium-ion battery: State of the art and future perspectives, 6 2018.



---

# Glossary

## List of Acronyms

<b>P2D</b>	Pseudo 2-Dimensional
<b>EV</b>	Electric Vehicle
<b>EVs</b>	Electric Vehicles
<b>ICEV</b>	Internal Combustion Energy vehicle
<b>ICEVs</b>	Internal Combustion Energy Vehicles
<b>NEVs</b>	New Energy Vehicles
<b>WTW</b>	Well To Wheel
<b>SEI</b>	Solid Electrolyte Interphase
<b>RC</b>	Resistor-Capacitor
<b>MCCCV</b>	Multistage Constant Current Constant Voltage
<b>NiMH</b>	Nickel Metal Hydride
<b>NiCd</b>	Nickel Cadmium
<b>OCV</b>	Open Circuit Voltage
<b>FOM</b>	Full Order Model
<b>FOMs</b>	Full Order Models
<b>SPMe</b>	Electrolyte Enhanced Single Particle Model
<b>ESPM</b>	Extended Single Particle Model
<b>CCCV</b>	Constant-Current Constant-Voltage
<b>AMCCCV</b>	Adaptive Multistage Constant-Current Constant-Voltage (CCCV)
<b>NMPC</b>	Nonlinear Model Predictive Control
<b>FUDS</b>	Federal Urban Driving Schedule
<b>MPC</b>	Model Predictive Control
<b>SOC</b>	State Of Charge

---

<b>SOCs</b>	States Of Charge
<b>EC</b>	Ethyl Carbonate
<b>DP</b>	Dynamic Programming
<b>BMS</b>	Battery Management System
<b>SPKF</b>	Sigma-Point Kalman Filter
<b>ROM</b>	Reduced Order Model
<b>SQP</b>	Sequential Quadratic Programming
<b>ODE</b>	Ordinary Differential Equation
<b>PDE</b>	Partial Differential Equation
<b>ODEs</b>	Ordinary Differential Equations
<b>PDEs</b>	Partial Differential Equations
<b>SP</b>	Single Particle
<b>RMSE</b>	Root Mean Square Error
<b>VAF</b>	Variance Accounted For
<b>DFN</b>	Doyle-Fuller Newman
<b>FHM</b>	Full Homogenized Macroscale

## List of Symbols

$A(s)$	Answer function
--------	-----------------

---

# Index

math, 12

test, 12